

QCD at finite density with Dyson-Schwinger equations

Vom Fachbereich Physik
der Technischen Universität Darmstadt

zur Erlangung des Grades
eines Doktors der Naturwissenschaften
(Dr. rer. nat.)

genehmigte Dissertation von
M.Sc. Daniel Roland Müller
aus Miltenberg

Darmstadt 2013
D17

Referent: Prof. Dr. Jochen Wambach
Korreferent: Priv. Doz. Dr. Michael Buballa

Tag der Einreichung 24.04.2013
Tag der Prüfung: 27.05.2013

Zusammenfassung

In dieser Arbeit untersuchen wir QCD bei endlicher Dichte mit Dyson-Schwinger Gleichungen. Im ersten Teil betrachten wir dabei farbsupraleitende Phasen, welche bei hohen Dichten durch Bildung von Quark-Quark Paaren auftreten. Wir beschreiben dabei die 2SC und CFL Phase mit massiven Strangequarks. Zunächst berechnen wir das Phasendiagramm in einer Hard-Thermal-Loop / Hard-Dense-Loop Näherung, welche nackte masselose Quarks an die Gluonen rückkoppelt. Die Vertex Parameter fitteten wir an eine chirale kritische Temperatur von $T_c = 150$ MeV. Diese Näherung ergibt recht niedrige kritische Temperaturen für die farbsupraleitenden Phasen um $20 - 30$ MeV und eine zu hohe Pionerfallskonstante. Zur Verbesserung der Trunkierung koppeln wir anschließend den vollen farbsupraleitenden Quarkpropagator an die Gluonen. Neben den realistischeren Vakuumobservablen steigen die kritischen Temperaturen auch auf $40 - 60$ MeV an. Wir finden eine dominante CFL Phase bei hohen Dichten, bei mittlerem chemischen Potential ist der Grundzustand eine 2SC Phase, welche auch stets in einem schmalen Band zwischen CFL und normalleitender Phase auftritt. Wir berechnen auch Debye- und Meissnermassen der Gluonen, welche die Vorhersagen von Rechnungen bei schwacher Kopplung reproduzieren können.

Im zweiten Teil der Arbeit betrachten wir chirale Kondensate mit räumlichen Modulationen. Wir untersuchen dazu eindimensionale Modulationen in Form einer ebenen Welle, welche zwischen einem skalaren und einem pseudoskalaren Kondensat rotiert, im Dyson-Schwinger Formalismus und lösen das System. Wir erhalten eine inhomogene Phase, die den ursprünglich chiralen Phasenübergang erster Ordnung überdeckt, was mit Ergebnissen aus vergleichbaren Modellrechnungen übereinstimmt.

Abstract

In this work we investigate QCD at finite density with Dyson-Schwinger equations. In the first part we consider color-superconducting phases, which occur at high densities through the formation of quark-quark pairs. We describe 2SC and CFL phases with massive strange quarks. We calculate the phase diagram in a hard-thermal-loop / hard-dense-loop approximation which describes the back-coupling of massless quarks to the gluons. We fixed the vertex parameters to a chiral critical temperature of $T_c = 150$ MeV. This approximation results in low critical temperatures for the color-superconducting phases around $20 - 30$ MeV and a too large pion decay constant. To improve the truncation we couple the full color-superconducting quark propagator back to the gluons. In addition to more realistic vacuum observables also the critical temperatures increase to $40 - 60$ MeV. We find a dominant CFL phase at high densities, while at intermediate chemical potential, the ground state is a 2SC phase which also extends to a small band between CFL and normal conducting phase. We also calculate Debye and Meissner masses of the gluons, which can reproduce the results of weak-coupling calculations.

In the second part of this work we consider chiral condensates with the possibility of spatial modulations. We investigate 1-dimensional modulations with plane-wave shape, which oscillate between a scalar and a pseudoscalar condensate, in the Dyson-Schwinger formalism. We find an inhomogeneous phase that covers the original first-order chiral phase transition, which is in agreement with similar model calculations.

Contents

1. Introduction	1
2. QCD and Dyson-Schwinger equations	7
2.1. QCD basics	7
2.1.1. Gauge fixing	8
2.1.2. Renormalization	9
2.1.3. QCD symmetries	10
2.2. Dyson-Schwinger equations	12
2.2.1. Quark Dyson-Schwinger equation	12
2.2.2. Gluon Dyson-Schwinger equation	15
2.2.3. Dyson-Schwinger equation of the quark-gluon vertex	16
2.3. Effective action, quark condensate and pion properties	16
2.4. Color superconductivity	19
2.4.1. Structure of color-superconducting phases	21
2.4.2. Color-superconducting condensates	25
2.4.3. Symmetry relations of the propagator	26
3. Color-superconducting phases in a HTL-HDL truncation	29
3.1. Truncation of the quark-gluon vertex	29
3.2. Truncation of the gluon DSE	30
3.3. HTL-HDL approximation	32
3.4. Strange-quark mass	33
3.5. Results	35
4. Self-consistent calculation of the gluon propagator	41
4.1. Gluon DSE with self-consistent quarks	41
4.2. Renormalization of the gluon DSE	42
4.3. Regularization of the quark loop	44
4.3.1. Regularization for normal phases	44
4.3.2. Regularization for full NG propagators	48
4.4. Evaluating the quark loop	49

4.5. Results	51
4.6. Debye and Meissner masses	55
4.7. Silver-Blaze property	61
5. Inhomogeneous phases	65
5.1. Quark propagator for inhomogeneous phases	65
5.2. Gap equations	69
5.3. Results	73
6. Conclusion and Outlook	79
A. Definitions	82
A.1. Conventions	82
A.2. Dirac matrices	82
A.3. Fourier transformation	83
A.4. Integral conventions	83
B. Correlation functions	85
C. Derivation of Dyson-Schwinger equations	87
C.1. Quark DSE	87
C.2. Gluon DSE	88
D. Details on the gluon polarization	90
E. Numerical calculation	93
F. A remark on the iterative procedure	96

1. Introduction

Nature can be described with four fundamental forces: the electromagnetic, the weak and the strong interaction and the gravitational force. Except for gravity, whose features at high energies are still unknown, the forces are described by relativistic quantum field theories in the standard model. It includes the fermionic quarks and leptons, the gauge bosons photons, gluons, W^\pm and Z and the Higgs boson. While the fermions and gauge bosons have all been discovered until 2000, a possible discovery of the Higgs particle was just recently announced in 2012 at CERN [1, 2]. The quantum field theories are gauge theories that describe fermions and gauge bosons with an interaction between these particles defined by the principle of local gauge invariance. This invariance also requires the gauge bosons to be massless, however, they can acquire a dynamical mass due to spontaneous symmetry breaking of the local gauge symmetry with the Higgs mechanism.

While weak and electromagnetic interactions are understood well theoretically and can be verified in precision experiments, the strong force still has many open questions. It is described by the $SU(3)$ gauge theory quantum chromodynamics (QCD) with quarks and gluons as elementary degrees of freedom. The charges of QCD are the 3 colors red, green, blue and the corresponding anticharges. It is a non-abelian gauge theory, therefore the gluons can interact with each other directly. At high energies, the QCD coupling decreases logarithmically and the interaction becomes weak. This feature is called asymptotic freedom and has been shown by Gross, Wilczek and Politzer [3, 4], who were awarded with the Nobel Prize in 2004 for this accomplishment. This regime allows a perturbative treatment and is well described theoretically.

On the other hand, at low energies, the QCD coupling is strong and features like chiral symmetry breaking and confinement emerge. Confinement enforces the absence of free color charges in vacuum, and quarks and gluons only occur as bound states in form of hadrons. Theoretically, confinement is defined by a linearly rising static quark potential. Indirectly, it can be observed in experiment by the absence of free quarks and theoretical calculations show the linear potential but its origin is still unknown. This problem is closely related to one of the Millennium Prize Problems of the Clay Mathematics Institute that requires the proof that Yang-Mills theory exhibits a mass gap $\Delta > 0$ [5]. This mass gap naturally arises in a confining Yang-Mills theory in forms of glueballs

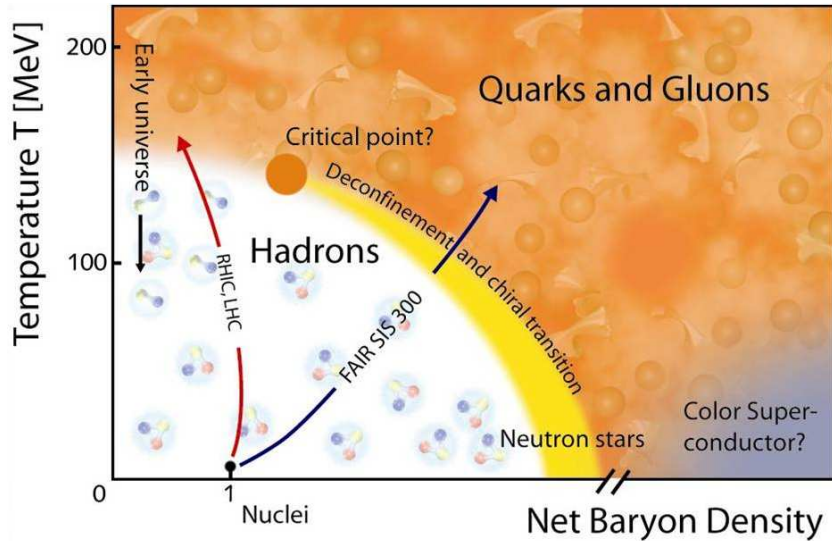


Figure 1.1.: Schematic QCD phase diagram [6].

as effective degrees of freedom. In QCD the confined, hadronic observables are quark-antiquark states called mesons, and baryons which are 3-quark states. Additionally there may be exotic hadrons like glueballs, tetraquarks, pentaquarks or hybrid states.

Another important feature of QCD at low energies are the high effective masses of quarks which reflect in the high masses of the baryons. This can be explained by the spontaneous breaking of chiral symmetry which also explains the existence of light pseudoscalar mesons as Goldstone bosons. At high temperatures chiral symmetry is restored and quarks and gluons are deconfined and form the quark-gluon plasma. These two phases, the hadronic regime at low temperatures and the partonic quark-gluon plasma at high temperatures are separated by a phase transition. At finite density, additional phases are expected to emerge.

The different QCD phases and phase transitions can be visualized in a QCD phase diagram, that shows the favored phases in dependence of temperature and chemical potential. The QCD phase diagram is one of the main objects of interest in QCD [7–9] and a sketch of this diagram is shown in Fig. 1.1. It shows the hadronic region at low temperatures and chemical potential where quarks are confined and chiral symmetry is broken. At high temperature the quark-gluon plasma dominates, where chiral symmetry is restored and quarks and gluons are deconfined. At high chemical poten-

tial various color-superconducting phases emerge which are condensates of quark-quark Cooper pairs. The diagram indicates also the regions of the phase diagram, present and future accelerators can access.

To probe QCD phases experimentally, high energies are required which can be reached in heavy-ion collisions at RHIC at BNL, LHC at CERN and, in the future, at FAIR in Darmstadt. In proton-proton collisions at high energies, a pair of jets is produced, which is a cone of hadrons which were created in the hadronization of a high energy parton and fly in the same direction as the initial parton. As the partons are produced in parton-antiparton pairs which fly in opposite directions, there is always a pair of jets or even more. In heavy-ion collisions at RHIC, it has been found that one of the jets is highly suppressed or absent [10, 11]. This can be interpreted as the loss of energy due to the propagation through a strongly interacting hot and dense medium, which is an evidence for a created quark-gluon plasma. These results could be confirmed with Pb-Pb collisions at LHC [12]. With statistical methods, temperature and chemical potential of the chemical freezeout, where the hadrons are created, can be calculated, which is a rough estimate for the QCD critical temperature (see [13–15] and references therein).

On the theoretical side, precise quantitative predictions can be obtained with lattice QCD. Thereby, the 4-dimensional space-time is discretized on a lattice and the path integral over gluon configurations is sampled numerically with Monte-Carlo simulations. These techniques require large computational effort but give first-principle results of QCD. Though there are still some uncertainties about the convergence to the continuum and infinite volume limit and the effect of fermion discretization, the zero-density regime of QCD can be described well theoretically. The most recent lattice calculations show, that the zero-density transition is a crossover and therefore a smooth transition. The critical temperature therefore depends on the observable and has values of 150 – 160 MeV [16, 17].

At finite density or chemical potential the lattice formulation is not applicable in most cases due to the fermion sign problem. The fermion determinant becomes complex for finite μ and cannot be interpreted as a probability distribution anymore, which spoils the Monte-Carlo simulation. There are ways to extrapolate towards finite density with Taylor expansion, extrapolation from imaginary chemical potential or reweighting methods but these only give access to a small region of finite density [18–22]. Only a few QCD-like theories like 2-color QCD, adjoint fermions and some others allow to prevent the sign problem, however, all of them show some fundamental differences to QCD.

At very high densities the coupling becomes small and QCD can be studied perturbatively with first principles. With weak-coupling methods it can be shown that the ground state of three-flavor QCD at low temperatures is a color-superconducting state in the color-flavor-locked (CFL) phase of symmetrically paired up, down and strange quarks

[23–25]. These methods are only applicable at chemical potentials above a few GeV. Below, many different pairing patterns are expected to play a role. Due to the strong coupling, non-perturbative methods are necessary. Therefore, finite-density regimes are extensively studied in effective models like Nambu–Jona-Lasinio (NJL) or quark-meson models. These models can be tuned to reproduce lattice results at zero density but can calculate finite-density quantities straight forwardly and often also calculations of dynamical quantities in Minkowski space are possible. Usually a first-order phase transition with a critical endpoint at finite densities is predicted. Calculations in the NJL model show a rich phase structure with many different types of color-superconducting condensates [26–28].

Also the possibility of inhomogeneous phases has been investigated (see [29] for a review). The idea of inhomogeneous structures already came up in the sixties by the possibility of inhomogeneous spin-density waves in nuclear matter [30] and later was studied in weak-coupling QCD at large N_c [31, 32]. Calculations in models of strong-coupling QCD also included the possibility of spatially inhomogeneous phases [33–35]. These phases are characterized by a spatially varying chiral symmetry breaking condensate and it was found that these phases cover the first-order phase transition completely. However, these models include some strong simplifications and especially the missing of gluons and dynamical confinement is a fundamental difference to QCD.

A way to investigate QCD directly at finite densities is provided by functional methods like the functional renormalization group (FRG) or Dyson-Schwinger equations (DSEs). In these methods, integral and differential equations for the dressed QCD correlation functions are derived from the QCD generating functional and solved numerically. These equations are exact in general, but not a closed system of equations and therefore can only be solved after specifying a truncation scheme. Truncated DSEs have been solved in vacuum to study ghost and gluon propagators and their IR behavior in Yang-Mills theory and also hadronic observables can be calculated (see [36–41]).

Recently, the study has been extended to finite temperature and density to access the QCD phase diagram with functional methods. The investigation of the chiral and deconfinement transition of QCD thereby is in agreement with lattice-QCD predictions [42, 43]. Similar to model calculations, a first-order chiral phase transition at finite density with a critical endpoint is found [44, 45]. The framework of Dyson-Schwinger equations can be extended to the study of color-superconducting phases as it has been done at zero temperature in [46–48]. These calculations show that the CFL phase is the dominant phase at intermediate chemical potentials and zero temperature. Also FRG calculations (see [49] for a review) show progress in understanding the QCD phase diagram [50] and FRG methods in PQM models predict a similar behavior of the chiral phase transition [51, 52].

The aim of this work is to investigate the QCD phases at finite density with a recent truncation of QCD Dyson-Schwinger equations. In Chapter 2 we introduce the formalism of Dyson-Schwinger equations and color superconductivity. In Chapter 3 we show a simple truncation to solve the system numerically. For the gluon propagator we take lattice data of Yang-Mills calculations and include quark effects with a hard-thermal-loop / hard-dense-loop (HTL-HDL) truncation. This truncation only considers the effects of bare massless quarks on the gluon. This approximation allows to calculate the dressed quark propagator and a phase diagram. In Chapter 4 we improve the truncation by coupling fully dressed quark propagators back to the gluon and also include the effects of quark masses and color-superconducting condensates on the gluon. Again, we investigate the color-superconducting condensates and calculate the phase diagram. Additionally we calculate the gluon screening masses. In Chapter 5 we focus on the chirally broken phase in the HTL-HDL approximation, but allow for an inhomogeneous chiral condensate. We take the most simple ansatz in a 1-dimensional plane wave (chiral density wave) and calculate the phase diagram.

Most of the results shown in Chapter 3 have already been published in [53].

2. QCD and Dyson-Schwinger equations

2.1. QCD basics

Quantum chromodynamics is the fundamental quantum field theory describing quarks and gluons. It is a non-abelian $SU(3)$ gauge theory constrained by renormalizability, local gauge symmetry, locality and Poincare invariance. In Euclidean space it is described by the Lagrangian

$$\mathcal{L}_{QCD} = \bar{\psi} (-\not{D} + m) \psi + \frac{1}{4} F_{\mu\nu}^a F_{\mu\nu}^a \quad (2.1)$$

with the covariant derivative

$$D_\mu = \partial_\mu + igA_\mu^a t^a \quad (2.2)$$

and the field strength tensor

$$F_{\mu\nu}^a t^a = -\frac{i}{g} [D_\mu, D_\nu] = \left(\partial_\mu A_\nu^a - \partial_\nu A_\mu^a - g f^{abc} A_\mu^b A_\nu^c \right) t^a. \quad (2.3)$$

We use the Feynman slash notation $\not{D} = \gamma_\mu D_\mu$. g is the unrenormalized strong coupling constant and $m = \text{diag}\{m_u, m_d, m_s, \dots\}$ the matrix of the unrenormalized (bare) quark masses. The quark spinors $\bar{\psi}, \psi$ have N_f flavor components, $N_c = 3$ color components and are 4-dimensional spinors in Dirac space. They transform according to the fundamental representation of the gauge group $SU(3)$. The gauge or gluon fields A_μ^a live in the adjoint representation of the gauge group. t_a are the 8 generators and f^{abc} the structure constants of that group, defined by $[t^a, t^b] = if^{abc}t^c$.

The generating functional is defined in the path integral formalism

$$Z[\bar{\eta}, \eta, j] = \int \mathcal{D}[\bar{\psi}\psi A] \exp \left(-S_{QCD} + \int d^4x (\bar{\eta}\psi + \bar{\psi}\eta + j_\mu^a A_\mu^a) \right) \quad (2.4)$$

with the external sources $\bar{\eta}, \eta$ and j_μ^a and the classical action

$$S_{QCD} = \int d^4x \mathcal{L}_{QCD}. \quad (2.5)$$

As we work in Euclidean space, the 4-component of x is the imaginary time $x_4 = it$. All correlation functions can be deduced from the generating functional with functional derivatives

$$\langle \mathcal{T}\varphi_i(x_1)\varphi_j(x_2), \dots \rangle = \frac{1}{Z[0]} \frac{\delta^n Z[J]}{\delta J_i(x_1)\delta J_j(x_2)\dots} \quad (2.6)$$

with fields φ_i and corresponding sources J_i .

2.1.1. Gauge fixing

An essential feature of the QCD Lagrangian is its invariance under local gauge transformations

$$\begin{aligned} \psi &\rightarrow U\psi \\ A_\mu^a t^a &\rightarrow U A_\mu^a t^a U^\dagger + \frac{i}{g} (\partial_\mu U) U^\dagger \end{aligned} \quad (2.7)$$

with a space-time dependent $SU(3)$ transformation matrix $U = e^{i\alpha^a(x)t^a}$.

This invariance implies that the integration over the gauge fields in Eq. (2.4) also sums up equivalent gauge configurations that are in the same gauge orbit, defined by

$$(A_\mu^a)^\alpha t^a := \left\{ U A_\mu^a t^a U^\dagger + \frac{i}{g} (\partial_\mu U) U^\dagger \middle| U = e^{i\alpha^a t^a} \in SU(3) \right\} \quad (2.8)$$

and therefore give the same action. This does not generate problems when only using gauge invariant quantities like it is possible in lattice gauge theory. However, methods such as Dyson-Schwinger equations rely on unobservable gauge dependent quantities like quark and gluon propagators and we need a description of these quantities as well. This cannot be done straightforwardly, as a consequence of gauge freedom is that the kinetic part of the gluon in the Lagrangian Eq. (2.1) $A_\mu^a (-\partial^2 g_{\mu\nu} + \partial_\mu \partial_\nu) A_\nu^a$ has vanishing eigenvalues. This spoils the definition of a perturbative gluon propagator $D_{\mu\nu,0}^{ab}(x-y)$, as the defining equation $(-\partial^2 g_{\mu\nu} + \partial_\mu \partial_\nu) D_{\nu\rho,0}^{ab}(x-y) = g_{\mu\rho} \delta^{ab} \delta(x-y)$ has no solution and we need to fix the gauge to overcome that problem. This means, we pick exactly one gluon configuration from each gauge orbit and calculate all quantities for that choice of the gauge. While e.g. propagators are dependent of that choice, observable quantities such as hadron masses, transition temperatures etc. must not be gauge dependent.

We can fix the gauge by using the Faddeev-Popov method introducing the gauge fixing condition

$$f^a(A) - \omega^a(x) = 0 \quad (2.9)$$

such that exactly one configuration of each gauge orbit fulfills that condition¹.

We choose linear covariant gauges $f^a(A) = \partial_\mu A_\mu^a$. This gauge condition can be implemented in the generating functional Eq. (2.4) by inserting

$$1 = \int \mathcal{D}\alpha(x) \delta(f^a(A^\alpha) - \omega^a(x)) \left| \det \frac{\delta f^a(A^\alpha)}{\delta \alpha} \right| \quad (2.10)$$

and after averaging over $\omega^a(x)$ with a Gaussian weight $\exp\left(-\int d^4x \frac{(\omega^a)^2}{2\xi^2}\right)$ we get the result [55]

$$Z[\bar{\eta}, \eta, j, \bar{\sigma}, \sigma] = \int \mathcal{D}[\bar{\psi} \psi A \bar{c} c] \exp \left(\int d^4x (-\mathcal{L}_{gf} + \bar{\eta}\psi + \bar{\psi}\eta + j_\mu^a A_\mu^a + \bar{\sigma}c + \bar{c}\sigma) \right) \quad (2.11)$$

$$\mathcal{L}_{gf} = \mathcal{L}_{QCD} + \frac{1}{2\xi} (\partial_\mu A_\mu^a)^2 - (\partial_\mu \bar{c}^a)(D_\mu^{ab} c^b) \quad (2.12)$$

with the covariant derivative in the adjoint representation

$$D_\mu^{ab} = \partial_\mu \delta^{ab} + g f^{abc} A_\mu^c \quad (2.13)$$

and the auxiliary ghost fields \bar{c} and c . These are unphysical spin-zero Grassmann fields. Together with the unphysical gluon polarizations they have to disappear in the physical spectrum. This is ensured by the BRST symmetry, a remnant of the local gauge symmetry after gauge fixing.

The gauge parameter ξ can be chosen freely. In this work, we use Landau gauge $\xi = 0$, where the gluon field is strictly transverse, i.e. $\partial_\mu A_\mu^a = 0$. Therefore, the gluon propagator is also transverse and as this is not altered by quantum corrections, this gauge is useful for application in Dyson-Schwinger equations.

2.1.2. Renormalization

The gauge fixed QCD Lagrangian Eq. (2.12) is multiplicatively renormalizable and with the introduction of a finite number of renormalization constants all divergencies are cured. After rescaling the fields, the renormalized Lagrangian is given by

$$\begin{aligned} \mathcal{L}_{ren} = & Z_2 \bar{\psi} (-\not{d} + Z_m m) \psi - Z_1 F i g \bar{\psi} \gamma_\mu \frac{\lambda_a}{2} \psi A_\mu^a \\ & + \frac{Z_3}{4} (\partial_\mu A_\nu^a - \partial_\nu A_\mu^a)^2 - Z_1 g f^{abc} (\partial_\mu A_\nu^a) A_\mu^b A_\nu^c + \frac{Z_4}{4} g^2 f^{abe} f^{cde} A_\mu^a A_\nu^b A_\mu^c A_\nu^d \\ & + \tilde{Z}_3 \bar{c}^a \partial^2 c^a + \tilde{Z}_1 g f^{abc} \bar{c}^a \partial_\mu (A_\mu^c c^b) + \frac{Z_3}{2Z_\xi \xi} (\partial_\mu A_\mu^a)^2 \end{aligned} \quad (2.14)$$

¹The Faddeev-Popov procedure does not solve this problem completely and there still remain equivalent configurations called Gribov copies [54] which need to be considered when studying Yang-Mills theory.

and depends only on renormalized fields and couplings. The scaling relation of the fields are

$$\begin{aligned}\bar{\psi}\psi &\rightarrow Z_2\bar{\psi}\psi, & A_\mu^a &\rightarrow Z_3^{1/2}A_\mu^a, & \bar{c}^a c^b &\rightarrow \tilde{Z}_3\bar{c}^a c^b \\ g &\rightarrow Z_g g, & m &\rightarrow Z_m m, & \xi &\rightarrow Z_\xi \xi.\end{aligned}\tag{2.15}$$

The renormalization constants of the vertices are not independent, but constrained by Slavnov-Taylor identities that make use of the BRST invariance of the Lagrangian:

$$Z_{1F} = Z_g Z_2 Z_3^{1/2}, \quad Z_1 = Z_g Z_3^{3/2}, \quad \tilde{Z}_1 = Z_g Z_3^{1/2} \tilde{Z}_3, \quad Z_4 = Z_g^2 Z_3^2 \tag{2.16}$$

In Landau gauge it is also possible to choose $\tilde{Z}_1 = 1$ [56]. This gives the relations $Z_g = \tilde{Z}_3^{-1} Z_3^{-1/2}$ and $Z_{1F} = \frac{Z_2}{Z_3}$.

The correlation functions defined in Eq. (2.6) also inherit the renormalization dependence. The propagators are defined as 2-point correlation functions (see Appendix B) and the quark, gluon and ghost propagators scale with the corresponding renormalization constants $Z_i(\nu, \Lambda)$

$$S(p; \Lambda) = Z_2 S(p; \nu), \quad D_{\mu\nu}^{ab}(k; \Lambda) = Z_3 D_{\mu\nu}^{ab}(k; \nu), \quad G^{ab}(k; \Lambda) = \tilde{Z}_3 G^{ab}(k; \nu) \tag{2.17}$$

with the cutoff Λ and the renormalization scale ν . The quark-gluon vertex has the scaling relation

$$g(\Lambda) \Gamma_\mu^a(p, q; \Lambda) = \frac{1}{Z_2 Z_3^{1/2}} g(\nu) \Gamma_\mu^a(p, q; \nu). \tag{2.18}$$

Using the relation for the coupling $g(\Lambda) = Z_g g(\nu)$, we get

$$\Gamma_\mu^a(p, q; \nu) = Z_{1F} \Gamma_\mu^a(p, q; \Lambda) \tag{2.19}$$

for the dressed quark-gluon vertex.

2.1.3. QCD symmetries

The QCD Lagrangian exhibits a number of important symmetries. As a gauge theory it is invariant under local gauge transformations as indicated in the previous section. Although gauge invariance of the QCD Lagrangian forbids a gluon mass term in the Lagrangian, breaking of Lorentz invariance in the medium can induce effective electric screening masses of the gluons, the Debye masses. These masses only occur at finite temperature or chemical potential and do not spoil gauge invariance of the theory [57]. In a color-superconducting regime it is also possible that the global gauge symmetry

is spontaneously broken². The spontaneous breaking of a symmetry induces massless Goldstone bosons. In case of a gauge symmetry these Goldstone bosons are “eaten” by the gauge bosons and the gluons get a magnetic screening mass through the Anderson-Higgs mechanism [59, 60]. These masses are called Meissner masses.

Another important symmetry of QCD is chiral symmetry. For vanishing bare quark masses $m = 0$, left- and right-handed quarks, defined by

$$\psi_{R,L} = \frac{1 \pm \gamma_5}{2} \psi, \quad (2.20)$$

do not mix and the Lagrangian exhibits a $U_L(N_f) \otimes U_R(N_f)$ symmetry. This symmetry can be expressed as $U_B(1) \otimes U_A(1) \otimes SU_V(N_f) \otimes SU_A(N_f)$ emphasizing the invariance under vector and axial-vector rotations

$$\psi \rightarrow \exp(i\theta_a^V \tau_a) \psi, \quad \psi \rightarrow \exp(i\theta_a^A \gamma_5 \tau_a) \psi \quad (2.21)$$

with $\tau_a \in SU_f(3)$. The corresponding currents, already generalized to finite bare quark masses, are:

$$\partial_\mu j_\mu = \partial_\mu \bar{\psi} \gamma_\mu \psi = 0 \quad (2.22)$$

$$\partial_\mu j_\mu^5 = \partial_\mu \bar{\psi} \gamma_\mu \gamma_5 \psi = 2\bar{\psi} m \gamma_5 \psi - \frac{g^2 N_f}{32\pi^2} \epsilon^{\mu\nu\rho\sigma} F_{\mu\nu}^a F_{\rho\sigma}^a \quad (2.23)$$

$$\partial_\mu j_\mu^a = \partial_\mu \bar{\psi} \gamma_\mu \frac{\tau^a}{2} \psi = \bar{\psi} \left[\frac{\tau^a}{2}, m \right] \psi \quad (2.24)$$

$$\partial_\mu j_\mu^{5,a} = \partial_\mu \bar{\psi} \gamma_\mu \gamma_5 \frac{\tau^a}{2} \psi = \bar{\psi} \gamma_5 \left\{ \frac{\tau^a}{2}, m \right\} \psi \quad (2.25)$$

The $U_B(1)$ current j_μ is always conserved and guarantees baryon number conservation. The vector current j_μ^a is conserved for equal quark masses while the axial and axial-vector currents j_μ^5 and $j_\mu^{5,a}$ are already broken by non-vanishing quark masses. The axial current is additionally broken anomalously by the Adler-Bell-Jackiw anomaly [61, 62] that breaks this current through the quark triangle diagram on the quantum level. This symmetry breaking explains the mass splitting of the η and η' mesons.

In vacuum, a dynamical quark mass is generated through the strong quark-gluon interaction. This dynamical quark mass already arises in the chiral limit and breaks the $SU_A(N_f)$ symmetry spontaneously. According to the Goldstone theorem this causes the

²Only the global gauge symmetry in the gauge fixed theory is broken which is not in contradiction with Elitzur’s theorem [58], which states the impossibility of breaking local gauge symmetries.

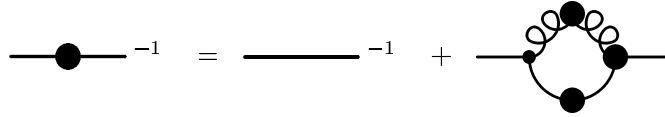


Figure 2.1.: Dyson-Schwinger Equation for the full quark propagator. Plain lines represent quark propagators, the curly line the gluon propagator. Thick dots represent dressed quantities.

occurrence of $N_f^2 - 1$ Goldstone bosons which are the pseudoscalar mesons. They are massless in the chiral limit, for small bare quark masses they have small masses. For $N_f = 2 + 1$ these are the three pions and the heavier four kaons and the eta meson. Chiral symmetry along with gauge symmetry can also be broken in color-superconducting phases.

2.2. Dyson-Schwinger equations

Dyson-Schwinger equations are the quantum equations of motion of a quantum field theory. Exploiting the identity

$$0 = \int \mathcal{D}[\varphi] \frac{\delta}{\delta \varphi_i} \exp(-S_{QCD}[\varphi] + J_j \varphi_j) \quad (2.26)$$

for the variation with respect to different sources φ_i and taking additional variations, the DSEs for all n-point functions can be obtained. For the quark and gluon DSE this is shown in Appendix C. The DSEs are coupled integral equations and obtained without any approximation.

2.2.1. Quark Dyson-Schwinger equation

The DSE for the dressed quark propagator $S(p)$ is depicted in Fig. 2.1 diagrammatically and given by

$$S^{-1}(p; \nu) = Z_2(\nu, \Lambda) (S_0^{-1}(p; \Lambda) + \Sigma(p; \Lambda)). \quad (2.27)$$

The bare propagator is

$$S_0^{-1}(p; \Lambda) = -i\cancel{p} + Z_m(\nu, \Lambda)m_f(\nu) \quad (2.28)$$

where, in general, different bare quark masses $m_f(\nu)$ for the different quark flavors are allowed. The quark self-energy $\Sigma(p; \Lambda)$ is a one-loop diagram including a dressed quark

propagator $S(q; \nu)$, a dressed gluon propagator $D_{\mu\nu}^{ab}(k; \nu)$, a bare $gZ_{1F}(\nu, \Lambda)\gamma_\mu \frac{\lambda^a}{2}$ and a dressed $g\Gamma_\mu^a(p, q; \nu)$ quark-gluon vertex

$$Z_2(\nu, \Lambda)\Sigma(p; \Lambda) = Z_{1F}(\nu, \Lambda)g^2(\nu) \int \frac{d^4 q}{(2\pi)^4} \gamma_\mu \frac{\lambda^a}{2} S(q; \nu) \Gamma_\nu^b(p, q; \nu) D_{\mu\nu}^{ab}(k = p - q; \nu). \quad (2.29)$$

$\lambda^a = 2t^a$ are the 8 Gell-Mann matrices in color space. We use the convention of labeling the quark momenta with p and q and the gluon momentum with k whereas momentum conservation implies $k = p - q$.

An unfortunate feature is that the DSE of an n-point correlation function includes at least one higher n-point function and consequently, the system cannot be closed without a truncation. For the quark DSE the unknown quantities are the dressed gluon propagator and the dressed quark-gluon vertex. In general, the DSEs are an infinite tower of coupled equations and not solvable exactly. We therefore will solve the quark and gluon DSE in an appropriate truncation that will be specified later.

As already indicated on the left-hand side of Eq. (2.29), the self-energy diagram is proportional to Z_2 which is necessary to keep multiplicative renormalizability. This can be seen easily, applying the scaling relations Eq. (2.17) and Eq. (2.19) with the STIs for the renormalization constants Eq. (2.16) to the right-hand side of Eq. (2.29). To fix the remaining renormalization constants Z_2 and Z_m the quark propagator is renormalized by requiring

$$S^{-1}(p; \nu) \Big|_{p^2 = \nu^2} = -i\gamma + m_f(\nu) \Big|_{p^2 = \nu^2} \quad (2.30)$$

at the renormalization point ν . In the chiral limit, the DSE does not depend on Z_m and the mass stays unrenormalized. As Z_m only depends on the cut-off and the renormalization scale and not on the bare quark mass, it can still be determined by extrapolation from finite bare quark masses. In the following, we omit the explicit dependence of the propagators on the renormalization scale ν and the cutoff Λ .

Specifying the dressed gluon and the dressed quark-gluon vertex, the quark DSE can be solved. The inverse quark propagator in vacuum has two dressing functions and can be parametrized by

$$S^{-1}(p) = -i\gamma A(p) + B(p). \quad (2.31)$$

The propagator is often expressed as

$$S(p) = \frac{i\gamma A(p) + B(p)}{p^2 A^2(p) + B^2(p)} =: \frac{Z_q(p)(i\gamma + M(p))}{p^2 + M^2(p)} \quad (2.32)$$

defining the quark wave function renormalization $Z_q(p) = 1/A(p)$ and the renormalization-point independent mass function $M(p) = B(p)/A(p)$.

Investigating QCD in the medium introduces the rest frame of the medium which breaks the $O(4)$ rotational symmetry of the system. Temporal and spatial coordinates or equivalently energy and momentum in Fourier space need to be treated as independent coordinates. Finite temperature T can be introduced by restricting the integration in imaginary time direction to $\beta = 1/T$. In Fourier space this translates to a sum over discrete Matsubara frequencies

$$\int_{-\infty}^{\infty} \frac{dp_4}{2\pi} f(p_4) \rightarrow T \sum_{\omega_n} f(\omega_n). \quad (2.33)$$

The Matsubara frequencies are odd multiples of πT for quarks $\omega_n = (2n+1)\pi T$ due to the anti-periodic boundary conditions of fermions. Bosons obey periodic boundary conditions, therefore the gluon Matsubara frequencies are $\omega_m = 2m\pi T$.

Finite chemical potential is introduced as a Lagrange multiplier that enforces baryon number conservation

$$S_{QCD} \rightarrow \int_0^\beta d\tau \int d^3x (\mathcal{L}_{QCD} + \mu \rho). \quad (2.34)$$

The baryon number density is given by

$$\rho(x) = \psi^\dagger(x)\psi(x) = \bar{\psi}(x)\gamma_4\psi(x) \quad (2.35)$$

and can be absorbed in the free Dirac part of the Lagrangian

$$\mathcal{L}_{QCD,free} + \mu \rho = \bar{\psi}(-\not{d} + m_f + \gamma_4 \mu) \psi. \quad (2.36)$$

Therefore, the bare medium propagator has an energy component shifted by the chemical potential

$$S_0^{-1}(p := (\omega_n, \vec{p})) = -i\gamma_4(\omega_n + i\mu) - i\vec{p} + Z_m m_f. \quad (2.37)$$

The medium quark propagator has an additional dressing function, also reflecting the broken $O(4)$ symmetry

$$S^{-1}(p) = -i\gamma_4(\omega_n + i\mu)C(p) - i\vec{p}A(p) + B(p). \quad (2.38)$$

Finite chemical potential also leads to complex dressing functions. We define the medium mass function by $M(p) = \frac{B(p)}{C(p)}$.

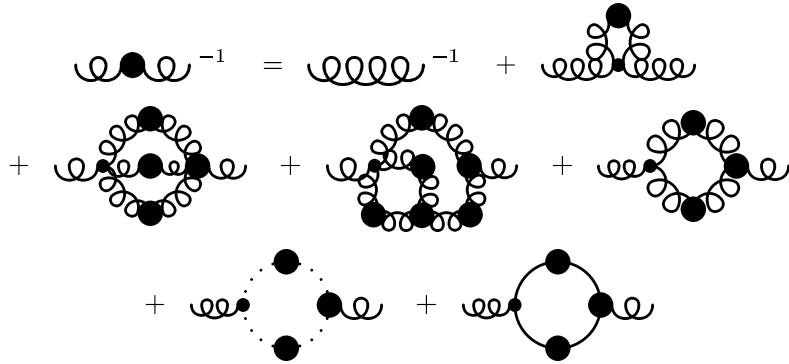


Figure 2.2.: DSE for the gluon propagator. Curly, dotted and plain lines represent gluon, ghost and quark propagators, respectively. Thick dots indicate dressed quantities.

2.2.2. Gluon Dyson-Schwinger equation

The gluon propagator is described by the DSE in Fig. 2.2 and obeys the equation

$$D_{\mu\nu}^{-1,ab}(k) = D_{\mu\nu,0}^{-1,ab}(k) + \Pi_{\mu\nu,YM}^{ab}(k) + \Pi_{\mu\nu,q}^{ab}(k). \quad (2.39)$$

Without the last diagram the equation corresponds to the pure (quenched) Yang-Mills system including a ghost-loop diagram and diagrams involving only gluons that arise due to the possible self-interaction of the gluons. The last diagram describes the coupling to the quarks. Solving the Yang-Mills equations is numerically demanding already without quarks [63–65]. In this work we therefore do not calculate the Yang-Mills diagrams explicitly but investigate the quark contribution to the gluon self-energy, described by the last diagram and given by

$$\Pi_{\mu\nu,q}^{ab}(k) = -Z_{1F}g^2 \int \frac{d^4q}{(2\pi)^4} \text{Tr} \left(\gamma_\mu \frac{\lambda^a}{2} S(p) \Gamma_\nu^b(p, q) S(q) \right). \quad (2.40)$$

We work in Landau gauge where the gluon is strictly transverse and given by

$$D_{\mu\nu}^{ab}(k) = \frac{Z^{ab}(k)}{k^2} T_{\mu\nu} \quad (2.41)$$

in vacuum with the transverse projector

$$T_{\mu\nu} = \left(\delta_{\mu\nu} - \frac{k_\mu k_\nu}{k^2} \right) \quad (2.42)$$

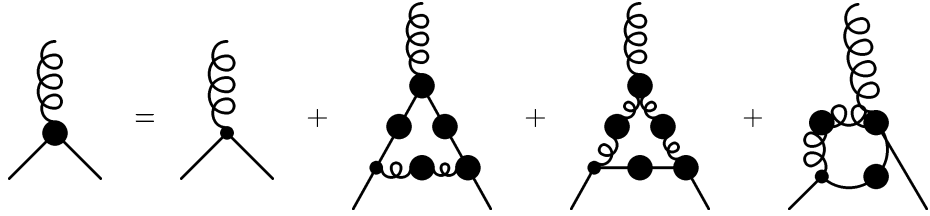


Figure 2.3.: Dyson-Schwinger Equation for the quark-gluon vertex.

and the gluon dressing function $Z^{ab}(k)$ that, in general, may depend on the color channel.

The medium also has influence on the structure of the gluon propagator. In the 4-dimensional transverse subspace the gluon splits up into a 3-dimensional transverse and 3-dimensional longitudinal component, defined via the projectors

$$\begin{aligned} P_{\mu\nu}^T(k) &= \delta_{ij} - \frac{k_i k_j}{k^2} \\ P_{\mu\nu}^L(k) &= \delta_{\mu\nu} - \frac{k_\mu k_\nu}{k^2} - P_{\mu\nu}^T(k). \end{aligned} \quad (2.43)$$

The gluon propagator has in general two different dressing functions proportional to those projectors.

$$D_{\mu\nu}^{ab}(k) = \frac{Z_{TT}^{ab}(k)}{k^2} P_{\mu\nu}^T(k) + \frac{Z_{TL}^{ab}(k)}{k^2} P_{\mu\nu}^L(k). \quad (2.44)$$

2.2.3. Dyson-Schwinger equation of the quark-gluon vertex

The quark-gluon vertex is probably the least known quantity. Its DSE can be expressed as shown in Fig. 2.3 [66]. As already mentioned, a generic feature of the vertex DSE is the occurrence of at least one higher correlation function, here a 2-quark–2-gluon correlation function in the last diagram which prevents getting a closed system of equations. In general, the dressed vertex consists of 10 Dirac components with different dressing functions that depend on 2 external momenta. In medium, there are even more components.

2.3. Effective action, quark condensate and pion properties

The solutions of Dyson-Schwinger equations can also be understood as extremal values of the effective action. The effective action is an interesting quantity as it also allows to judge the stability of the solutions, however, it is not always easy to calculate it. It can

be defined in the CJT formalism [67] by

$$\Gamma[S] = \int_p \text{Tr} \ln S^{-1}(p) - \int_p \text{Tr} (1 - Z_2 S_0^{-1}(p) S(p)) + \Gamma_2[S] \quad (2.45)$$

where Γ_2 incorporates the interaction and is the sum of all 2-particle-irreducible (2PI) diagrams of the dressed quark propagator. The effective action is equivalent to the thermodynamic pressure of the system

$$p = \Gamma[S]. \quad (2.46)$$

The quark DSE can be derived by extremizing the effective action

$$\frac{\delta \Gamma[S]}{\delta S(p)} = 0. \quad (2.47)$$

This also relates $\Gamma_2[S]$ to the quark self-energy

$$\frac{\delta \Gamma_2[S]}{\delta S(p)} = Z_2 \Sigma(p). \quad (2.48)$$

It is always possible to derive DSEs from a given effective action, however, vice versa, not every truncated DSE allows to explicitly define an effective action as it is not always possible to solve Eq. (2.48) analytically for Γ_2 . If the gluon-propagator and the quark-gluon vertex in the quark self-energy Eq. (2.29) do not depend on the quark propagator, which is used in the HTL-HDL approximation, Γ_2 can be determined analytically and is given by

$$\begin{aligned} \Gamma_2 &= Z_{1F} \frac{g^2}{2} \int \frac{d^4 p}{(2\pi)^4} \int \frac{d^4 q}{(2\pi)^4} \text{Tr} \left(\gamma_\mu \frac{\lambda^a}{2} S(q) \Gamma_\nu^b(p, q) D_{\mu\nu}^{ab}(k) S(p) \right) \\ &= \frac{Z_2}{2} \int \frac{d^4 p}{(2\pi)^4} \text{Tr} (\Sigma(p) S(p)). \end{aligned} \quad (2.49)$$

At the stationary point it can also be written as

$$\Gamma_2 = \frac{1}{2} \int_p \text{Tr} (1 - Z_2 S_0^{-1}(p) S(p)). \quad (2.50)$$

The effective action is quartically divergent and can be regularized by calculating the difference between two actions. However, due to the strong divergencies, it is very tedious to perform these integrals numerically and one needs a very high accuracy of the dressing functions.

For the back-coupling of the dressed quark propagator to the gluon, which is investigated in Chapter 4, it is even not possible to get an analytic expression for Γ_2 and it is only formally defined by Eq. (2.48).

The quark condensate is the expectation value of the quark-antiquark fields $\langle\bar{\psi}\psi\rangle$ and defined by [68]

$$\langle\bar{\psi}\psi\rangle = -Z_2 Z_m \int \frac{d^4 p}{(2\pi)^4} \text{Tr} S(p). \quad (2.51)$$

In the chiral limit this quantity is finite, but depends on the renormalization scale. As the renormalization dependence is solely carried by Z_2 and Z_m , it drops out for ratios of condensates which are therefore physical quantities.

For finite bare quark masses, a combination of bare and strange condensate cancels the divergencies and is used in e.g. lattice QCD [69]

$$\langle\bar{\psi}\psi\rangle_{l,s} = \langle\bar{\psi}\psi\rangle_l - \frac{m_l}{m_s} \langle\bar{\psi}\psi\rangle_s \quad (2.52)$$

with the condensate of a light flavor l . Alternatively it is possible to determine the condensate with a fit on the perturbative behavior of the mass function [70]. This also requires a high accuracy of the dressing functions as the condensate is only sensitive to the next-to-leading-order asymptotic behavior of the mass function.

In medium we fix our input quantities by the critical temperature of the chiral phase transition. To get a measure for the quality of the vacuum results, we need to compare with mesonic observables. In the chiral limit, the pion is massless which is ensured if the corresponding symmetries are preserved. In contrast, the pion decay constant also has a finite value in the chiral limit and is a good observable to check the accuracy of the vacuum solution of the DSE. The physical pion has the value of $f_\pi = 92.4 \pm 0.2$ MeV [71], in the chiral limit it is slightly smaller. It can be calculated without solving the pion Bethe-Salpeter equation using the relation [36, 72]

$$f_\pi^2 = \frac{N_c}{4\pi^2} \int_0^\infty dp^2 p^2 \frac{Z_2 A^{-1}(p^2) M(p^2)}{(p^2 + M^2(p^2))^2} \left(M(p^2) - \frac{p^2}{2} \frac{dM(p^2)}{dp^2} \right). \quad (2.53)$$

This equation uses the leading-order Bethe-Salpeter equation for the pion and is valid in the chiral limit but underestimates the pion decay constant by a few percent.

For small explicit chiral-symmetry breaking, the Gell-Mann Oakes Renner relation [73] gives a connection between pion and quark properties

$$f_\pi^2 m_\pi^2 = -m_l \langle\bar{u}u + \bar{d}d\rangle + \mathcal{O}(m_l^2) \quad (2.54)$$

with the pion mass m_π , the light quark mass m_l and the light quark condensate $\langle\bar{u}u + \bar{d}d\rangle$. It is trivially fulfilled in the chiral limit, where $m_l = m_\pi = 0$, and provides the connection between m_l and m_π , when allowing for light quark masses.

2.4. Color superconductivity

In a fermionic system an attractive force between the fermions leads to the formation of bosonic Cooper pairs [74, 75]. This phenomenon is analog to the formation of electron pairs in an electric superconductor. At large enough chemical potential, up and down quarks are nearly massless and therefore have a finite density and the strong force provides an attractive channel for the formation and condensation of diquarks. Due to the complex color, flavor and Dirac structure of the quarks, there are many pairing patterns possible which have been extensively studied in the past [76–82]. The color-superconducting phases are characterized by diquark condensates

$$\langle \psi^T C \gamma_5 \mathcal{O} \psi \rangle. \quad (2.55)$$

$C = \gamma_2 \gamma_4$ is the charge conjugation matrix and \mathcal{O} an operator in color, flavor and Dirac space, specifying the condensate. The combination $C \gamma_5 \mathcal{O}$ needs to be antisymmetric to obey the Pauli principle. We restrict the investigations to scalar spin 0 phases throughout this work. Therefore, \mathcal{O} only acts in color and flavor space. As $C \gamma_5$ is antisymmetric in Dirac space, the overall antisymmetric condition requires \mathcal{O} to be a symmetric operator.

In field theory formalism, color superconductivity can be implemented most easily by introducing the 2-dimensional Nambu-Gor'kov (NG) space and defining bi-spinors

$$\Psi = \frac{1}{\sqrt{2}} \begin{pmatrix} \psi \\ C \bar{\psi}^T \end{pmatrix}, \quad \bar{\Psi} = \frac{1}{\sqrt{2}} (\bar{\psi} \quad \psi^T C). \quad (2.56)$$

The quark spinors are 4-dimensional objects in Dirac space and have $3 \times N_f$ components in color-flavor space, where N_f is the number of flavors. Additionally they have two components in NG space but, by construction, those are not independent and therefore, the degrees of freedom of the theory effectively are not changed. The fermionic part of the Lagrangian can also be formulated in NG space

$$\mathcal{L}_{QCD,q} = \bar{\Psi} \begin{pmatrix} -\not{D} + m_f + \gamma_4 \mu & 0 \\ 0 & -\not{D}_C + m_f - \gamma_4 \mu \end{pmatrix} \Psi \quad (2.57)$$

with the charge conjugate covariant derivative $D_{C,\mu} = -\overleftrightarrow{\partial}_\mu - ig A_\mu^a (t^a)^T$. Deriving the quark DSE by taking the derivatives with respect to the NG spinors instead of the quark spinors gives the DSE for the NG quark propagator

$$\mathcal{S}^{-1}(p) = Z_2 (\mathcal{S}_0^{-1}(p) + \Sigma(p)). \quad (2.58)$$

We also define the NG propagators and self-energies [46, 79]:

$$\mathcal{S}(p) = \begin{pmatrix} S^+(p) & T^-(p) \\ T^+(p) & S^-(p) \end{pmatrix} \quad (2.59)$$

$$\mathcal{S}_0(p) = \begin{pmatrix} S_0^+(p) & 0 \\ 0 & S_0^-(p) \end{pmatrix} \quad (2.60)$$

$$\Sigma(p) = \begin{pmatrix} \Sigma^+(p) & \Phi^-(p) \\ \Phi^+(p) & \Sigma^-(p) \end{pmatrix} \quad (2.61)$$

The components diagonal in NG space represent the normal propagators and self-energies for particles (+) and charge conjugate particles (-), while the off-diagonal components are related to color superconductivity. Therefore, the bare propagator is diagonal in NG space. Without color superconductivity, also the dressed propagator and the self-energy are diagonal and the Dyson-Schwinger system decouples into two equivalent gap equations for the quark propagator and the charge conjugate propagator. On the other hand, if color-superconducting condensates are present, quarks and charge conjugate quarks are coupled.

This becomes evident when we insert the above expressions into the gap equation, Eq. (2.58). One then obtains the following set of equations, which are coupled by the color-superconducting condensates:

$$\begin{aligned} S^{\pm-1} &= Z_2 \left(S_0^{\pm-1} + \Sigma^{\pm} - \Phi^{\mp} (S_0^{\mp-1} + \Sigma^{\mp})^{-1} \Phi^{\pm} \right) \\ T^{\pm} &= - (S_0^{\mp-1} + \Sigma^{\mp})^{-1} \Phi^{\pm} S^{\pm}. \end{aligned} \quad (2.62)$$

The vertices also live in NG space. While the bare vertex is diagonal

$$\Gamma_{\mu}^{a,0} = Z_{1F} \begin{pmatrix} \gamma_{\mu} \frac{\lambda^a}{2} & 0 \\ 0 & -\gamma_{\mu} \frac{\lambda^{a,T}}{2} \end{pmatrix} =: Z_{1F} \gamma_{\mu} \frac{\Lambda^a}{2} \quad (2.63)$$

the full vertex also has off-diagonal elements in general

$$\Gamma_{\mu}^a(p, q) = \begin{pmatrix} \Gamma_{\mu}^{a,+}(p, q) & \Delta_{\mu}^{a,-}(p, q) \\ \Delta_{\mu}^{a,+}(p, q) & \Gamma_{\mu}^{a,-}(p, q) \end{pmatrix}. \quad (2.64)$$

The self-energy integral can also be formulated in NG space

$$Z_2 \Sigma(p) = g^2 T \sum_{\omega_n} \int \frac{d^3 q}{(2\pi)^3} \Gamma_{\mu}^{a,0} \mathcal{S}(q) \Gamma_{\nu}^b(p, q) D_{\mu\nu}^{ab}(k). \quad (2.65)$$

Allowing for color superconductivity also requires additional dressing functions for the

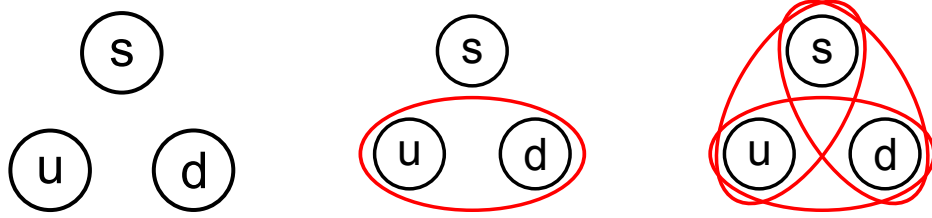


Figure 2.4.: Pairing patterns of 3 quark flavors: unpaired (left), 2SC phase (middle) and CFL phase (right). Colors of the quarks are not illustrated.

propagators [47, 83]

$$\begin{aligned}
 S^{+-1}(p) &= S_i^{+-1}(p)P_i = \sum_i \left(-i\gamma_4(\omega_n + i\mu)C_i^+(p) - i\vec{p}A_i^+(p) + B_i^+(p) - i\gamma_4 \frac{\vec{p}}{|\vec{p}|} D_i^+(p) \right) P_i \\
 T^+(p) &= T_i^+(p)M_i = \sum_i \left(\gamma_4 \frac{\vec{p}}{|\vec{p}|} T_{A,i}^+(p) + \gamma_4 T_{B,i}^+(p) + T_{C,i}^+(p) + \frac{\vec{p}}{|\vec{p}|} T_{D,i}^+(p) \right) \gamma_5 M_i.
 \end{aligned} \tag{2.66}$$

The self-energies Σ^\pm and Φ^\pm are decomposed analogously. For chirally symmetric phases, the $B_i^+(p)$ -dressing functions vanish due to the symmetry. $D_i^+(p)$ as well as $T_{B,i}^+(p)$ and $T_{D,i}^+(p)$ are only non-zero for color-superconducting phases with finite strange-quark masses. P_i and M_i parametrize the phases that are investigated and are matrices in color, flavor and Dirac space in general. For scalar spin 0 phases these matrices are unity in Dirac space. In general, they can be directly related to the operator \mathcal{O} in the condensates Eq. (2.55) and the operator \mathcal{O} is a linear combination of the matrices M_i . The restrictions to these matrices are to obey the residual symmetries of the CSC phases and to be complete in the sense that they yield a closed set of self-consistency equations when inserted into Eq. (2.62), Eq. (2.65) and therefore fulfill

$$\begin{aligned}
 P_i P_j &= \alpha_{ijk} P_k, & M_i M_j &= \beta_{ijk} P_k \\
 P_i M_j &= \gamma_{ijk} M_k, & M_i P_j &= \delta_{ijk} M_k \\
 \lambda_a P_i \lambda_a &= \alpha_{ij} P_j, & \lambda_a^T M_i \lambda_a &= \beta_{ij} M_j
 \end{aligned} \tag{2.67}$$

with constants $\alpha, \beta, \gamma, \delta$.

2.4.1. Structure of color-superconducting phases

The phases of our interest are the 2SC and CFL-like phases. The pairing patterns in flavor space are illustrated in Fig. 2.4. The 2SC phase is characterized by a pairing of

up and down quarks while strange quarks remain unpaired. This phase is dominant in a regime between the chiral phase transitions of up/down and strange quarks where up and down quarks are light and can form Cooper pairs while strange quarks are still too heavy for pairing.

In group theory, the coupling of two fundamental color triplets forms a sextet and an anti-triplet

$$\mathbf{3} \otimes \mathbf{3} = \bar{\mathbf{3}} \oplus \mathbf{6}. \quad (2.68)$$

In the 1-gluon exchange, the sextet channel is repulsive, while the anti-triplet is attractive and therefore provides the attractive force needed to form Cooper pairs. We choose a color structure in the attractive $\bar{\mathbf{3}}$ -channel parametrized by the antisymmetric Gell-Mann matrices $\lambda_{a=2,5,7}$. We therefore need an antisymmetric flavor structure to obtain a symmetric \mathcal{O} in Eq. (2.55). For up and down quarks, this is given by τ_2 and we choose

$$\mathcal{O}_{2SC} = \lambda_2 \otimes \tau_2 \quad (2.69)$$

as we can rotate the color vector λ_a to the $a = 2$ component by the global color symmetry. In the 2SC phase the $SU_c(3)$ color symmetry is broken to a $SU_c(2)$ subgroup. For two flavors the $SU_f(2)$ symmetry stays unbroken, for three flavors the $SU_f(3)$ is broken to $SU_f(2)$.

The matrices P_i and M_i can be obtained by requiring the invariance under the residual symmetry [47]

$$U^\dagger P_i U = P_i, \quad U^T M_i U = M_i \quad (2.70)$$

with U being an element of the the residual symmetry group and choosing a set of matrices being a closed system under Eq. (2.67). For the 2SC phase we can choose

$$M_{2SC} = \lambda_2 \otimes \tau_2 \quad (2.71)$$

parametrizing a condensate of red and green up and down quarks and we close the system with

$$P_{ud,rg} = \lambda_2^2 \otimes \tau_2^2, \quad P_{ud,b} = (\mathbb{1} - \lambda_2^2) \otimes \tau_2^2, \quad P_s = \mathbb{1} - P_{ud,rg} - P_{ud,b} \quad (2.72)$$

where the indices name the quarks represented by the projector. They form a orthonormal basis for the 2SC phase.

For three quark flavors of the same mass, a symmetric pairing is expected to be energetically preferred. In the color-flavor locked (CFL) phase, quarks of all 3 flavors and 3 colors are paired in a totally symmetric way with a residual symmetry of a combined color and flavor rotation described by the $SU_{c+V}(3)$ group with the generators $\tau_a - \lambda_a^T$.

2.4. Color superconductivity

The dominant anti-triplet condensate is parametrized by the antisymmetric Gell-Mann matrices

$$M_{CFL} = \sum_{a=2,5,7} \lambda_a \otimes \tau_a. \quad (2.73)$$

Additionally there is a small contribution in the sextet channel

$$M_6 = \sum_{a=0,1,3,4,6,8} \lambda_a \otimes \tau_a \quad (2.74)$$

with the definition $\lambda_0 = \tau_0 = \sqrt{\frac{2}{3}} \mathbb{1}$.

For the practical calculation it is more convenient to chose a basis in the orthonormal singlet-octet representation [84]

$$P_{sing} = \frac{1}{3} (M_{CFL} M_{CFL} - \mathbb{1}), \quad P_{oct} = \mathbb{1} - P_{sing} \quad (2.75)$$

and

$$M_{sing} = \frac{1}{2} M_{CFL} P_{sing}, \quad M_{oct} = M_{CFL} P_{oct}. \quad (2.76)$$

The anti-triplet and sextet gap functions can then be expressed by³

$$\Phi_{\bar{3}} = \frac{1}{6} \Phi_{sing} + \frac{2}{3} \Phi_{oct}, \quad \Phi_6 = -\frac{1}{6} \Phi_{sing} + \frac{1}{3} \Phi_{oct}. \quad (2.77)$$

In weak-coupling calculations, the sextet gap is often neglected, as is it usually small, which leads to a singlet gap twice the octet gap $\Phi_{sing} = 2\Phi_{oct}$.

With 2 light flavors and a heavier strange quark, the symmetry breaking pattern is more complicated. The strange quark breaks the $SU_f(3)$ flavor symmetry explicitly to $SU_f(2) \otimes U_s(1)$. In a color-superconducting phase, this symmetry, together with the gauge symmetry is broken down to $SU_{c+V}(2) \otimes U_{c+V}(1)$, generated by $\tau_a - \lambda_a^T$ for $a = 1, 2, 3, 8$. The projectors need to interpolate between a 2SC phase that will be the ground state for large strange-quark masses and a CFL phase for massless strange quarks

³Our singlet gap differs by a factor of 2 from the gap defined in [46] as we take the convention of [85].

and we choose [47, 86]⁴

$$P_i = \begin{pmatrix} \delta_{i,1} + \delta_{i,2} & \delta_{i,2} & \delta_{i,4} \\ \delta_{i,2} & \delta_{i,1} + \delta_{i,2} & \delta_{i,4} \\ \delta_{i,5} & \delta_{i,5} & \delta_{i,3} \\ & & \delta_{i,1} \\ & & & \delta_{i,1} \\ & & & & \delta_{i,6} \\ & & & & & \delta_{i,7} \\ & & & & & & \delta_{i,6} \\ & & & & & & & \delta_{i,7} \end{pmatrix} \quad (2.78)$$

$$M_i = \begin{pmatrix} \delta_{i,1} + \delta_{i,2} & \delta_{i,2} & \delta_{i,4} \\ \delta_{i,2} & \delta_{i,1} + \delta_{i,2} & \delta_{i,4} \\ \delta_{i,5} & \delta_{i,5} & \delta_{i,3} \\ & & \delta_{i,1} \\ & & & \delta_{i,1} \\ & & & & \delta_{i,7} \\ & & & & & \delta_{i,6} \\ & & & & & & \delta_{i,7} \end{pmatrix}$$

in the basis

$$\{(r, u), (g, d), (b, s), (r, d), (g, u), (r, s), (b, u), (g, s), (b, d)\}. \quad (2.79)$$

In contrast to the pure 2SC or CFL phase, this basis is not orthonormal and even not orthogonal. The quarks are in a **1** \oplus **1** \oplus **2** \oplus **2** \oplus **3** representation which would predict 5 color-superconducting condensates. We allow for 7 components which are allowed by the restriction of the residual symmetry Eq. (2.70), but it turns out that M_4 and M_5 as well as M_7 and M_8 are not independent for the stable solutions of the DSE and therefore only 5 components are independent.

With these matrices, a 2SC phase can be parametrized, if the condensates fulfill

$$\Phi_1 = -\Phi_2 = \Phi_{2SC}, \quad \Phi_3 = \Phi_4 = \Phi_5 = \Phi_6 = \Phi_7 = 0 \quad (2.80)$$

$$\Sigma_1 = \Sigma_{rg,ud}, \quad \Sigma_3 = \Sigma_6 = \Sigma_s, \quad \Sigma_7 = \Sigma_{ud,b}, \quad \Sigma_2 = \Sigma_4 = \Sigma_5 = 0. \quad (2.81)$$

⁴ Our P_6 and M_6 correspond to P_7 and M_7 in Ref. [47] and our P_7 and M_7 correspond to P_8 and M_8 , while there are no projectors P_6 and M_6 in that reference.

If the strange quarks have the same mass as up and down quark, also a phase exhibiting an exact CFL symmetry can be parametrized, if

$$\Phi_1 = \Phi_6 = \Phi_7 = \Phi_{oct}, \quad \Phi_2 = \Phi_4 = \Phi_5 = -\frac{2}{3}\Phi_{sing} - \frac{1}{3}\Phi_{oct}, \quad \Phi_3 = \frac{2}{3}(\Phi_{oct} - \Phi_{sing}) \quad (2.82)$$

$$\Sigma_1 = \Sigma_6 = \Sigma_7 = \Sigma_{oct}, \quad \Sigma_2 = \Sigma_4 = \Sigma_5 = \frac{1}{3}(\Sigma_{oct} - \Sigma_{sing}), \quad \Sigma_3 = \frac{1}{3}\Sigma_{sing} + \frac{2}{3}\Sigma_{oct}. \quad (2.83)$$

For a different strange-quark mass, a CFL-like pairing pattern is possible. This pairing-type has non-vanishing strange condensates but only approximate CFL symmetry which is explicitly broken by the strange-quark mass difference. However, an exact 2SC pairing is still possible and which pairing type is more stable is chosen dynamically by the system and depends on the strange-quark mass. Finally, also a non-superconducting phase can be described with the constraint

$$\Sigma_1 = \Sigma_7 = \Sigma_{ud}, \quad \Sigma_3 = \Sigma_6 = \Sigma_s \quad (2.84)$$

and all other dressing functions being zero.

2.4.2. Color-superconducting condensates

The color-superconducting condensates, defined by Eq. (2.55)

$$\mathcal{C}_{\mathcal{O}} = \langle \psi^T C \gamma_5 \mathcal{O} \psi \rangle \quad (2.85)$$

can be calculated directly from the NG propagators Eq. (2.59), using the definitions of the NG spinors Eq. (2.56)

$$\mathcal{C}_{\mathcal{O}} = -Z_2 T \sum_{\omega_n} \int \frac{d^3 q}{(2\pi)^3} \text{Tr} (\gamma_5 \mathcal{O} T^-(q)). \quad (2.86)$$

The operator \mathcal{O} can project onto the different pairing patterns. For a pure up and down quark pairing of red and green quarks, as it occurs in the 2SC phase we chose

$$\mathcal{O}_{ud} = \frac{\lambda_2}{2} \otimes \frac{\tau_2}{2}. \quad (2.87)$$

Similarly, the condensates including strange quarks are represented by

$$\mathcal{O}_{uds} = \frac{1}{2} \left(\frac{\lambda_5}{2} \otimes \frac{\tau_5}{2} + \frac{\lambda_7}{2} \otimes \frac{\tau_7}{2} \right). \quad (2.88)$$

For a 2SC phase, only up and down quarks pair, therefore

$$\mathcal{C}_{ud}^{2SC} = -4Z_2 T \sum_{\omega_n} \int \frac{d^3 q}{(2\pi)^3} T_{C,2SC}^- \quad (2.89)$$

is the only condensate and $\mathcal{C}_{uds}^{2SC} = 0$. In contrast, in a phase with three chiral quarks and an exact CFL symmetry, up, down and strange condensates are equal and have the value of the anti-triplet condensate

$$\mathcal{C}_{ud}^{cCFL} = \mathcal{C}_{uds}^{cCFL} = -4Z_2 T \sum_{\omega_n} \int \frac{d^3 q}{(2\pi)^3} T_{C,\bar{3}}^- \quad (2.90)$$

For massive strange quarks, both condensates are independent and the difference between \mathcal{C}_{uds}^{cCFL} and \mathcal{C}_{ud}^{cCFL} indicates the magnitude of the explicit symmetry breaking due to the strange-quark mass. Explicitly the condensates are given by

$$\mathcal{C}_{ud}^{cCFL} = -4Z_2 T \sum_{\omega_n} \int \frac{d^3 q}{(2\pi)^3} \frac{1}{2} \left(T_{C,1}^- - T_{C,2}^- \right) \quad (2.91)$$

$$\mathcal{C}_{uds}^{cCFL} = -4Z_2 T \sum_{\omega_n} \int \frac{d^3 q}{(2\pi)^3} \frac{1}{4} \left(T_{C,6}^- + T_{C,7}^- - T_{C,4}^- - T_{C,5}^- \right). \quad (2.92)$$

2.4.3. Symmetry relations of the propagator

The propagator components and dressing functions carry internal symmetries that are a great simplification for practical calculations. General relations for the propagators can be derived by investigating the definition of the propagators by time ordered expectation values which is for NG propagators

$$\mathcal{S}(x, y) = \langle \mathcal{T} \Psi(x) \bar{\Psi}(y) \rangle. \quad (2.93)$$

Defining the matrices in NG space

$$\mathcal{C} = \begin{pmatrix} 0 & C \\ C & 0 \end{pmatrix}, \quad \Gamma_4 = \begin{pmatrix} \gamma_4 & 0 \\ 0 & \gamma_4 \end{pmatrix} \quad (2.94)$$

the spinors are related by

$$\Psi = \mathcal{C} \bar{\Psi}^T, \quad \bar{\Psi} = \Psi^T \mathcal{C}, \quad \Psi = \Gamma_4 \bar{\Psi}^\dagger, \quad \bar{\Psi} = \Psi^\dagger \Gamma_4. \quad (2.95)$$

With these relations, the transposed Eq. (2.93) gives

$$\mathcal{S}(x, y)^T = -\mathcal{C}\langle \mathcal{T}\Psi(y)\bar{\Psi}(x)\rangle\mathcal{C} = -\mathcal{C}\mathcal{S}(y, x)\mathcal{C} \quad (2.96)$$

or in Fourier space

$$\mathcal{S}(p)^T = -\mathcal{C}\mathcal{S}(-p)\mathcal{C}. \quad (2.97)$$

Similarly, the adjoint expression Eq. (2.93) gives

$$\mathcal{S}(x, y)^\dagger = \Gamma_4\langle \tilde{\mathcal{T}}\Psi(y)\bar{\Psi}(x)\rangle\Gamma_4 = \Gamma_4\mathcal{S}(-y_4, \vec{y}, -x_4, \vec{x})\Gamma_4 \quad (2.98)$$

where $\tilde{\mathcal{T}}$ indicates that the imaginary time ordered path is also changed by the complex conjugation, leading to the minus-sign in the time component. A Fourier transformation of this expression gives the relation

$$\mathcal{S}(p_4, \vec{p})^\dagger = \Gamma_4\mathcal{S}(-p_4, \vec{p})\Gamma_4. \quad (2.99)$$

The two relations Eq. (2.97) and Eq. (2.99) relate the + and - components as well as the propagators at positive and negative energies. Therefore, it is sufficient, if only the +-dressing functions are calculated for $p_4 > 0$.

Relation Eq. (2.97) gives for the NG components

$$\begin{aligned} S^\pm(p) &= -CS^\mp(p)^T C \\ T^\pm(p) &= -CT^\pm(-p)^T C \end{aligned} \quad (2.100)$$

or for the self-energy components

$$\Sigma_{ABCD,i}^+(p) = \Sigma_{ABCD,\tilde{i}}^-(p) \quad (2.101)$$

$$\phi_{ABC,j}^+(p) = \phi_{ABC,\tilde{j}}^+(-p), \quad \phi_{D,j}^+(p) = -\phi_{D,\tilde{j}}^+(-p) \quad (2.102)$$

where \tilde{i} is defined by $P_i^T = P_{\tilde{i}}$ and \tilde{j} by $M_j^T = M_{\tilde{j}}$. This is important for the non-symmetric matrices P_4 , P_5 , M_4 , M_5 , M_7 and M_8 that transform into each other under transposition. The second relation Eq. (2.99) gives

$$\begin{aligned} S^\pm(p_4, \vec{p}) &= \gamma_4 S^\pm(-p_4, \vec{p})^\dagger \gamma_4 \\ T^\pm(p_4, \vec{p}) &= \gamma_4 T^\mp(-p_4, \vec{p})^\dagger \gamma_4 \end{aligned} \quad (2.103)$$

or for the self-energy components

$$\Sigma_{ABC,i}^+(p_4, \vec{p}) = \Sigma_{ABC,\tilde{i}}^+(-p_4, \vec{p})^*, \quad \Sigma_{D,i}^+(p_4, \vec{p}) = -\Sigma_{D,\tilde{i}}^+(-p_4, \vec{p})^* \quad (2.104)$$

$$\phi_{ACD,j}^+(p_4, \vec{p}) = -\phi_{ACD,\tilde{j}}^-(-p_4, \vec{p})^*, \quad \phi_{B,j}^+(p_4, \vec{p}) = \phi_{B,\tilde{j}}^-(-p_4, \vec{p})^*. \quad (2.105)$$

Additionally we require parity invariance for homogeneous phases, formally defined by the spinor transformation $\psi(x_4, \vec{x}) = \gamma_4 \psi(x_4, -\vec{x})$ and giving the relation

$$\begin{aligned} S^\pm(p_4, \vec{p}) &= \gamma_4 S^\pm(p_4, -\vec{p}) \gamma_4 \\ T^\pm(p_4, \vec{p}) &= -\gamma_4 T^\pm(p_4, -\vec{p}) \gamma_4. \end{aligned} \quad (2.106)$$

As the dressing functions are scalar functions they can only depend on $\vec{p}^2 = |\vec{p}|^2$

$$\Sigma_{ABCD}(p) = \Sigma_{ABCD}(p_4, |\vec{p}|), \quad \phi_{ABCD}(p) = \phi_{ABCD}(p_4, |\vec{p}|). \quad (2.107)$$

The vertex exhibits similar properties

$$\Gamma_\mu^a(p, q) = -\mathcal{C} \Gamma_\mu^a(-q, -p)^T \mathcal{C} \quad (2.108)$$

and equivalently its components

$$\begin{aligned} \Gamma_\mu^{a,+}(p, q) &= -C \Gamma_\mu^{a,-}(-q, -p)^T C \\ \Delta_\mu^{a,+}(p, q) &= -C \Delta_\mu^{a,+}(-q, -p)^T C. \end{aligned} \quad (2.109)$$

3. Color-superconducting phases in a HTL-HDL truncation

In the last chapter we have derived the Dyson-Schwinger equations for the quark and gluon propagator and specified the most general ansatz for the propagators. Up to this point, these were exact QCD equations. However, the Dyson-Schwinger system is not a closed system of equations and to solve the system it is still necessary to introduce a truncation. Our main goal is to solve the quark DSE which requires the dressed gluon propagator and the dressed quark-gluon vertex as input quantities. In this section, we introduce our basic truncation scheme, which is based on an HTL-HDL approximation. An improved truncation will be discussed in Chapter 4.

3.1. Truncation of the quark-gluon vertex

The quark-gluon vertex is a complicated object as it has various tensor structures and a dependence on two external momenta, and therefore it is quite involved to solve its DSE. It has been studied on the lattice [87] and also with Dyson-Schwinger equations in semi-perturbative truncations [66, 88]. Recently the coupled system of quark DSE and vertex DSE has been investigated self-consistently in a truncated version in vacuum [89, 90] where the vertex shows, besides a perturbative UV running, a significant IR enhancement. We model this vertex dressing with an ansatz mimicking this behavior.

At this stage, we restrict the vertex to the diagonal NG components and an abelian ansatz that only depends on the gluon momentum $k = p - q$

$$\Gamma_\mu^a(p, q) = \frac{\Lambda^a}{2} \gamma_\mu \Gamma(k) \quad (3.1)$$

with a dressing function $\Gamma(k)$ and the Gell-Mann matrices in NG space Λ^a defined in Eq. (2.63).

For this function, we take a model ansatz, similar to the vertex proposed in [42]

$$\Gamma(k^2) = Z_2 \tilde{Z}_3 \left(\frac{d_1}{d_2 + k^2} + \frac{k^2}{k^2 + \Lambda^2} \left(\frac{\beta_0 \alpha(\nu) \ln(k^2/\Lambda^2 + 1)}{4\pi} \right)^{2\delta} \right). \quad (3.2)$$

The vertex consists of a perturbative logarithmic running with the critical exponents $\beta_0 = (11N_c - 2N_f)/3$ and $\delta = -9N_c/(44N_c - 8N_f)$. The values for the strong coupling $\alpha(\nu) = g^2/4\pi = 0.3$ and the scale factor $\Lambda = 1.4$ GeV are taken from [42]. The first part in the parentheses is an infrared enhancement, necessary to generate chiral symmetry breaking. We take $d_2 = 0.5$ GeV² and fit d_1 to obtain a critical temperature of around 150 MeV for the chiral phase transition at $\mu = 0$ and we get a value of $d_1 = 9.6$ GeV². The vertex in Ref. [42] has additional contributions motivated by a Slavnov-Taylor identity and a Ball-Chiu vertex construction [91]. As there is no strict argument for the necessity of these components, we dropped them as they lead to instabilities in the iteration of color-superconducting phases.

With this vertex and the STI $Z_{1F} = Z_2/\tilde{Z}_3$, the normal and anomalous components of the self-energy Eq. (2.65) become

$$\begin{aligned}\Sigma^+(p) &= 4\pi\alpha(\nu)T \sum_{\omega_n} \int \frac{d^3q}{(2\pi)^3} \frac{\Gamma(k)}{\tilde{Z}_3} \gamma_\mu \frac{\lambda_a}{2} S^+(q) \gamma_\nu \frac{\lambda_b}{2} D_{\mu\nu}^{ab}(k), \\ \Phi^+(p) &= -4\pi\alpha(\nu)T \sum_{\omega_n} \int \frac{d^3q}{(2\pi)^3} \frac{\Gamma(k)}{\tilde{Z}_3} \gamma_\mu \frac{\lambda_a^T}{2} T^+(q) \gamma_\nu \frac{\lambda_b}{2} D_{\mu\nu}^{ab}(k).\end{aligned}\tag{3.3}$$

Note that \tilde{Z}_3 drops out when Eq. (3.2) is inserted.

3.2. Truncation of the gluon DSE

The second quantity to specify for solving the quark DSE is the gluon propagator. In recent years great progress has been made in this sector by combining continuum methods with lattice calculations. In lattice QCD the gluon dressing functions can be calculated in vacuum and at finite temperature in Landau gauge which can serve as an input for the Dyson-Schwinger equations [43, 92]. At finite densities there are no lattice results due to the fermion sign problem, but in the gluon DSE Eq. (2.2) density effects can only originate from the quark-loop diagram. We therefore use the truncation shown in Fig. 3.1 where we take the Yang-Mills result for the gluon propagator from the lattice and include the quark loop perturbatively.

Thereby we include finite temperature and also finite-density effects from the quark propagator but we neglect back-coupling effects of the quark propagator on the Yang-Mills system.

The gluon DSE is then given by

$$D_{\mu\nu}^{-1,ab}(k) = D_{\mu\nu,YM}^{-1,ab}(k) + \Pi_{\mu\nu}^{ab}(k)\tag{3.4}$$

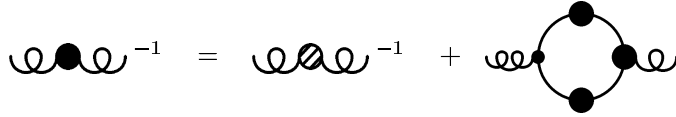


Figure 3.1.: Truncated DSE of the gluon propagator. The shaded propagator is the full Yang-Mills gluon propagator.

$T[\text{MeV}]$	0	100	122	125	152	167
$a_L(T)$	0.60	0.42	0.23	0.33	0.19	0.17
$b_L(T)$	1.36	1.23	1.14	1.20	1.13	1.08
$a_T(T)$	0.60	0.71	0.78	0.83	0.86	1.04
$b_L(T)$	1.36	1.37	1.46	1.47	1.52	1.60

Table 3.1.: Fitting constants of the Yang-Mills gluon dressing function.

with the Yang-Mills gluon propagator $D_{\mu\nu,YM}^{ab}$ and the gluon polarization tensor $\Pi_{\mu\nu}^{ab}$. The former has the same transverse structure as the full gluon Eq. (2.44)

$$D_{\mu\nu,YM}^{ab}(k) = \left(\frac{Z_{TT}^{YM}(k)}{k^2} P_{\mu\nu}^T(k) + \frac{Z_{TL}^{YM}(k)}{k^2} P_{\mu\nu}^L(k) \right) \delta^{ab}. \quad (3.5)$$

The Yang-Mills gluon dressing functions has been extracted from lattice data and fitted by

$$Z_{TT,TL}^{YM}(k) = \frac{k^2 \Lambda^2}{(k^2 + \Lambda^2)^2} \left(\left(\frac{c}{k^2 + a_{T,L} \Lambda^2} \right)^{b_{T,L}} + \frac{k^2}{\Lambda^2} \left(\frac{\beta_0 \alpha(\nu) \ln(k^2/\Lambda^2 + 1)}{4\pi} \right)^\gamma \right). \quad (3.6)$$

The lattice data and fitting constants can be found in [43]. The temperature dependent infrared constants are summarized in Tab. 3.1 and $c = 11.5 \text{ GeV}^2$. We determine their values at other temperatures by linear interpolation. The perturbative logarithmic running is parametrized with the same constants β_0 , $\alpha(\nu)$ and Λ as in the vertex dressing function Eq. (3.2). The critical exponent for the running is given by $\gamma = (-13N_c + 4N_f)/(22N_c - 4N_f)$ and related to δ by $2\delta + \gamma = -1$.

The polarization tensor is given by

$$\Pi_{\mu\nu}^{ab}(k) = -2\pi\alpha(\nu)T \sum_{\omega_n} \int \frac{d^3 q}{(2\pi)^3} \text{Tr} \left(\Gamma_\mu^{a,0} \mathcal{S}(p) \Gamma_\nu^b(p, q) \mathcal{S}(q) \right) \quad (3.7)$$

with $p=k+q$. We already included a factor $\frac{1}{2}$ that compensates for the trace over NG space. As quantum corrections must not change the transverse nature of the gluon (cf. Eq. (2.44) and Eq. (3.5)), we require the polarization tensor to be transverse as well, i.e.

$$\Pi_{\mu\nu}^{ab}(k) = \Pi_{TT}^{ab}(k)P_{\mu\nu}^T(k) + \Pi_{TL}^{ab}(k)P_{\mu\nu}^L(k). \quad (3.8)$$

The dressed gluon propagator is then given by

$$D_{\mu\nu}^{ab}(k) = \frac{Z_{TT}^{YM}(k)}{k^2 + Z_{TT}^{YM}(k)\Pi_{TT}^{ab}(k)}P_{\mu\nu}^T(k) + \frac{Z_{TL}^{YM}(k)}{k^2 + Z_{TL}^{YM}(k)\Pi_{TL}^{ab}(k)}P_{\mu\nu}^L(k). \quad (3.9)$$

Since the gluon polarization tensor has a dependence on the dressed quark propagator, see Eq. (3.7), this equation must, in principle, be solved self-consistently together with the quark DSE. This will be the essential part of the next Chapter 4. However, in a first step, we perform a simple non-self-consistent approximation, which was also employed in Ref. [46, 47].

3.3. HTL-HDL approximation

In this scheme, the quark loop is calculated with bare quarks in a hard-thermal-loop / hard-dense-loop (HTL-HDL) approximation which is numerically a simple way to consider unquenching effects on the gluon propagator. With bare propagators and a vertex Eq. (3.1) the quark contribution Eq. (3.7) simplifies to

$$\Pi_{\mu\nu}^{ab}(k) = -4\pi\alpha(\nu)T \sum_{\omega_n} \int \frac{d^3q}{(2\pi)^3} \text{Tr} \left(\gamma_\mu \frac{\lambda^a}{2} S_0(p) \gamma_\nu \frac{\lambda^b}{2} \Gamma(k) S_0(q) \right). \quad (3.10)$$

In HTL-HDL approximation, the quark-loop integral can be performed analytically under the assumption that the external momenta are small in comparison to temperature $T \gg |k|$ or chemical potential $\mu \gg |k|$. Neglecting the vacuum contributions, the HTL-HDL result can be found in textbooks, e.g. [57] and is given by

$$\begin{aligned} Z_{TT}^{YM}(k)\Pi_T^{ab}(k) &= m_{TT}^2 \frac{\omega_m}{|\vec{k}|} \left[\left(1 + \left(\frac{\omega_m^2}{\vec{k}^2} \right) \right) iQ \left(\frac{i\omega_m}{|\vec{k}|} \right) - \frac{\omega_m}{|\vec{k}|} \right] \delta^{ab} \\ Z_{TL}^{YM}(k)\Pi_L^{ab}(k) &= 2m_{TL}^2 \frac{\omega_m^2 + \vec{k}^2}{\vec{k}^2} \left[1 - \frac{\omega_m}{|\vec{k}|} iQ \left(\frac{i\omega_m}{|\vec{k}|} \right) \right] \delta^{ab} \end{aligned} \quad (3.11)$$

with

$$iQ(ix) = \frac{i}{2} \ln \frac{ix+1}{ix-1} = \arctan \left(\frac{1}{x} \right). \quad (3.12)$$

The effective transverse and longitudinal gluon masses are defined by

$$m_{TT,TL}^2 = N_f \alpha_{TT,TL}(k) \left(\frac{\pi T^2}{3} + \frac{\mu^2}{\pi} \right) \quad (3.13)$$

with the renormalization-point independent strong running couplings, given by (cf. [46])

$$\alpha_{TT,TL}(k) = \frac{\Gamma(k) Z_{TT,TL}^{YM}(k)}{Z_2 \tilde{Z}_3} \alpha(\nu). \quad (3.14)$$

In this approximation, all quark masses and color-superconducting contributions to the polarization tensor are neglected, but, as it provides analytic results for the gluon polarization, it has the advantage to keep the numerical efforts at the same level as in a pure rainbow truncation with quenched gluons. We first present the results for the QCD phases in this truncation.

3.4. Strange-quark mass

The last input quantity to be specified is the strange-quark mass at the renormalization scale ν . According to the particle data group (PDG) [93], its value is $m_s = 95 \pm 5$ MeV in the \overline{MS} renormalization scheme at a renormalization scale of $\nu = 2$ GeV. In earlier Dyson-Schwinger calculations [47] the renormalization point was therefore chosen to be 2 GeV as well, and the PDG value for m_s was directly used as an input. However, the gluon dressings and vertex in this work differ from our input which also has influence on the mass functions. This is illustrated in Fig. 3.2, where the vacuum-mass functions of the (chiral) up and down quarks are shown for the two interactions used in Ref. [47] and for the present setting. An essential difference is that, for these mass functions chiral symmetry is restored at lower momenta and therefore, 2 GeV is already close to the purely perturbative regime, so the perturbative strange-quark mass could be used at this scale.

In contrast, with the improved parametrizations of quark-gluon vertex and gluon propagator used in our calculations, there are still considerable non-perturbative effects at 2 GeV and therefore we have to renormalize at a higher scale to be in the perturbative region. To be on the safe side, we choose $\nu = 100$ GeV. Thus, in order to make contact to the PDG value of the strange-quark mass, we have to evolve it to that higher scale, employing the same perturbative running which was used in the PDG analysis. The scale evolution of the quark mass is then described by the differential equation

$$\nu^2 \frac{dm(\nu)}{d\nu^2} = -\gamma(\alpha(\nu))m(\nu) \quad (3.15)$$

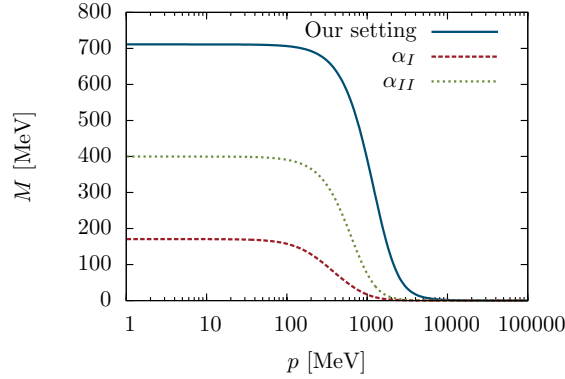


Figure 3.2.: Vacuum mass functions of chiral quarks for the interactions $\alpha_{I,II}$ from [47] and in our setting.

while the coupling obeys the equation

$$\nu^2 \frac{d\alpha(\nu)}{d\nu^2} = \beta(\alpha(\nu)) \quad (3.16)$$

where the functions $\beta(\alpha)$ and $\gamma(\alpha)$ are known to four-loop order for \overline{MS} renormalization [93, 94]. With the initial conditions $m_s(2 \text{ GeV}) = 95 \text{ MeV}$ and $\alpha(M_Z = 91.2 \text{ GeV}) = 0.118$ we integrate Eq. (3.15) to $m_b = 4.2 \text{ GeV}$ with 4 flavors and finally to 100 GeV with 5 flavors, giving $m_s^{\overline{MS}}(100 \text{ GeV}) = 54 \text{ GeV}$. This strange-quark mass was also chosen in [45], although at a slightly lower renormalization scale of 80 GeV . The renormalization scheme used in this work is a momentum subtraction (MOM) scheme which is different from \overline{MS} , however, at high renormalization scales the quark masses have similar values in both schemes.

Additionally, the gluon fit led to a quite large scale Λ (Eq. (3.2), Eq. (3.6)) and it is not clear whether the perturbative strange-quark mass is consistent with our truncation. Therefore, we also consider a different way to estimate the strange-quark mass. Assuming a physical pion mass of $m_\pi = 140 \text{ MeV}$ and calculating the light-quark condensate Eq. (2.51) and pion decay constant Eq. (2.53), we can use the Gell-Mann Oakes Renner (GMOR) relation Eq. (2.54) and calculate the corresponding light-quark mass, which turns out to be $m_l(100 \text{ GeV}) = 1.2 \text{ MeV}$. The ratio of light and strange-quark mass is given by $m_s/m_l = 27.5$ [93] and we get a strange-quark mass of $m_s(100 \text{ GeV}) = 32 \text{ MeV}$.

As the pion decay constant is quite large ($f_\pi = 127 \text{ MeV}$), even without considering that Eq. (2.53) underestimates the true f_π , the application of the GMOR relation seems

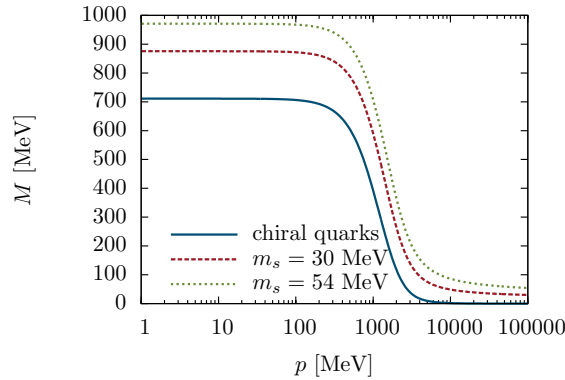


Figure 3.3.: Light and strange-quark mass functions in vacuum.

to be questionable. However, the resulting strange-quark mass of around 30 MeV is similar in the improved truncation in Chapter 4 with a more realistic f_π . We therefore perform calculations for $m_s = 54$ MeV and $m_s = 30$ MeV at our renormalization point of 100 GeV. These values can be seen as upper and lower bounds for the strange-quark mass.

The corresponding quark mass functions for chiral ($m = 0$) and strange quarks ($m = 30$ MeV and $m = 54$ MeV) in vacuum are shown in Fig. 3.3. We find a dressed light-quark mass of $M(0) = 710$ MeV and strange-quark masses of $M(0) = 875$ MeV and $M(0) = 970$ MeV, respectively.¹ These quark masses seem to be quite large in comparison to typical model results. Due to the neglect of the quark masses in the quark loop, the HTL-HDL approximation gives too large gluonic screening masses in the chirally broken phase which would result in very low critical temperatures if we fixed the vertex parameter d_1 in Eq. (3.2) by vacuum quantities. Instead, we chose a larger value for d_1 to raise the critical temperature to $T_c = 150$ MeV with the drawback of getting too large vacuum quantities. However, in the improved truncation in Chapter 4 pion decay constant and quark masses will have smaller values again.

3.5. Results

We perform the calculations for $N_f = 2 + 1$. We take chiral up and down quarks and a strange-quark mass of 30 MeV and 54 MeV at our renormalization point at $\nu = 100$

¹Strictly speaking, these masses are only the screening masses, the pole masses can not be extracted in Euclidean formalism.

GeV as discussed in the last section.

The stable solutions of the DSEs correspond to minima of the thermodynamic potential, or, equivalently, to maxima of the pressure Eq. (2.46). The numerical calculation of the pressure is very unstable due to the initial quartic divergencies. We therefore want to obtain the stable solutions by iterating the DSEs. As argued in Appendix F, the solutions found by solving the DSEs iteratively are expected to correspond to global or local maxima of the pressure, i.e., to stable or metastable solutions, but not to unstable ones. According to this hypothesis (which is usually assumed in DSE calculations), this means that we always find the correct solution in the case of second-order phase transitions.

For first-order phase transitions, there is a regime where both a stable and a metastable solution of the DSEs exist, which both can be found by iteration. The exact position of the phase transition, which manifests itself in a jump between the two solutions, can only be determined by studying the pressure of the system. However, because of the numerical uncertainties mentioned above, this does not further narrow down the phase-transition region in practice. We therefore restrict ourselves to calculating the spinodal lines of the first-order region, i.e., the lines where the metastable solutions disappear. As these regions mostly have only a small extent, they still give a good estimate for the phase transition.

We show results for 2SC and CFL-like pairing and indicate for all quantities in which phase the solutions have been obtained. A CFL solution can only be found when it corresponds to a maximum of the pressure, 2SC solutions can always be found by enforcing a strict 2SC symmetry of the system. In Fig. 3.4 we show the dependence of the color-superconducting condensates on chemical potential at low temperatures 10 MeV. All condensates rise with increasing chemical potential. At low chemical potential we only find a 2SC phase while at a threshold of 500 MeV for $m_s = 30$ MeV or 600 MeV for $m_s = 54$ MeV also a CFL-like solution exists, indicated by a non-zero C_{uds}^{CFL} .

Except for the onset of the CFL-condensation, the condensates show a similar behavior for both strange-quark masses and, in particular, the 2SC condensates are equal in both cases. This is due to the fact, that the quark masses were neglected in the HTL-HDL calculation of the gluon polarization. Therefore, if there is no pairing between light and strange quarks, the strange sector decouples from the light quarks. In contrast, CFL condensates couple light and strange quarks and therefore depend on m_s .

The behavior of the condensates is related to the dependence of the quark mass functions $M(0)$ on chemical potential, shown in Fig. 3.5². At low and intermediate chemical

²Precisely, the masses of red / green and blue quarks differ in the CFL-like phase. However, in the HTL-HDL truncation, this mass splitting is only of the order of 1 MeV and not visible in the resolution of the plot. Additionally, the light quarks have a finite mass in the CFL phase, also of the order of 1 MeV due to the mixing between light and strange quarks.

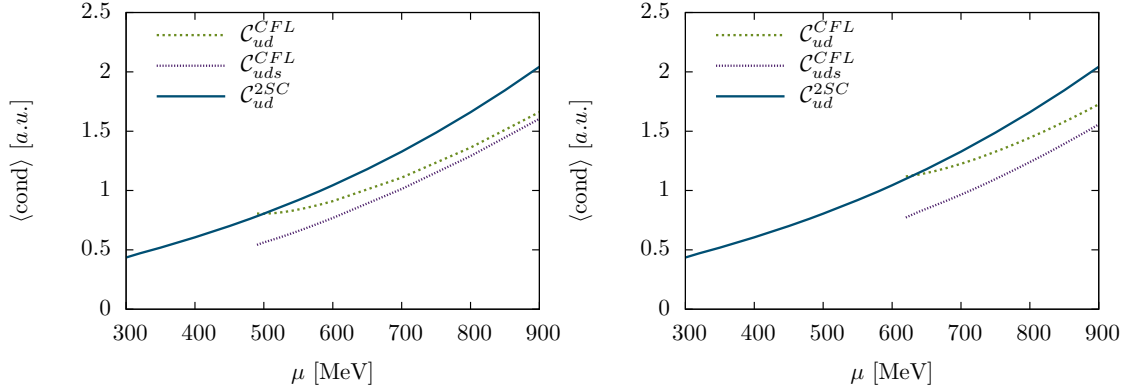


Figure 3.4.: Dependence of 2SC and CFL condensates at $T = 10$ MeV on the chemical potential for $m_s = 30$ MeV (left) and $m_s = 54$ MeV (right). All condensates are given in arbitrary, but equal, units.

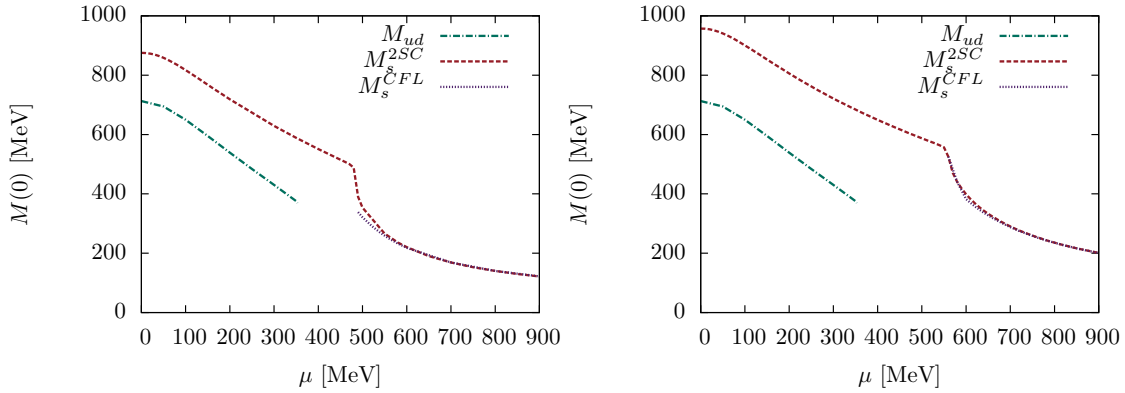


Figure 3.5.: Dependence of light and strange-quark mass functions at $T = 10$ MeV on chemical potential for $m_s = 30$ MeV (left) and $m_s = 54$ MeV (right).

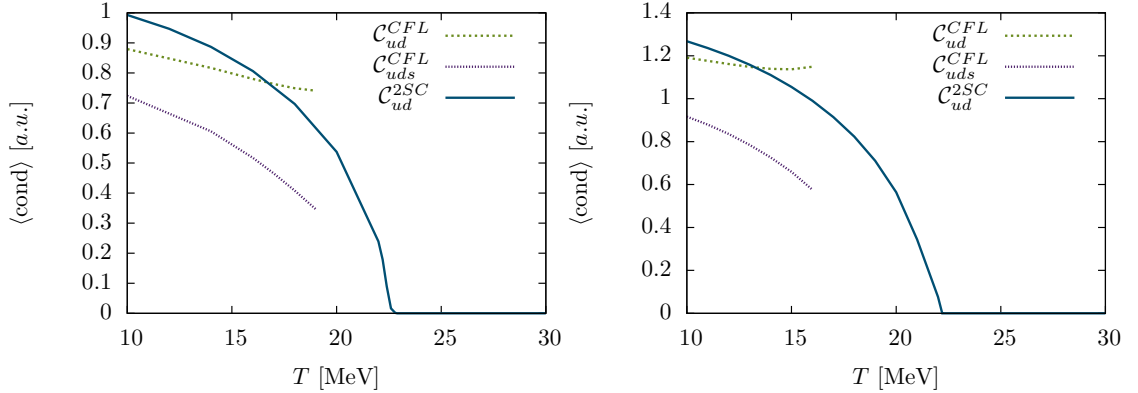


Figure 3.6.: Temperature dependence of 2SC and CFL condensates at $\mu = 580$ MeV for $m_s = 30$ MeV (left) and at $\mu = 680$ MeV for $m_s = 54$ MeV (right). The units are the same as in Fig. 3.4.

potential the strange-quark mass is quite high. This leads to a strong mismatch between the Fermi momenta of light and strange quarks which inhibits CFL pairing. The strange-quark mass smoothly decreases until a crossover transition at $\mu = 500$ MeV for $m_s = 30$ MeV and at $\mu = 600$ MeV for $m_s = 54$ MeV occurs in the 2SC phase. As the strange sector decouples in a 2SC phase, a non-color-superconducting phase shows the same behavior as the 2SC phase and the 2SC condensate $\mathcal{C}_{ud}^{2\text{SC}}$ is not influenced by the drop of M_s in the transition region. The crossover also triggers the onset of a CFL-like solution which has a slightly lower strange quark mass than the mass in the 2SC phase. At higher μ this deviation almost vanishes and purely perturbative behavior of the strange quark dominates. We also show the light quark mass in the chirally broken phase. It decreases with increasing μ until 350 MeV where this solution ceases to exist.

In Fig. 3.6 the dependence of the condensates on temperature is shown at a chemical potential of 580 MeV for $m_s = 30$ MeV and $\mu = 680$ MeV for $m_s = 54$ MeV. The 2SC condensate smoothly decreases with temperature and eventually vanishes at a temperature between $20 - 25$ MeV. The CFL-like phase ceases to exist above a lower critical temperature. The system therefore undergoes a first-order phase transition between the 2SC and CFL-like phase and finally the 2SC phase melts in a second-order transition to the normal conducting phase.

The resulting phase diagrams are shown in Fig. 3.7. As pointed out earlier, in the HTL-HDL approximation, the strange and non-strange sectors decouple, except for the CFL phase, where they are coupled by the condensate. Therefore, the only effect of m_s

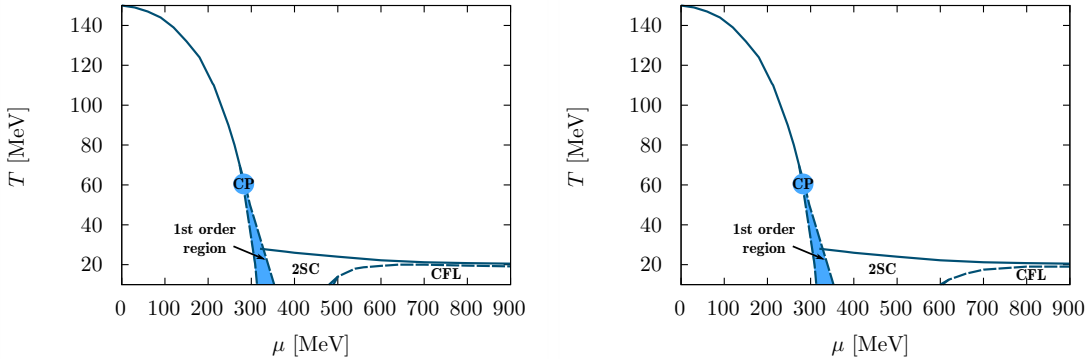


Figure 3.7.: Phase diagram for $m_s = 30$ MeV (left) and $m_s = 54$ MeV (right). The regions of the first-order phase transitions are indicated by shaded areas and bounded by spinodal lines (dashed). Solid lines indicate second-order phase transitions and CP the tricritical point.

on the phase diagram is a shift of the CFL phase boundary while all other transitions are identical for both strange-quark masses.

The shaded areas indicate first-order regions bordered by spinodal lines. The first-order transition is located somewhere in this region. The most prominent ones correspond to the chiral phase transition from the chirally broken phase to the 2SC phase or, at somewhat higher temperatures, to the normal-conducting restored phase (with respect to the up and down quarks). At a tricritical point the two spinodal lines and therefore also the first-order transition line meet. At higher temperatures the transition is of second-order.

The critical point in a similar calculation in [44] differs from our result and is located at a higher temperature ($T = 95$ MeV, $\mu = 280$ MeV) but was calculated for two flavors with a critical temperature of $T_c = 180$ MeV at $\mu = 0$. Additionally the vertex truncation slightly differs in this work. As shown in [45] the inclusion of strange quarks shifts the critical point towards lower temperatures and slightly higher chemical potential which is consistent with our result. However, a direct comparison is not possible, as the calculations in [45] were done without HTL-HDL approximation.

The hadronic part of the phase diagram is mainly shown for completeness, while our focus is on the color-superconducting phases at low temperatures and higher chemical potentials.

Here we find a 2SC phase followed by a CFL-like phase. At $T = 10$ MeV the transition

between these phases happens at a chemical potential of around 500 MeV for $m_s = 30$ MeV and 600 MeV for $m_s = 54$ MeV. At high chemical potential and low temperature, the CFL-like phase is the ground state as it has the larger residual symmetry. At finite temperature the CFL condensates undergo a phase transition to the 2SC phase. This transition is of first-order at low chemical potential, however, it becomes weaker with larger μ and we have numerical indications that at large μ (somewhere around 900 MeV) the phase transition becomes second-order, i.e., the spinodal region ends again in a critical point. Such a behavior was also found in the NJL-model analysis of Ref. [95]. At higher temperatures, the 2SC phase undergoes a second-order transition to the normal conducting chirally restored phase. This transition takes place around 20 and 30 MeV. Remarkably, the critical temperature is slowly decreasing with increasing chemical potential, despite the fact that the zero-temperature condensate increases (cf. Fig. 3.4).

The most important result of this chapter is the occurrence of a stable 2SC phase at low temperatures which is in contrast to the zero-temperature investigations in [47] where the CFL phase was found to be favored in the whole region above the chiral phase transition at $T = 0$. Although our calculations have been performed for $T > 10$ MeV only, a naive extrapolation of the phase boundaries to $T = 0$ does not change our results qualitatively. The difference should therefore mainly be attributed to the improved gluon propagators and vertices, we have used. This truncation generates higher strange quark masses that persist up to higher chemical potential and prevent the pairing of strange quarks.

4. Self-consistent calculation of the gluon propagator

Due to its simplicity the HTL-HDL truncation is a widely applied truncation. The usage of bare quark propagators in the gluon DSE makes it independent of the dressed quark propagator and the numerical effort is similar to a pure rainbow truncation. Nevertheless, it neglects important contributions to the gluon polarization such as those of quark masses and color-superconducting condensates. These approximations can be justified in the perturbative regime at high temperatures and give a reasonable description of the chirally restored phase. However, in the chirally broken phase and at high densities in the color-superconducting regime, an improved description of the gluon polarization would be favorable. We therefore wish to calculate the quark loop in the polarization function with self-consistent fully dressed Nambu-Gor'kov quark propagators, which takes care of these features and restores self-consistency on the level of quark propagators.

4.1. Gluon DSE with self-consistent quarks

We use a similar truncation of the gluon propagator as in the HTL-HDL case but with the essential difference that the quark loop now consists of full NG quark propagators. The Feynman diagrams are shown in Fig. 4.1.

$$\text{Diagram: } \text{Gluon propagator}^{-1} = \text{Gluon propagator}^{-1} + \text{Quark loop diagram}$$

Figure 4.1.: Truncated DSE of the gluon propagator, the shaded propagator is the full Yang-Mills gluon propagator and the quark loop consists of dressed NG quarks.

The quark loop Eq. (3.7)

$$\Pi_{\mu\nu}^{ab}(k) = -2\pi\alpha(\nu)T \sum_{\omega_n} \int \frac{d^3q}{(2\pi)^3} \text{Tr} \left(\Gamma_{\mu}^{a,0} \mathcal{S}(p) \Gamma_{\nu}^b(p, q) \mathcal{S}(q) \right) \quad (4.1)$$

has to be evaluated simultaneously to the iteration of the quark DSE. Calculating this quantity with dressed quark propagators is not as trivial as the quark self-energy as, dependent on vertex truncation and numerical cut-offs, problems like quadratic divergencies and longitudinal components arise. Those need to be cured by an appropriate regularization and renormalization scheme which we will specify in the next sections.

4.2. Renormalization of the gluon DSE

Like the quark self-energy the gluon polarization shows logarithmic divergencies that have to be renormalized. To implement renormalization in our truncation scheme properly, we start by investigating the Yang-Mills gluon DSE in vacuum given by

$$D_{\mu\nu,YM}^{ab,-1}(k) = Z_3 D_{\mu\nu,0}^{ab,-1}(k) + \Pi_{\mu\nu,YM}^{ab}(k) \quad (4.2)$$

with the bare gluon propagator $D_{\mu\nu,0}^{ab}(k) = \frac{1}{k^2} T_{\mu\nu}(k) \delta^{ab}$ and the Yang-Mills gluon self-energy $\Pi_{\mu\nu,YM}^{ab}(k)$. Assuming a transverse, color diagonal self-energy

$$\Pi_{\mu\nu,YM}^{ab}(k) = \Pi_{T,YM}(k) T_{\mu\nu}(k) \delta^{ab} \quad (4.3)$$

the corresponding dressed propagator has the same structure

$$D_{\mu\nu,YM}^{ab}(k) = \frac{Z_{YM}(k)}{k^2} T_{\mu\nu}(k) \delta^{ab} \quad (4.4)$$

with the Yang-Mills dressing function $Z_{YM}(k)$ and the DSE simplifies to

$$Z_{YM}^{-1}(k) = Z_3 + \frac{\Pi_{T,YM}(k)}{k^2}. \quad (4.5)$$

The renormalization condition requires the gluon propagator to be equal to the bare propagator at the renormalization point by

$$Z_{YM}(\nu) = 1 \quad (4.6)$$

which allows to eliminate Z_3 in Eq. (4.5)

$$Z_{YM}^{-1}(k) = 1 + \frac{\Pi_{T,YM}(k)}{k^2} - \frac{\Pi_{T,YM}(\nu)}{\nu^2} \quad (4.7)$$

and gives the dressed Yang-Mills gluon propagator

$$D_{\mu\nu,YM}^{ab}(k) = \frac{1}{k^2 + \Pi_{T,YM}(k) - \frac{k^2}{\nu^2} \Pi_{T,YM}(\nu)} T_{\mu\nu}(k) \delta^{ab}. \quad (4.8)$$

Including the quark loop, we get an additional contribution

$$D_{\mu\nu}^{ab,-1}(k) = Z_3 D_{\mu\nu,0}^{ab,-1}(k) + \Pi_{\mu\nu,YM}^{ab}(k) + \Pi_{\mu\nu}^{ab}(k) \quad (4.9)$$

and, if we assume again a diagonal and transverse quark contribution, we get for the full gluon dressing $Z(k)$

$$Z^{-1}(k) = Z_3 + \frac{\Pi_{T,YM}(k)}{k^2} + \frac{\Pi_T(k)}{k^2} \stackrel{(4.5)}{=} Z_{YM}^{-1}(k) + \frac{\Pi_T(k)}{k^2}. \quad (4.10)$$

Using same renormalization condition as before $Z(\nu) = 1$ and subtracting this condition results in

$$Z^{-1}(k) = 1 + Z_{YM}^{-1}(k) - Z_{YM}^{-1}(\nu) + \frac{\Pi_T(k)}{k^2} - \frac{\Pi_T(\nu)}{\nu^2}. \quad (4.11)$$

It is useful to choose the same renormalization point ν as for the Yang-Mills dressing. Then, $Z_{YM}(\nu) = 1$ and the full renormalized gluon propagator becomes

$$D_{\mu\nu}^{ab}(k) = \frac{Z_{YM}(k)}{k^2 + Z_{YM}(k) \left(\Pi_T(k) - \frac{k^2}{\nu^2} \Pi_T(\nu) \right)} T_{\mu\nu}(k) \delta^{ab} \quad (4.12)$$

and we define the renormalized polarization function by

$$\Pi_{ren}(k) = \Pi(k) - \frac{k^2}{\nu^2} \Pi(\nu). \quad (4.13)$$

It is worth to note that Eq. (4.12) includes no truncation yet and is exact. The approximation we make, is neglecting the dependence of $Z_{YM}(k)$ on the dressed gluon propagator $D_{\mu\nu}^{ab}(k)$ and therefore neglecting the influence of quarks on the Yang-Mills sector. Therefore, this truncation is not fully self-consistent on the level of gluons, but as it does not require to solve the Yang-Mills system, it keeps the numerical effort on a feasible level. However, the gluon DSE and quark DSE are still coupled as the quark propagator contributes to $\Pi_T(k)$.

4.3. Regularization of the quark loop

4.3.1. Regularization for normal phases

Renormalization of the quark loop is necessary to get rid of the logarithmic divergencies naturally arising in a renormalizable QFT. As already mentioned, truncation and also a numerical cutoff can generate additional quadratic divergencies and unphysical longitudinal contributions that need to be cured as well. In full QCD without truncation, regularizing carefully, e.g. with dimensional regularization, these issues are cured automatically. As we need to use a cutoff regularization for our numerical calculations we need to define a regularization scheme to get rid of the quadratic divergencies. This is done such that known results in the weak-coupling limit can be reproduced. Although the gluon propagator must be transverse, the quark loop itself may have longitudinal contributions, if they are canceled by longitudinal contributions of Yang-Mills diagrams, which is ensured by Slavnov-Taylor identities in full QCD. As we truncate the system and especially do not calculate the quark effects on the Yang-Mills system, we do not get this cancellation. Instead we specify a truncation that cures the divergencies and drop all remaining longitudinal quark-loop contributions.

In a first step we therefore investigate the polarization tensor for non-superconducting propagators and introduce the abbreviations

$$\begin{aligned} P_\mu^v &= (C(p)\omega_p, A(p)\vec{p})_\mu \\ N_p &= (P^v)^2 + B^2(p) = C^2(p)\omega_p^2 + A^2(p)\vec{p}^2 + B^2(p). \end{aligned} \quad (4.14)$$

The dressed propagator can then be written as

$$S(p) = \frac{1}{N_p} (i\cancel{P}^v + B(p)). \quad (4.15)$$

After evaluating the traces the polarization function becomes

$$\begin{aligned} \Pi_{\mu\nu}^{ab}(k) &= -\frac{Z_{1F}g^2N_f\delta^{ab}}{2}T \sum_{\omega_n} \int \frac{d^3q}{(2\pi)^3} \\ &\quad \frac{4\Gamma(p, q)}{N_p N_q} \left[-P_\mu^v Q_\nu^v - Q_\mu^v P_\nu^v + \delta_{\mu\nu} (P^v Q^v + B(p)B(q)) \right] \end{aligned} \quad (4.16)$$

where the color trace was evaluated as

$$\text{Tr} \left(\frac{\lambda^a}{2} \frac{\lambda^b}{2} \right) = \frac{1}{2} \delta^{ab}. \quad (4.17)$$

4.3. Regularization of the quark loop

For 2+1 flavors the integral has to be calculated for light and strange quarks separately. In medium, the integral can be decomposed into 3 Lorentz components

$$\Pi_{\mu\nu}^{ab}(k) = \Pi_L^{ab}(k)L_{\mu\nu}(k) + \Pi_{TT}^{ab}(k)P_{\mu\nu}^T(k) + \Pi_{TL}^{ab}(k)P_{\mu\nu}^L(k) \quad (4.18)$$

with the longitudinal projector $L_{\mu\nu} = \frac{k_\mu k_\nu}{k^2}$ and the projections

$$\begin{aligned} \Pi_L^{ab}(k) &= -\frac{Z_{1F}g^2N_f\delta^{ab}}{2}T\sum_{\omega_n}\int\frac{d^3q}{(2\pi)^3}\frac{4\Gamma(p,q)}{N_pN_q}\left(P^vQ^v-2\frac{kP^v\cdot kQ^v}{k^2}+B(p)B(q)\right) \\ \Pi_{TT}^{ab}(k) &= -\frac{Z_{1F}g^2N_f\delta^{ab}}{2}T\sum_{\omega_n}\int\frac{d^3q}{(2\pi)^3}\frac{4\Gamma(p,q)}{N_pN_q}\left(P^vQ^v-2A(p)A(q)q_1^2+B(p)B(q)\right) \\ \Pi_T^{ab}(k) &= -\frac{Z_{1F}g^2N_f\delta^{ab}}{2}T\sum_{\omega_n}\int\frac{d^3q}{(2\pi)^3}\frac{4\Gamma(p,q)}{N_pN_q}\left(\frac{1}{3}P^vQ^v+\frac{2}{3}\frac{kP^v\cdot kQ^v}{k^2}+B(p)B(q)\right) \\ \Pi_{TL}^{ab}(k) &= 3\Pi_T^{ab}(k)-2\Pi_{TT}^{ab}(k). \end{aligned} \quad (4.19)$$

At this point the problems are visible. The integrals are quadratically divergent and a longitudinal contribution of the polarization function occurs. To investigate these problems further we simplify the longitudinal part using bare propagators and a bare vertex in vacuum

$$\Pi_{L,bare}^{ab}(k) = -\frac{8\pi N_f\delta^{ab}}{k^2}\int\frac{d^4q}{(2\pi)^4}\left(\frac{kp}{p^2}-\frac{kq}{q^2}\right). \quad (4.20)$$

Recalling that $p = k + q$, it can be seen that this integral vanishes analytically when performing the shift of the integration variable $q \rightarrow q - k$ in the first term, guaranteeing the transverseness in the HTL-HDL approximation. Applying similar transformations to Π_T^{ab} and Π_{TT}^{ab} , it can be shown that this also cures the quadratic divergencies. This mechanism is spoiled when using a cutoff for numerical calculation as this prevents the shift of the integration variable. Using a cutoff Λ in the q -integration the integral gives

$$\begin{aligned} \Pi_{L,bare}^{ab,\Lambda}(k) &= \frac{N_f\delta^{ab}}{12\pi}(k^2-3\Lambda^2) \\ \Pi_{T,bare}^{ab,\Lambda}(k) &= \frac{N_f\delta^{ab}}{12\pi}\left(\frac{8}{3}k^2-3\Lambda^2+2k^2\log\left(\frac{\Lambda^2}{k^2}\right)\right). \end{aligned} \quad (4.21)$$

We therefore need a regularization that removes the longitudinal contribution and also the cutoff dependence. We use a scheme similar to one proposed by Brown and Pen-

nington [96], defined by the projection

$$\Pi_{reg}^{ab}(k) = \frac{1}{3} \left(\delta_{\mu\nu} - 4 \frac{k_\mu k_\nu}{k^2} \right) \Pi_{\mu\nu}^{ab}(k) = \Pi_T^{ab}(k) - \Pi_L^{ab}(k) =: \Pi_{T,reg}^{ab}(k). \quad (4.22)$$

It is also possible to subtract $\Pi_L^{ab}(0)$ instead of $\Pi_L^{ab}(k)$ which gives the same result for bare quarks after renormalization with Eq. (4.13), as

$$\Pi_T^{ab}(k) - \Pi_L^{ab}(k) - \frac{k^2}{\nu^2} \left(\Pi_T^{ab}(\nu) - \Pi_L^{ab}(\nu) \right) = \Pi_T^{ab}(k) - \Pi_L^{ab}(0) - \frac{k^2}{\nu^2} \left(\Pi_T^{ab}(\nu) - \Pi_L^{ab}(0) \right) \quad (4.23)$$

is fulfilled for Eq. (4.21). This regularization only removes a constant contribution $c\Lambda^2$ also for dressed quarks and only the divergent contribution is subtracted. We use this scheme in the following and define the regularized and renormalized polarization functions $\Pi_r(k)$ generally as

$$\Pi_{TT/TL,r}^{ab}(k) = \Pi_{TT/TL}^{ab}(k) - \Pi_L^{ab}(0) - \frac{k^2}{\nu^2} \left(\Pi_{TT/TL}^{ab}(\nu) - \Pi_L^{ab}(0) \right). \quad (4.24)$$

For bare quarks, we get a regularized transverse polarization function that reproduces HTL-HDL results and gives the renormalized vacuum expression

$$\Pi_{T,r}^{ab}(k) = -\frac{N_f \delta^{ab}}{6\pi} k^2 \log \left(\frac{k^2}{\nu^2} \right). \quad (4.25)$$

This is the same result as obtained in textbooks [55] in dimensional regularization and therefore an appropriate way of regularizing the integral. This scheme also ensures vanishing Meissner masses¹ $m_{M,ab}^2 = \Pi_{TT,r}^{ab}(0)$, required for an unbroken gauge symmetry. This can be seen in a short calculation, taking the limits $k_4 = 0$ and $\vec{k} \rightarrow 0$ in Eq. (4.19) and performing the angular integration.

To preserve renormalizability, the vertex dressing function $\Gamma(p, q)$ also must not depend solely on the gluon momentum. In that case $\Gamma(p, q) = \Gamma(k^2)$, the vertex dressing function does not depend on the integration variable and would result in a renormalized polarization

$$\Pi_{T,r}^{ab}(k) = \frac{N_f \delta^{ab}}{6\pi} \left(\frac{5}{6} k^2 (\Gamma(k^2) - \Gamma(\nu^2)) + k^2 \left(\log \left(\frac{\Lambda^2}{k^2} \right) \Gamma(k^2) - \log \left(\frac{\Lambda^2}{\nu^2} \right) \Gamma(\nu^2) \right) \right). \quad (4.26)$$

¹For a more detailed study of the Meissner and Debye masses, see Section 4.6

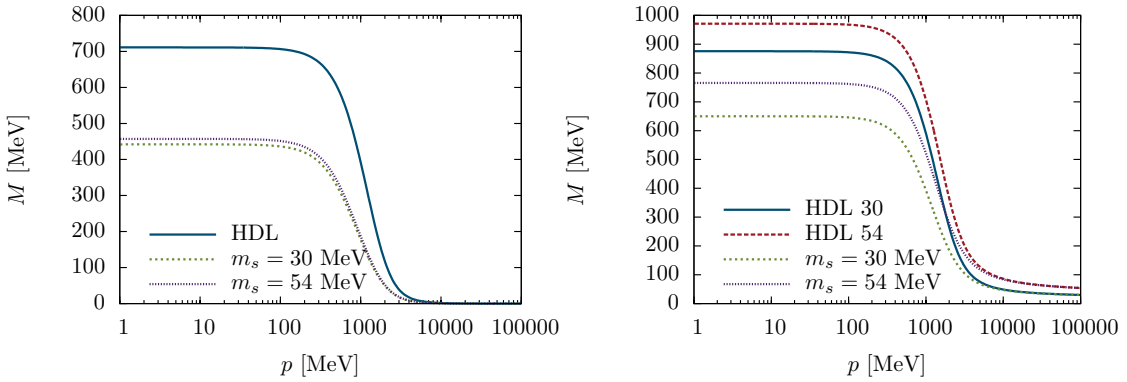


Figure 4.2.: Vacuum quark mass functions for light quarks (left) and strange quarks (right) for the HTL-HDL approximation (for $m_s = 30$ MeV and $m_s = 54$ MeV) in comparison with the self-consistent calculation.

This expression still has a logarithmic divergence². We therefore take the momentum dependence

$$\Gamma(p, q) = \Gamma(p^2 + q^2) \quad (4.27)$$

with the dressing function Eq. (3.2) in the gluon polarization with an explicit dependence on both quark momenta p and q and preserve renormalizability with Eq. (4.13). We also need to adjust the value of d_1 in Eq. (3.2) and take $d_1 = 14$ GeV², which leads to a chiral critical temperature of $T_c \approx 150$ MeV at $\mu = 0$.

Using this scheme in the vacuum quark DSE, we get quark mass functions that are significantly smaller than in the HTL-HDL approximation (Fig. 4.2).

With the back-coupling of the quarks, the strange quark also has influence on the light quarks as seen in the left figure, but this is only a minor effect. The light masses are now around $M(0) = 450$ MeV while the pion decay constant is also smaller and around $f_\pi = 95$ MeV which is a much more realistic value than that of the HTL-HDL approximation. The self-consistent treatment of the quarks in the gluon DSE therefore has important influence on the vacuum observables. Estimating the strange-quark mass with the GMOR relation as done in Section 3.4 gives a similar value of $m_s = 33$ MeV, but now with a quite realistic pion decay constant and therefore justifies the application of the GMOR relation.

The strange quark naturally has a bigger dependence on the bare strange mass. The

²Only a modified vertex-dependent renormalization condition $\Pi(k) - \frac{k^2 \Gamma(k^2)}{\nu^2 \Gamma(\nu^2)} \Pi(\nu)$ would result in finite expressions.

bare masses of 30 and 54 MeV lead to a difference of the dressed masses of around 100 MeV for both approximations. Similar to the light quarks, the improved gluon leads to a strong decrease of the quark mass.

4.3.2. Regularization for full NG propagators

The regularization specified in the last chapter works well for non-superconducting phases and can reproduce weak-coupling results. For superconducting phases, it turns out that this scheme still neglects important contributions. For 2SC and CFL phases, some interesting features for Debye and Meissner masses have been found in [85, 97] in the weak-coupling limit. In a two-flavor 2SC phase, gluons with different colors have different Debye and Meissner masses due to the unsymmetric breaking of color symmetry. The gluons with color index 1-3 are special as they have both vanishing Debye and Meissner masses. As they represent the unbroken $SU_c(2)$ subgroup of color symmetry the Meissner masses need to vanish. Additionally, these gluons only couple to red or green quarks, which are all bound in Cooper pairs. This also suppresses the Debye mass of these gluons. Furthermore the relative value of the gluon masses in comparison to the HTL-HDL gluon masses could be calculated for the 2SC and CFL phase. These features can be reproduced in our formalism if we improve our vertex truncation. We therefore investigate the Slavnov-Taylor identity (STI) for the quark-gluon vertex [98], which connects the quark propagator and the quark-gluon vertex with the ghost propagator $G(k)$ and the ghost-gluon vertex $H^a(p, q)$

$$-iG^{-1}(k)k_\mu\Gamma_\mu^a(p, q) = \mathcal{S}^{-1}(p)H^a(p, q) - H^a(p, q)\mathcal{S}^{-1}(q). \quad (4.28)$$

As we do not solve the Yang-Mills system explicitly we cannot implement the STI directly. Instead, as a truncation, we construct a vertex and a regularization, that keep the most important features of the polarization by exploiting the STI in a limiting case. If we assume $H^a(p, q) = g(p, q)\frac{\Lambda^a}{2}$ the STI reduces to a restriction similar to the Ward-Takahashi identity in QED, except for a multiplicative scalar function $f(p, q)$

$$-ik_\mu\Gamma_{\mu,BC}^a(p, q) = \mathcal{S}^{-1}(p)\frac{\Lambda^a}{2} - \frac{\Lambda^a}{2}\mathcal{S}^{-1}(q). \quad (4.29)$$

This can be used to give constraints to the quark-gluon vertex as proposed by Ball and Chiu [91]. The Ball-Chiu vertex therefore ensures a transverse quark contribution to the gluon polarization and fulfills

$$k_\mu k_\nu \Pi_{\mu\nu}^{ab}(k) = 0. \quad (4.30)$$

This is a strict requirement in QED while in QCD it is only an approximate criterion as longitudinal parts are allowed in principle as discussed before. We do not require

Eq. (4.29) to be fulfilled in general but use it as a guide to construct the vertex. We use the simple color-superconducting self-energy

$$\phi^+(p) = \phi_i \gamma_5 M_i \quad (4.31)$$

with $M_i = M_{2SC}$ and $M_i = M_{sing/oct}$ for a 2SC and a CFL phase, respectively, and the corresponding gaps ϕ_i . These self-energies are also used in weak-coupling calculations and we construct the exact Ball-Chiu vertex for this propagator.

We can rewrite Eq. (4.29) as

$$\begin{aligned} -ik_\mu \Gamma_{\mu,BC}^a(p,q) &= (\mathcal{S}^{-1}(p) - \mathcal{S}^{-1}(q)) \frac{\Lambda^a}{4} + \frac{\Lambda^a}{4} (\mathcal{S}^{-1}(p) - \mathcal{S}^{-1}(q)) \\ &+ (\mathcal{S}^{-1}(p) + \mathcal{S}^{-1}(q)) \frac{\Lambda^a}{4} - \frac{\Lambda^a}{4} (\mathcal{S}^{-1}(p) + \mathcal{S}^{-1}(q)). \end{aligned} \quad (4.32)$$

The first line are contributions similar to those also occurring for normal propagators. It gives the bare vertex γ_μ for bare propagators or propagators with constant mass or color-superconducting gap functions like our test propagator Eq. (4.31). The second line only contributes for propagators non-trivial in color space. The gap functions give additional contributions to the vertex

$$\Gamma_{\mu,CSC}^a = \frac{ik_\mu}{4k^2} \begin{pmatrix} 0 & -(\phi_i^-(p) + \phi_i^-(q))(\lambda^a M_i + M_i \lambda^{a,T}) \\ (\phi_i^+(p) + \phi_i^+(q))(\lambda^{a,T} M_i + M_i \lambda^a) & 0 \end{pmatrix}. \quad (4.33)$$

For our calculation with full NG quarks we therefore use the vertex

$$\Gamma_\mu^a(p,q) = \left(\gamma_\mu \frac{\Lambda^a}{2} + \Gamma_{\mu,CSC}^a \right) \Gamma(p,q) \quad (4.34)$$

with the full anomalous self-energies Φ^\pm in the vertex Eq. (4.33).

It is worth to note that the the anomalous vertex contributions $\Gamma_{\mu,CSC}^a$ are proportional to k_μ and vanish for every transverse projection. Therefore, they do not contribute to the quark DSE and in the gluon polarization they only contribute to the longitudinal component $\Pi_L^{ab}(k)$ and enter through the regularization condition Eq. (4.24).

4.4. Evaluating the quark loop

Using the NG propagators Eq. (2.59) and the vertex Eq. (2.64) the NG trace of the quark loop Eq. (3.7) can be performed, giving the contributions (details are shown in Appendix D)

$$\begin{aligned}
\Pi_{\mu\nu}^{ab}(k) = & -Z_{1F}4\pi\alpha(\nu)T \sum_{\omega_n} \int \frac{d^3q}{(2\pi)^3} \\
& \left\{ \text{Tr} \left[\gamma_\mu \frac{\lambda^a}{2} S^+(p) \gamma_\nu \frac{\lambda^b}{2} \Gamma(p, q) S^+(q) \right] - \text{Tr} \left[\gamma_\mu \frac{\lambda^a}{2} T^-(p) \gamma_\nu \frac{\lambda^{b,T}}{2} \Gamma(p, q) T^+(q) \right] \right. \quad (4.35) \\
& \left. + \text{Tr} \left[\gamma_\mu \frac{\lambda^a}{2} S^+(p) \Delta_\nu^{b,-}(p, q) T^+(q) \right] + \text{Tr} \left[\gamma_\mu \frac{\lambda^a}{2} T^-(p) \Delta_\nu^{b,+}(p, q) S^+(q) \right] \right\}.
\end{aligned}$$

For a pure CFL phase the color-flavor traces give a diagonal gluon polarization in color space. For a 2SC phase or a CFL-like phase with massive strange quarks the situation is more difficult. In these cases, the quark loop can have non-diagonal contributions in color space. In general, block structures arise for $(a, b) \in \{4, 5\}$ and $(a, b) \in \{6, 7\}$ with the structure

$$\begin{pmatrix} \Pi_{\mu\nu}^{44}(k) & \Pi_{\mu\nu}^{45}(k) \\ \Pi_{\mu\nu}^{54}(k) & \Pi_{\mu\nu}^{55}(k) \end{pmatrix} \quad (4.36)$$

and the properties $\Pi_{\mu\nu}^{44}(k) = \Pi_{\mu\nu}^{55}(k)$ and $\Pi_{\mu\nu}^{45}(k) = -\Pi_{\mu\nu}^{54}(k)$. These blocks can be diagonalized using the unitary matrix [97]

$$u = \frac{1}{\sqrt{2}} \begin{pmatrix} 1 & -i \\ -i & 1 \end{pmatrix}. \quad (4.37)$$

Therefore, the matrix U with a block u on the diagonal for the 4–5 and 6–7 component and a 1 on all other diagonal elements diagonalizes the polarization tensor in color space by

$$\Pi_{\mu\nu, \text{diag}}^{ab}(k) = U_{aa'}^\dagger \Pi_{\mu\nu}^{a'b'}(k) U_{b'b}. \quad (4.38)$$

After diagonalization, the first contribution in Eq. (4.35) therefore has the color trace

$$U_{aa'}^\dagger \text{Tr}_{cf} \left(\lambda^{a'} P_i \lambda^{b'} P_j \right) U_{b'b} = \text{Tr}_{cf} \left((U^\dagger \lambda)^a P_i (U \lambda)^b P_j \right) \quad (4.39)$$

where we used the symmetry $U^T = U$. The other contributions give analogous results and it is useful to absorb U into the Gell-Mann matrices

$$\begin{aligned}
(U^\dagger \lambda)^a &= \left(\lambda_1, \lambda_2, \lambda_3, \frac{\lambda_4 + i\lambda_5}{\sqrt{2}}, \frac{\lambda_5 + i\lambda_4}{\sqrt{2}}, \frac{\lambda_6 + i\lambda_7}{\sqrt{2}}, \frac{\lambda_7 + i\lambda_6}{\sqrt{2}}, \lambda_8 \right)^a \\
(U \lambda)^b &= \left(\lambda_1, \lambda_2, \lambda_3, \frac{\lambda_4 - i\lambda_5}{\sqrt{2}}, \frac{\lambda_5 - i\lambda_4}{\sqrt{2}}, \frac{\lambda_6 - i\lambda_7}{\sqrt{2}}, \frac{\lambda_7 - i\lambda_6}{\sqrt{2}}, \lambda_8 \right)^b
\end{aligned} \quad (4.40)$$

and interpret the diagonal gluon polarization function just as the polarization in a different basis in color space. In the quark DSE Eq. (2.65), the color-flavor structure with the diagonal gluon gives

$$\lambda^a P_i \lambda^b U_{aa'} D_{\mu\nu,diag}^{a'b'}(k) U_{b'b}^\dagger = (U\lambda)^{a'} P_i (U^\dagger \lambda)^{b'} D_{\mu\nu,diag}^{a'b'}(k) \quad (4.41)$$

and only the diagonal gluon and the rotated Gell-Mann matrices emerge. Requiring the conditions for P_i and M_i Eq. (2.67) in this new system gives no change in the CFL parametrization but requires a new projector for the 2SC phase. The strange-quark projector P_s now splits into a strange-blue projector $P_{s,b} = (\mathbb{1} - \lambda_2^2) \otimes (\mathbb{1} - \tau_2^2)$ and a non-blue strange projector $P_{s,rg} = P_s - P_{s,b}$. This requirement of an additional projector is also intuitive, as the symmetry breaking between red / green and blue quarks, significant in the 2SC condensates, is also carried over to the strange sector via the gluon. In the HTL-HDL approximation this was not visible, as the strange quark decoupled from the light sector in the 2SC phase.

4.5. Results

Using the full quark propagator in the quark loop we can present results of the coupled quark and gluon DSE system. The dependence of the diquark condensates on chemical potential at $T = 10$ MeV is shown in Fig. 4.3. The condensates are qualitatively similar to the HTL-HDL case, except that with the back-coupling of the full quark propagator to the glue sector the strange quark has a stronger influence on the color-superconducting condensates. While the CFL condensates can only be formed with light strange quarks, 2SC pairing is also possible for heavy strange quarks. When restricting to the 2SC phase, a discontinuity is visible in the 2SC condensate which corresponds to the strange quark phase transition, as strange and light quarks are coupled due to the quark loop in the gluon DSE. At small T this transition is of first-order and the figure shows both branches of the 2SC condensate in the spinodal region. The first-order phase transition is located somewhere between the two branches. This transition leads to a small decrease of the 2SC condensates and is located around $\mu = 600$ MeV for $m_s = 30$ MeV and $\mu = 700$ MeV for $m_s = 54$ MeV. An unfortunate feature of the truncation used here is the much larger extent of the spinodal regions in contrast to the HTL-HDL approximation. However, the calculation of the pressure, that could provide the location of the first-order transition is not possible as, in addition to the numerical problems in the HTL-HDL approximation, there is even no analytic expression for the interaction Γ_2 Eq. (2.49), as our truncation involves a non-trivial dependence of the vertex and gluon on the quark propagator. Therefore, we cannot constrain the first-order transition to a smaller region. However,

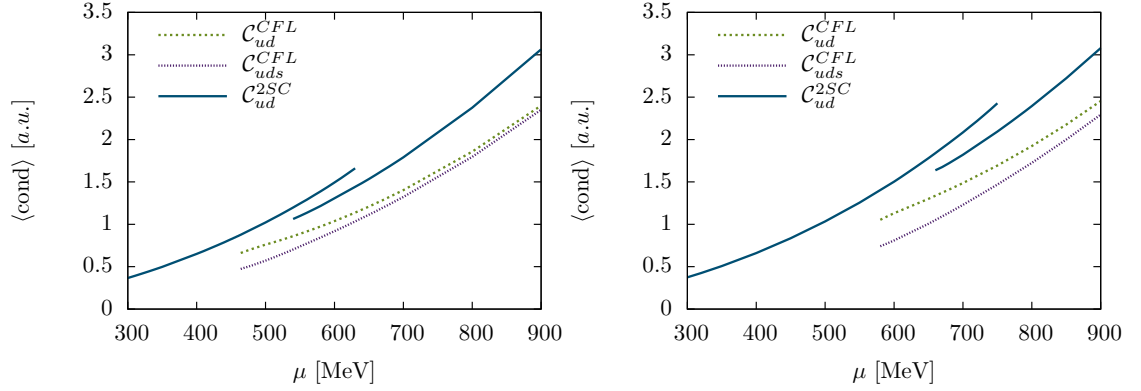


Figure 4.3.: Dependence of 2SC and CFL condensates at $T = 10$ MeV on chemical potential for $m_s = 30$ MeV (left) and $m_s = 54$ MeV (right).

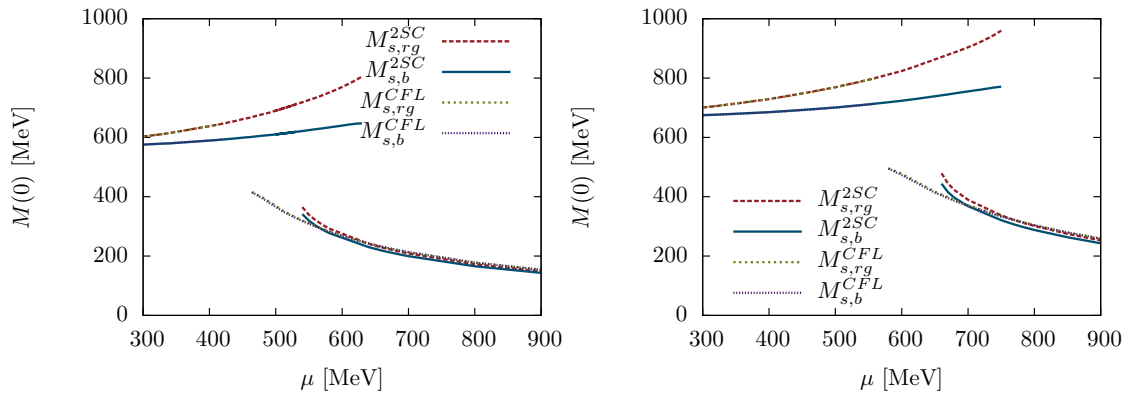


Figure 4.4.: Dependence of the strange-quark mass at $T = 10$ MeV on chemical potential for $m_s = 30$ MeV (left) and $m_s = 54$ MeV (right).

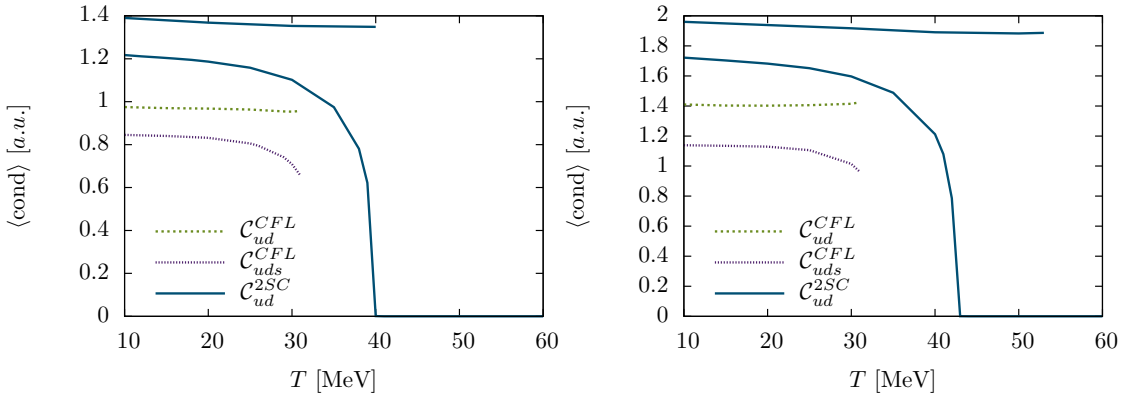


Figure 4.5.: Dependence of 2SC and CFL condensates on temperature at $\mu = 580$ MeV for $m_s = 30$ MeV (left) and at $\mu = 680$ MeV $m_s = 54$ MeV (right).

it is probable, that the CFL phase is favored almost everywhere where it exists and the CFL phase is dominant at $\mu > 500$ MeV or $\mu > 600$ MeV for $m_s = 30$ MeV or $m_s = 54$, respectively. The CFL condensates show no qualitative difference to the HTL-HDL approximation and increase smoothly for chemical potential above the threshold.

The discontinuous behavior in the 2SC phase can be also seen in the diagram for the strange-quark masses Fig. 4.4. We show the mass functions $M(0)$ in the 2SC phase for red/green and blue strange quarks, corresponding to the propagator component proportional to $P_{s,rg}$ and $P_{s,b}$ and the masses in the CFL phase corresponding to P_7 (red/green) and P_3 (blue). The masses in the 2SC phase also have two branches in the first-order region. In contrast to the simpler truncation, the masses of red/green and blue strange quarks have a visible difference in the 2SC phase as the blue quarks are not paired in contrast to the other quarks, which has an influence on their mass. The unpaired blue quarks are lighter than the other quarks.

The CFL pairing shifts the phase transition of the strange quarks to lower chemical potential, as the energy gain due to CFL condensation can exceed the energy gain due to chiral symmetry breaking. The CFL quark masses of blue and red/green quarks do not differ remarkably, as the pairing is almost symmetric. As one would expect, the higher strange-quark mass shifts the strange quark phase transition also to higher chemical potential.

The dependence of the condensates on temperature at a chemical potential of $\mu = 580$ MeV for the light strange-quark mass and of $\mu = 680$ MeV for the heavier ones is shown in Fig. 4.5. These chemical potentials are inside the spinodal region of the strange

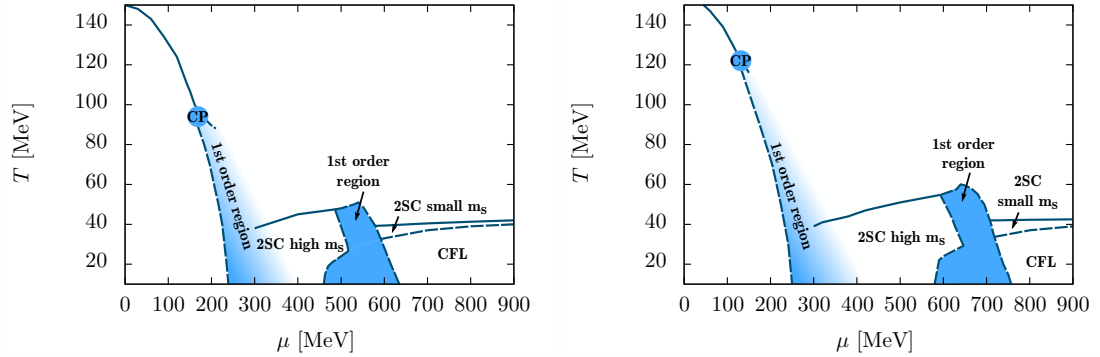


Figure 4.6.: Phase diagram for $m_s = 30$ MeV (left) and $m_s = 54$ MeV (right). First-order areas are indicated by shaded areas bounded by spinodal lines (dashed). Solid lines indicate second-order transitions, CP the tricritical point.

quark phase transition, therefore there are two branches for the 2SC phase. The upper one corresponds to the high strange-quark mass and the lower branch to the light strange quark. The first-order phase transition occurs in the coexistence region of the two branches. Similar to the HTL-HDL case there is a possible CFL pairing at low temperatures followed by a first-order transition to the 2SC phase. The critical temperature of the second-order phase transition between the 2SC and the normal conducting phase is around $T = 40 - 50$ MeV. This is an important difference to the HTL-HDL truncation, which had much smaller critical temperatures.

Due to the impact of the strange quark phase transition, the phase diagrams (Fig. 4.6) show a more complicated phase structure. As a general feature both phase diagrams show larger spinodal regions and a higher critical temperature for the color-superconducting phases in contrast to the HTL-HDL approximation. For the hadronic phase at low densities, the critical point is lifted to higher temperatures and lower chemical potentials. The spinodal region of the first-order transition becomes remarkably larger and we were not able to find the exact position of the upper spinodal anymore. Therefore the region is only approximately indicated. The chiral phase transition seems to be quite robust under the variation of the strange-quark mass, the critical point is shifted to higher temperatures and lower chemical potentials when increasing the strange-quark mass. We find the critical point around $(T, \mu) = (100, 160)$ MeV for $m_s = 30$ MeV and $(T, \mu) = (120, 120)$ MeV for $m_s = 54$ MeV. A similar study in [45] finds a CEP at $T = 100$ MeV and $\mu = 190$ MeV and sees the same qualitative change in comparison with the

HTL-HDL approximation. However, it should be noted that the regularization of the quark loop and the vertex truncation were done in a slightly different way in that work.

Again, our focus lies on the color-superconducting phases at higher chemical potential. The qualitative phase structure with a CFL-like phase at high μ and a 2SC phase at intermediate μ and a small band extending to finite temperature and separating the CFL and normal conducting phase are similar to the HTL-HDL case, nevertheless there are some important differences. The coupling of the strange quarks to the light sector leads to the separation of the 2SC phase in one phase with light, approximately chirally symmetric, strange quarks and a phase with heavy strange quarks, separated by a first-order transition. Therefore, we find a large spinodal region where four phases - the CFL phase, the two 2SC phases and the normal conducting phase - meet and are all separated by first-order transitions. Although we find a (meta-)stable 2SC solution in the shaded region at low temperatures, we expect most of the lower part of the spinodal region to be a CFL-like phase. This would mean that the strange quark transition is shifted to lower chemical potentials in comparison to a 2SC or a normal conducting phase, as the energy gain of CFL pairing is larger than that of strange quark chiral symmetry breaking.

The transition between 2SC and normal conducting phase is, except for the spinodal region, of second-order and for both strange-quark masses between $T = 40 - 60$ MeV. It rises with increasing chemical potential, however, the strange quark phase transition leads to a kink with a sudden drop of the critical temperatures.

Although the strange-quark mass has some influence on the critical point of the chiral phase transition, the color-superconducting section and especially the 2SC phase is quite similar for both masses. The main difference is that the onset of CFL condensation together with the kink in the 2SC transition between light and heavy strange quarks is shifted to larger chemical potentials for the heavier strange quarks. The critical temperature to the normal conducting phase only shows a weak dependence on the strange-quark mass.

4.6. Debye and Meissner masses

The strength of the effective coupling of the quarks is determined by the vertex and the gluon dressing. As the system is dominated by the momentum regime < 1 GeV the screening of the gluons at low energies has a great influence on the system and is interesting to investigate. The screening is in general defined by a screening function $M(k)$ with

$$D \propto \frac{Z_3}{k^2 + M^2(k)} \quad (4.42)$$

and the screening mass is the zero-momentum limit $M(0)$. If $M(0) = 0$ the gluon is not screened and diverges in the IR, for finite $M(0)$ the gluon is finite in the IR. There is a Yang-Mills contribution to the screening mass, given by

$$\begin{aligned} m_{D,YM}^2 &\propto \frac{k^2}{Z_{TL}(k)} \Big|_{k \rightarrow 0} = \Lambda^2 \left(\frac{a_L \Lambda^2}{c} \right)^{b_L} \\ m_{M,YM}^2 &\propto \frac{k^2}{Z_{TT}(k)} \Big|_{k \rightarrow 0} = \Lambda^2 \left(\frac{a_T \Lambda^2}{c} \right)^{b_T} \end{aligned} \quad (4.43)$$

for the gluon parametrization Eq. (3.6). These components are called Debye and Meissner masses and account for the electric and magnetic screening of the gluon. In the Yang-Mills sector both gluon projections are screened and the masses only depend on temperature.

With dynamical quarks in the theory, the quark loop in the gluon polarization gives additional contributions to the gluon masses. These contributions are defined analogously as the polarization tensors at zero momentum

$$\begin{aligned} m_{D,ab}^2 &= \lim_{\vec{p} \rightarrow 0} \Pi_{TL}^{ab}(\omega_m = 0, \vec{p}) \\ m_{M,ab}^2 &= \lim_{\vec{p} \rightarrow 0} \Pi_{TT}^{ab}(\omega_m = 0, \vec{p}). \end{aligned} \quad (4.44)$$

As we focus on the quark sector, we call these quark contributions simply Debye and Meissner masses in the following, neglecting the small and chemical potential independent Yang-Mills contribution (< 0.1 GeV 2). Due to the propagator structure Eq. (4.42), the full screening masses also can only be calculated up to an unknown factor Z_3 in our truncation, leaving them as renormalization dependent result, as we do not calculate Z_3 . However, they are still a qualitative measure for the screening of the gluons.

For normal phases the regularized expressions Eq. (4.19) are

$$\begin{aligned} m_{M,ab}^2 &= 0 \\ m_{D,ab}^2 &= -\frac{Z_{1F} g^2 N_f \delta^{ab}}{2} T \sum_{\omega_n} \int \frac{d^3 q}{(2\pi)^3} \frac{4\Gamma(q, q)}{N_q^2} \left(-2(q_4 + i\mu)^2 C^2(q) + \frac{2}{3} \vec{q}^2 A^2(q) \right). \end{aligned} \quad (4.45)$$

For bare propagators and vertices, which are realized at high temperatures, the Debye mass approaches the HTL-HDL limit Eq. (3.13) $m_D^2 = \frac{N_f g^2}{4\pi} \left(\frac{\pi T^2}{3} + \frac{\mu^2}{\pi} \right)$.

For non-superconducting phases the Meissner masses are equal to 0 as also observed in the HTL-HDL limit Eq. (3.11). For color superconductivity, the $SU_c(3)$ color symmetry

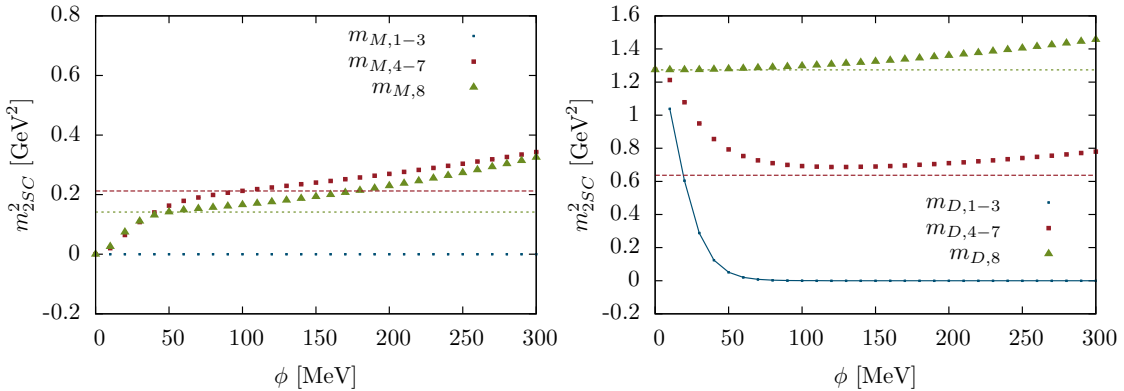


Figure 4.7.: Meissner (left) and Debye (right) masses (dots) of the gluons in different color channels in comparison with weak-coupling results [97] (lines) for the 2SC phase for propagators Eq. (4.31).

is spontaneously broken. The resulting Goldstone bosons are eaten up by the gluons giving rise to magnetic gluon masses via the Anderson-Higgs mechanism [59, 60]. For the 2SC phase the $SU_c(3)$ is broken down to $SU_c(2)$ giving rise to 5 massive gluons while the remaining 3 gluons stay massless. For the CFL phase the whole $SU_c(3)$ group is broken, therefore all 8 gluons acquire Meissner masses.

We show the gluon masses for the simple propagator Eq. (4.31) in Fig. 4.7 at $T = 10$ MeV and $\mu = 1000$ MeV for the 2SC phase with $\phi = \phi_{2SC}$. The 2SC polarization was calculated for $N_f = 2$ flavors. The Debye and Meissner masses for the different gluons are calculated as functions of the gap parameter ϕ and compared with the weak-coupling results of [97]. Additionally to the simple propagator parametrization, the weak-coupling limit assumes $T \ll \phi \ll \mu$. This is fulfilled for ϕ around $100 - 200$ MeV where we find good agreement between the weak-coupling results and our results. For larger and smaller values there are some deviations. For the Debye mass of gluons 1-3 a temperature dependent weak-coupling result is provided that fits exactly our calculation. The Meissner mass of the gluons 1-3 vanishes exactly as they correspond to the $SU_c(2)$ subgroup that stays unbroken in the 2SC phase. Additionally, the Debye mass of gluon 1-3 also tends towards 0 for low temperature. These gluons can only couple to red or green quarks which are all bound in Cooper pairs for 2 flavors. Therefore, the quark loop gives no contribution and no Debye mass is generated. All other gluons acquire both Debye and Meissner masses. The results for a CFL phase for $N_f = 3$ flavors with $\phi = \phi_{oct} = \frac{1}{2}\phi_{sing}$ are shown in Fig. 4.8. As the breaking pattern is symmetric in color

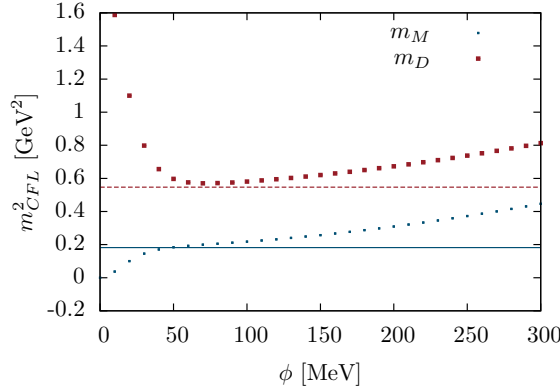


Figure 4.8.: Meissner and Debye masses (dots) in comparison with weak-coupling results [85] (lines) for the CFL phase for propagators Eq. (4.31).

and flavor, all gluons acquire the same Debye and Meissner masses. The weak-coupling results [85] are shown again for comparison and reasonably agree in the region where $T \ll \phi \ll \mu$.

Finally we also show the Debye and Meissner masses for the full calculation for $m_s = 30$ MeV Fig. 4.9 and $m_s = 54$ MeV Fig. 4.10. At low chemical potentials all masses are small as the Debye masses are suppressed by the heavy quark masses and Meissner masses are zero in non-color-superconducting phases. There is a small change at low chemical potential which is a small violation of the Silver-Blaze property, that requires observables and also the Debye mass to be independent on chemical potential, if the latter is smaller than the mass gap of the theory. The violation comes from the vertex approximation and will be discussed in detail in the next section. Small negative squared Debye masses are not forbidden in principle, as there is always a positive Yang-Mills contribution to the Debye mass, that the sum of Yang-Mills and quark contribution still stays positive. However, due to the Silver-Blaze property, the negative contributions should be an artifact, nevertheless.

At $\mu = 300 - 400$ MeV, there is a first phase transition at the onset of 2SC condensation. Similar to the weak-coupling results, gluons 1-3 have no or only small Debye and Meissner masses and the relative ordering of the gluon masses is the same as in the weak-coupling approximation.

At higher chemical potential also the strange quarks undergo a phase transition and become light. Therefore, the strange quark loop gives larger contributions and increases the Debye masses of all gluons equally while it does not contribute to the Meissner

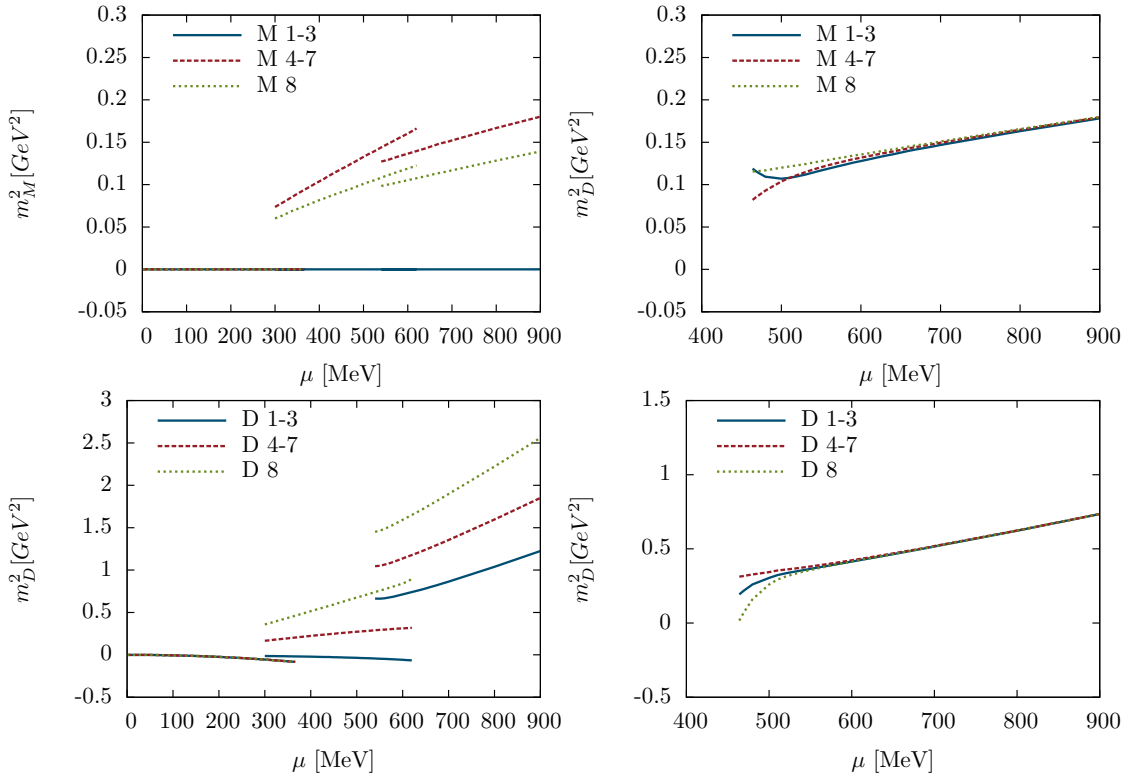


Figure 4.9.: Meissner (top) and Debye (bottom) masses for the 2SC and chirally broken phase (left) and the CFL phase (right) for $m_s = 30$ MeV.

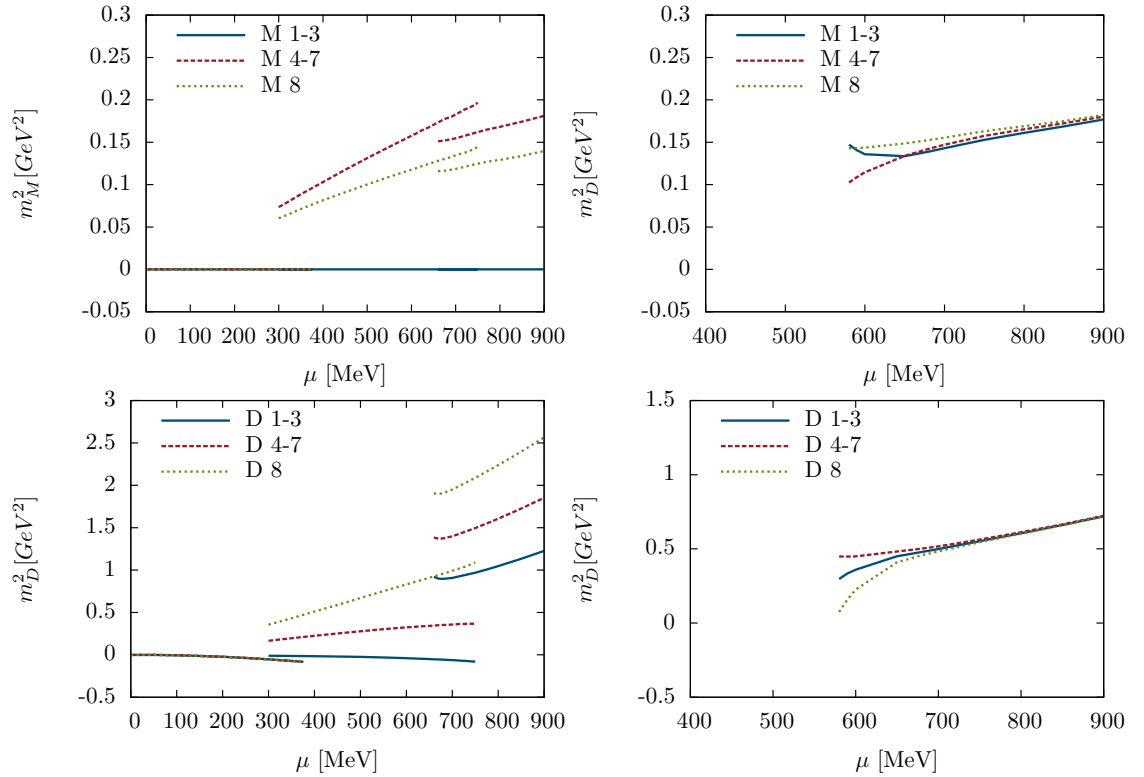


Figure 4.10.: Meissner (top) and Debye (bottom) masses for the 2SC and chirally broken phase (left) and the CFL phase (right) for $m_s = 54$ MeV.

masses. CFL pairing is possible for μ larger than 450 or 550 MeV for $m_s = 30$ or $m_s = 54$ MeV respectively. In this phase, the Debye and Meissner masses of all 8 gluons become similar due to the symmetric pairing pattern, like in the weak-coupling limit. The deviations origin from the finite strange-quark mass and diminish with increasing μ , as the mass becomes negligible with respect to the chemical potential. Both strange-quark masses give very similar results, the main difference is the position of the strange quark phase transition.

4.7. Silver-Blaze property

The Silver-Blaze property [99, 100] states that in a relativistic theory at zero temperature, the partition function and observables do not depend on chemical potential, if the latter stays below the mass gap of the system. Although the Lagrangian of the theory shows an explicit dependence on μ in general and therefore also some unobservable quantities like propagators depend on μ , observables like the masses of physical particles must stay constant, which requires a cancellation of the internal μ -dependence of the Lagrangian. If the chemical potential exceeds the mass gap, states can be excited and observables change. For the baryon Silver-Blaze property, relevant in our study, the Silver-Blaze region is $\mu < m_B/3$ with the proton mass m_B as the mass of the lightest baryon. This Silver-Blaze property only holds at zero temperature, as thermal excitation also change observables. Truncations can easily violate the Silver-Blaze property and our Debye masses Fig. 4.9 and Fig. 4.10 show a small violation of the Silver-Blaze property. In the following we discuss the Silver-Blaze property, its restrictions to the truncation and where we violate it.

For simplicity, we assume a quark propagator with a physical mass Δ that fulfills

$$-C^2(i\Delta, 0)\Delta^2 + B^2(i\Delta, 0) = 0. \quad (4.46)$$

Δ should be also the lowest singularity of the system and therefore the mass gap of the theory. This mass pole lies on the imaginary q_4 -axis. The quark self-energy is schematically given by an integral over a propagator component $S(q_4 + i\mu)$ multiplied with an integration kernel $K(p, q)$ that includes the vertex and the gluon dressings

$$\Sigma(p_4 + i\mu, \vec{p}) \sim \int_{q_4, \vec{q}} S(q_4 + i\mu, \vec{q}) K(p_4 + i\mu, \vec{p}, q_4 + i\mu, \vec{q}). \quad (4.47)$$

We focus on the q_4 integration and consider the integration path C shown in Fig. 4.11. The integral along this contour vanishes as it includes no singularity. Considering a rectangle with infinite extent in $\text{Re}(q_4)$ -direction, that means shifting the vertical parts to

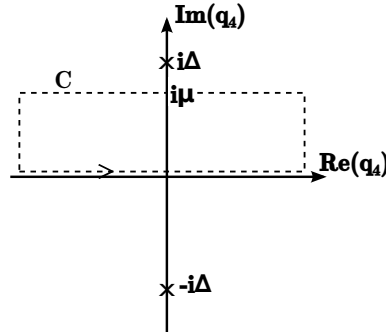


Figure 4.11.: Schematic integration contour of the q_4 -integration in a system with a mass gap Δ .

$q_4 \rightarrow \pm\infty$, these do not contribute as the integrand in Eq. (4.47) vanishes for $q_4 \rightarrow \pm\infty$. Therefore, the integral along the lower horizontal equals the integral along the upper one and especially the shift $q_4 \rightarrow q_4 - i\mu$ in Eq. (4.47) is possible, if the chemical potential is smaller than the mass gap, as no singularity is touched by this shift

$$\Sigma(p_4 + i\mu, \vec{p}) \sim \int_{q_4, \vec{q}} S(q_4, \vec{q}) K(p_4 + i\mu, \vec{p}, q_4, \vec{q}). \quad (4.48)$$

This integral is just the vacuum self-energy evaluated at $p_4 + i\mu$ and therefore

$$\Sigma(p_4 + i\mu, \vec{p}) = \Sigma_{vac}(p_4 + i\mu, \vec{p}). \quad (4.49)$$

For self-energies that are independent on p , like they occur in mean-field calculations in many effective models, the self-energy does not change for chemical potentials lower than the mass gap³. In Dyson-Schwinger calculations the self-energy is momentum dependent and therefore changes with chemical potential, but is related to its vacuum value by Eq. (4.49). Going one step further and calculating the quark condensate we need to evaluate an integral over the quark propagator

$$\langle \bar{q}q \rangle \sim \int_{q_4, \vec{q}} S(q_4 + i\mu, \vec{q}). \quad (4.50)$$

As long as the chemical potential is lower than the mass gap, we can replace the propagator with its vacuum value and shift the integration variable $q_4 \rightarrow q_4 - i\mu$ for the same reasons as before and get

³except if a first-order phase transition occurs earlier

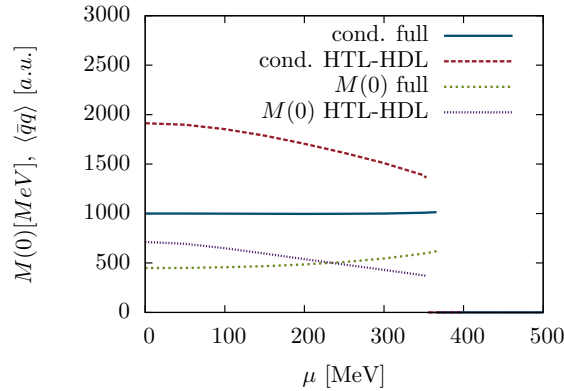


Figure 4.12.: Light quark condensate and mass for HTL-HDL truncation and the full back-coupling.

$$\langle \bar{q}q \rangle \sim \int_{q_4, \vec{q}} S_{vac}(q_4 + i\mu, \vec{q}) = \int_{q_4, \vec{q}} S_{vac}(q_4, \vec{q}) \sim \langle \bar{q}q \rangle_{vac}. \quad (4.51)$$

Therefore, the quark condensate stays constant for $\mu < \Delta$, reflecting the Silver-Blaze property. If $\mu > \Delta$, the shift of the integration variable $q_4 \rightarrow q_4 - i\mu$ is not possible, as the singularity at the mass gap needs to stay outside the integration contour in Fig. 4.11.

We can now study the gluon polarization with similar arguments. It is schematically given by

$$\Pi(k_4, \vec{k}) \sim \int_{q_4, \vec{q}} S(q_4 + i\mu, \vec{q}) S(p_4 + i\mu, \vec{p}) \tilde{K}(p_4 + i\mu, \vec{p}, q_4 + i\mu, \vec{q}) \quad (4.52)$$

with $p = k + q$. Here, the shift $q_4 \rightarrow q_4 - i\mu$ directly leads to a result independent of μ

$$\Pi(k_4, \vec{k}) \sim \int_{q_4, \vec{q}} S(q_4, \vec{q}) S(p_4, \vec{p}) \tilde{K}(p_4, \vec{p}, q_4, \vec{q}) \sim \Pi_{vac}(k_4, \vec{k}). \quad (4.53)$$

In particular the Silver-Blaze property therefore predicts constant Debye and Meissner masses at low chemical potential. In these arguments, it was important to choose a kernel with a consistent dependence on chemical potential $K(p_4 + i\mu, q_4 + i\mu)$.

In the quark DSE we use a vertex $\Gamma(p, q) = \Gamma(p - q)$. The dependence on chemical potential of the argument $p - q$ drops out and the Silver-Blaze property is fulfilled. In our calculation with the improved gluon polarization with full quarks, this vertex spoils renormalizability as shown in Eq. (4.26) and we cannot use it. Instead we take $\Gamma(p, q) =$

$\Gamma(p_4^2 + \vec{p}^2 + q_4^2 + \vec{q}^2)$. This vertex violates the Silver-Blaze property, as a consistent implementation of the chemical potential would require a dependence on $(p_4 + i\mu)^2$ instead of only p_4^2 and analogously for q_4 . On the level of quark quantities, this violation is only weak which can be seen in Fig. 4.12. We show the quark mass function $M(0)$ and quark condensate and also the HTL-HDL results for comparison. The condensate of the full calculation stays almost constant and only shows a tiny increase at higher chemical potential. In contrast, the HTL-HDL result shows a strong dependence on μ which violates the Silver-Blaze property heavily. As the HTL-HDL approximation assumes massless quarks and therefore removes the mass gap, the gluon involves an explicit dependence on chemical potential via the effective gluon mass $m_g^2 \sim \mu^2$ which causes the violation. The quark masses $M(0)$ show a μ -dependence in both cases which gives no statement about the Silver-Blaze property directly, as a momentum dependent self-energy shows a dependence on μ in general according to Eq. (4.49).

For the Debye masses of the improved truncation Fig. 4.9 and Fig. 4.10 the violation of the Silver-Blaze property is a bit larger than on the quark level, but altogether the improved truncation respects the Silver-Blaze property approximately and the violations are negligibly small in the quark sector and not too big in the gluonic sector.

A possible choice for a vertex fulfilling the Silver-Blaze property would be $\Gamma(p, q) = \Gamma((p_4 + i\mu)^2 + \vec{p}^2 + (q_4 + i\mu)^2 + \vec{q}^2)$. We cannot use this vertex as it causes a different problem. When considering the infrared term of our vertex model Eq. (3.2) $\Gamma_{IR}(x) = \frac{d_1}{x+d_2}$, we get for that momentum dependence

$$\Gamma_{IR} = \frac{d_1}{d_2 + (p_4 + i\mu)^2 + \vec{p}^2 + (q_4 + i\mu)^2 + \vec{q}^2}. \quad (4.54)$$

At zero energy and 3-momentum, the denominator becomes $d_2 - 2\mu^2$ which leads to an artificial singularity for larger chemical potential. As this problem cannot be evaded easily, we use the vertex $\Gamma(p, q) = \Gamma(p_4^2 + \vec{p}^2 + q_4^2 + \vec{q}^2)$ and live with a small violation of the Silver-Blaze property.

5. Inhomogeneous phases

In the previous chapters we only considered phases that are homogeneous in space. In effective models it has been found that spatially varying chiral condensates are preferred over homogeneous condensates in the region of the chiral phase transition which is entirely covered by an inhomogeneous phase [35, 101]. In these models, the critical endpoint of QCD changes to a Lifshitz point, where three second-order phase transitions meet in the chiral limit. It turns out that solitonic modulations are the most stable structures among the investigated modulations and 1-dimensional inhomogeneities were preferred over 2-dimensional crystals [102]. In every case, the homogeneous solution was least favored in the vicinity of the first-order line. Also inhomogeneous color-superconducting phases are suggested to be the ground state at higher densities [103–105]

The possibility of an inhomogeneous chiral condensate will be investigated in this section with Dyson-Schwinger equations. In NJL models the central quantity is the thermodynamic potential which is calculated in mean-field approximation and minimized with respect to a parametrized inhomogeneous condensate. As the NJL interaction is local, the thermodynamic potential can be simplified and it is possible to calculate various inhomogeneous structures with a brute-force diagonalization of the Hamiltonian. In the Dyson-Schwinger framework of QCD, the momentum dependent dressing functions increase the numerical effort drastically and we therefore restrict to a simple plane-wave ansatz (chiral density wave) of the modulation which allows an analytical inversion of the quark propagator and keeps the numerical effort on a feasible level. We also perform all calculations in this section with two chiral flavors.

5.1. Quark propagator for inhomogeneous phases

The homogeneous quark propagator is parametrized by

$$S^{-1}(p) = -i\omega_n \gamma_4 C(p) - i\vec{p} A(p) + B(p). \quad (5.1)$$

We now generalize this parametrization to an inhomogeneous propagator. Thereby it is useful to work in the chiral representation of the Dirac matrices (see Appendix A). In this representation γ_5 is diagonal while the other gamma matrices are only non-zero in

the off-diagonal 2×2 blocks. This simplifies the structure of the propagators. Similar to the NJL model we allow an inhomogeneous mass term characterized by an oscillation between scalar and pseudoscalar condensates [33, 34, 106]

$$\begin{aligned}\mathcal{C}_S &= \langle \bar{q}q \rangle \propto \cos(Qz) \\ \mathcal{C}_P &= \langle \bar{q}i\gamma_5\tau_3q \rangle \propto \sin(Qz)\end{aligned}\quad (5.2)$$

with the Pauli matrix τ_3 in isospin space. In general, the pseudoscalar condensate is a vector in that space, however, due to isospin symmetry which is unbroken for vanishing isospin-chemical potential we can rotate it into τ_3 direction.

We parametrize the mass term in coordinate space by

$$\hat{B}(x, y) = B_s(x, y) + i\gamma_5\tau_3B_p(x, y) = \hat{B}^+(x, y) \oplus \hat{B}^-(x, y) \quad (5.3)$$

with the two isospin components

$$\hat{B}^\pm(x, y) = B_s(x, y) \pm i\gamma_5B_p(x, y) \quad (5.4)$$

corresponding to up and down quarks. With the explicit Dirac structure in 2×2 Pauli blocks we get

$$\hat{B}^\pm(x, y) = \begin{pmatrix} B_s(x, y) \mp iB_p(x, y) & 0 \\ 0 & B_s(x, y) \pm iB_p(x, y) \end{pmatrix} \quad (5.5)$$

which visualizes the advantage of the chiral Dirac matrices. The quantities $B_s(x, y)$ and $B_p(x, y)$ are real in coordinate space which originates from the symmetry relations $B_s(p_4) = B_s(-p_4)^*$ and $B_p(p_4) = B_p(-p_4)^*$ in Fourier space (see Eq. (2.103)) and with the definition $B(x, y) := B_s(x, y) + iB_p(x, y)$ we get

$$\hat{B}^+(x, y) = \begin{pmatrix} B^*(x, y) & 0 \\ 0 & B(x, y) \end{pmatrix} = \hat{B}^-(x, y)^*. \quad (5.6)$$

We want to investigate a chiral density wave and make a plane wave ansatz

$$B^+(x, y) = \tilde{B}(x - y) \frac{1}{2} (e^{iQx} + e^{iQy}) \quad (5.7)$$

for the mass term and build a self-consistent system around this ansatz. As our gluon propagator and quark-gluon vertex are diagonal in isospin space, quarks with positive and negative isospin do not mix and we can restrict the calculation to the components with positive isospin $B^+(x, y)$ and omit the isospin indices in the following, unless otherwise noted. $B^-(x, y)$ can be obtained by $Q \rightarrow -Q$.

For 1-dimensional modulations we choose the wave vector Q to point in the 3-direction $Q \equiv Qe_3$. The Fourier transform (see Appendix A.3) of Eq. (5.7) is given by

$$\bar{B}(p, p') = \frac{1}{2} (B(p) + B(p')) \delta(p - p' - Q). \quad (5.8)$$

Eq. (5.8) leads to an off-diagonal structure in p - p' space for the dressing function $\bar{B}(p, p')$. The inversion of a propagator with such a non-diagonal contribution induces further dressing functions and we need in total 10 terms for a complete ansatz for the inverse propagator to achieve a self-consistent solution

$$\begin{aligned} S^{-1}(p, p') = & \left[-i(\omega_n + i\mu)\gamma_4 C(p) - ip_3\gamma_3 E(p) - i\vec{p}_\perp A(p) \right. \\ & \left. - i(\omega_n + i\mu)\gamma_5\gamma_4 C_5(p) - ip_3\gamma_5\gamma_3 E_5(p) - i\gamma_5\vec{p}_\perp A_5(p) \right] \delta(p - p') \\ & + \left(B(p, p') - i\gamma_4\gamma_3 F(p, p') - i\gamma_4 \frac{\vec{p}_\perp}{|\vec{p}_\perp|} G(p, p') - i\gamma_3 \frac{\vec{p}_\perp}{|\vec{p}_\perp|} H(p, p') \right) \frac{(1 - \gamma_5)}{2} \delta(p - p' + Q) \\ & + \left(B(p, p') + i\gamma_4\gamma_3 F(p, p') + i\gamma_4 \frac{\vec{p}_\perp}{|\vec{p}_\perp|} G(p, p') + i\gamma_3 \frac{\vec{p}_\perp}{|\vec{p}_\perp|} H(p, p') \right) \frac{(1 + \gamma_5)}{2} \delta(p - p' - Q) \end{aligned} \quad (5.9)$$

with $B(p, p') = \frac{1}{2} (B(p) + B(p'))$ and similar for F, G and H . Here we used the notation \vec{p}_\perp for the momentum contribution perpendicular to the wave vector Q in 3-dimensional space. The chiral condensates of Eq. (5.2) are then defined by

$$\begin{aligned} \langle \bar{q}q \rangle &= -Z_2 \int_{p, p'} e^{i(p-p')x} \text{Tr} (S^+(p, p') \oplus S^-(p, p')) \\ \langle \bar{q}i\gamma_5\tau_3 q \rangle &= -Z_2 \int_{p, p'} e^{i(p-p')x} \text{Tr} [i\gamma_5\tau_3 (S^+(p, p') \oplus S^-(p, p'))] \end{aligned} \quad (5.10)$$

which have contributions from up and down propagators. The dressing functions are also constrained by symmetries. The relation for negative energies is similar to the homogeneous case Eq. (2.103)

$$S(\omega_n, p_3, \vec{p}_\perp) = \gamma_4 S(-\omega_n, p_3, \vec{p}_\perp)^\dagger \gamma_4, \quad (5.11)$$

while parity is now restricted to the \vec{p}_\perp components, realized by

$$S(\omega_n, p_3, \vec{p}_\perp) = \gamma_5\gamma_2\gamma_5\gamma_1 S(\omega_n, p_3, -\vec{p}_\perp) \gamma_1\gamma_5\gamma_2\gamma_5. \quad (5.12)$$

In the direction of the inhomogeneous modulation, the propagator shows a parity symmetry, if the modulation vector Q is reversed as well

$$S(\omega_n, p_3, \vec{p}_\perp; Q) = \gamma_5 \gamma_3 S(\omega_n, -p_3, \vec{p}_\perp; -Q) \gamma_3 \gamma_5. \quad (5.13)$$

We now specify the structure of the quark propagator for a 1-dimensional modulation. For a periodic modulation we can define a reciprocal lattice (RL) in momentum space and only momenta that differ by an element of the RL are coupled. In our case, the RL is given by the momenta nQ for $n \in \mathbf{Z}$. The Brillouin zone (BZ) is a primitive cell of this lattice such that every momentum is uniquely obtained by $p = K + L$ with $K \in \text{RL}$ and $L \in \text{BZ}$. We can define the (first) Brillouin zone by $[0, Q]$ in 3-direction and infinite in 1- and 2-direction, containing a set of uncoupled momenta. The propagator can be rearranged into a block structure in momentum space by

$$S = \sum_{p \in BZ} S(p) \quad (5.14)$$

where the sum has to be interpreted as a direct sum and $S(p)$ represents one of these blocks which contains the infinite, but discrete, set of momenta differing by an element of the RL which are all coupled in general. To visualize this we show the schematic structure of one of these blocks of the inverse propagator in Dirac and momentum space

$$S^{-1}(p) \sim \left(\begin{array}{c|c|c|c|c|c} \ddots & & & & & \\ \hline 0 & \square_i & \diamondsuit_{i,i+1} & 0 & 0 & 0 \\ \tilde{\square}_i & 0 & 0 & 0 & 0 & 0 \\ \hline 0 & 0 & 0 & \square_{i+1} & \diamondsuit_{i+1,i+2} & 0 \\ 0 & \tilde{\diamondsuit}_{i+1,i} & \tilde{\square}_{i+1} & 0 & 0 & 0 \\ \hline 0 & 0 & 0 & 0 & 0 & \square_{i+2} \\ 0 & 0 & 0 & \tilde{\diamondsuit}_{i+2,i+1} & \tilde{\square}_{i+2} & 0 \\ \hline & & & & & \ddots \end{array} \right). \quad (5.15)$$

The continuous lines visualize the momentum grid and the indices the corresponding momenta $p_i = p + iQ$ which are constrained by the RL. Each field in the momentum grid represents a 4×4 Dirac block, i.e. the four entries of one of these blocks represent a 2×2 matrix each. The squares \square are built out of A, C, E, A_5, C_5 and E_5 dressing functions and only appear in the diagonal momentum space components while the diamonds \diamondsuit represent the non-diagonal B, F, G and H terms. In contrast to different modulations

like sinusoids or solitons, where all of these elements would be coupled, the chiral density wave generates a simpler structure and only four of the 2×2 components are coupled (e.g. \square_i , $\tilde{\square}_{i+1}$, $\diamond_{i,i+1}$ and $\tilde{\diamond}_{i+1,i}$). This allows the propagator to be inverted analytically with the structure

$$S(p) \sim \left(\begin{array}{c|c|c|c|c|c} \ddots & & & & & \\ \hline & 0 & \blacksquare_i & 0 & 0 & 0 & 0 \\ & \tilde{\blacksquare}_i & 0 & 0 & \blacklozenge_{i,i+1} & 0 & 0 \\ \hline & \blacklozenge_{i+1,i} & 0 & 0 & \blacksquare_{i+1} & 0 & 0 \\ & 0 & 0 & \tilde{\blacksquare}_{i+1} & 0 & 0 & \blacklozenge_{i+1,i+2} \\ \hline & 0 & 0 & \blacklozenge_{i+2,i+1} & 0 & 0 & \blacksquare_{i+2} \\ & 0 & 0 & 0 & 0 & \tilde{\blacksquare}_{i+2} & 0 \\ \hline & & & & & & \ddots \end{array} \right). \quad (5.16)$$

Due to the simple structure, the elements of S do not depend on the whole matrix Eq. (5.15) but only on four elements of the latter. For example \blacksquare_i is only dependent on \square_i , $\tilde{\square}_{i+1}$, $\diamond_{i,i+1}$ and $\tilde{\diamond}_{i+1,i}$.

5.2. Gap equations

In a homogeneous system stable states can be determined solely by solving the quark DSE Eq. (2.27) as done before. If we allow inhomogeneous condensates, characterized by a wave vector Q , we need an additional constraint to fix the wave vector and with that the shape of the modulation in coordinate space. The quark DSE can also be derived as the extremum of the thermodynamic potential Ω by variation with respect to the quark propagator

$$\frac{d\Omega}{dS} = 0. \quad (5.17)$$

The ground state of the system is also a minimum of Ω with respect to Q

$$\frac{d\Omega}{dQ} = 0 \quad (5.18)$$

which gives a gap equation that fixes the wave vector Q . Deriving these gap equations is straight forward if the thermodynamic potential is given as an analytic expression. On the other hand, not every DSE allows to reconstruct the thermodynamic potential, especially if the quark-gluon vertex or the gluon propagator depend on quark dressing

functions. For homogeneous phases this is only problematic in the vicinity of a first-order phase transition where more stable and metastable phases coexist and only the thermodynamic potential gives insight which phase is the ground state. In all other regions the DSE is sufficient to find the ground state. For inhomogeneous phases the DSE alone does not fix the wave vector Q . Thus we need a truncation that provides an explicit expression for the thermodynamic potential. Therefore, we use a HTL-HDL truncation for the gluon and a vertex independent of the propagator. Then the effective action which is just the negative thermodynamic potential $\Gamma = -\Omega$, is given by Eq. (2.45)

$$\Gamma = \text{Tr}_P \text{Tr}_{D,c,f} \ln S^{-1} - \text{Tr}_P \text{Tr}_{D,c,f} (\mathbb{1} - Z_2 S_0^{-1} S) + \Gamma_2. \quad (5.19)$$

with the interaction Γ_2 specified later. The traces need to be performed in color, flavor, Dirac and momentum space. For the first term, we can use $\text{Tr} \ln = \ln \det$, but in contrast to the trace, we cannot perform the determinant separately in momentum and Dirac space but have to calculate the determinant for the whole matrix in momentum and Dirac space. However, we can exploit the structure of the propagator and the determinant decays in a product of determinants of blocks Eq. (5.15)

$$\Gamma_0 := \ln \det S^{-1} = T \sum_{\omega_n} \ln \prod_{\vec{p} \in BZ} \det S^{-1}(p). \quad (5.20)$$

The product can be written as an integral over the BZ

$$\Gamma_0 = T \sum_{\omega_n} \int \frac{d^2 p_\perp}{(2\pi)^2} \int_0^Q \frac{dp_3}{2\pi} \ln \det S^{-1}(p). \quad (5.21)$$

The momentum determinant is now restricted to one block $S^{-1}(p)$. Additionally we can use that these blocks Eq. (5.15) consist of smaller blocks that decouple and restrict the propagator to one of these smaller blocks, summing over all contributions

$$\Gamma_0 = T \sum_{\omega_n} \int \frac{d^2 p_\perp}{(2\pi)^2} \sum_m \int_0^Q \frac{dp_3}{2\pi} \ln \det S_{\square}^{-1}(p_m = p + mQ) \quad (5.22)$$

where $S_{\square}^{-1}(p_m)$ is one of the smaller coupled blocks in Eq. (5.15) that depends on p_m and $p_m + Q$. Finally we can combine the integration over the BZ and the sum over the blocks

$$\sum_m \int_0^Q \frac{dp_3}{2\pi} f(p_3 + mQ) = \int \frac{dp_3}{2\pi} f(p_3) \quad (5.23)$$

and write

$$\Gamma_0 = T \sum_{\omega_n} \int \frac{d^2 p_\perp}{(2\pi)^2} \int \frac{dp_3}{2\pi} \ln \det S_\square^{-1}(p) \equiv \int_p \text{Tr} \ln S_\square^{-1}(p) \quad (5.24)$$

with the small block $S_\square^{-1}(p)$. The second contribution to Γ contains a matrix product with the homogeneous bare propagator being diagonal in momentum space

$$S_0^{-1}(p, p') = (2\pi)^4 \delta(p - p') S_0^{-1}(p). \quad (5.25)$$

As the trace can be performed separately in momentum and Dirac space, we only modify the momentum trace and write it as sum over matrix elements

$$\Gamma_1 := - \sum_{p, p'} \text{Tr}_{D, c, f} \left((2\pi)^4 \delta(p - p') - Z_2 S_0^{-1}(p, p') S(p', p) \right). \quad (5.26)$$

This sum covers infinitely many momenta which are also infinitely dense and can be replaced by an integral

$$\Gamma_1 = - \int_{p, p'} \text{Tr}_{D, c, f} \left((2\pi)^4 \delta(p - p') - Z_2 S_0^{-1}(p, p') S(p', p) \right). \quad (5.27)$$

Using the bare propagator Eq. (5.25), one momentum integral can be evaluated

$$\Gamma_1 = - \int_p \text{Tr}_{D, c, f} \left(\mathbb{1} - Z_2 S_0^{-1}(p) S(p, p) \right). \quad (5.28)$$

Similar to Γ_0 , we can write this expression as a function of $S_\square(p)$, which is useful for deriving the gap equations

$$\Gamma_1 = - \int_p \text{Tr} \left(\mathbb{1} - Z_2 S_{0, \square}^{-1}(p) S_\square(p) \right). \quad (5.29)$$

The interaction term is shown in Fig. 5.1 and given by

$$\Gamma_2 = Z_{1F} \frac{g^2}{2} \int_{p, p', q, q'} \text{Tr}_{D, c, f} \left(\gamma_\mu \frac{\lambda^a}{2} S(q, q') \Gamma_\nu^b(q', p') D_{\mu\nu}^{ab}(k, k') S(p', p) \right) \quad (5.30)$$

where we assumed a homogeneous vertex (see Appendix Eq. (B.16)). In the following we also consider a homogeneous gluon

$$D_{\mu\nu}^{ab}(k, k') = (2\pi)^4 \delta(k - k') D_{\mu\nu}^{ab}(k) \quad (5.31)$$

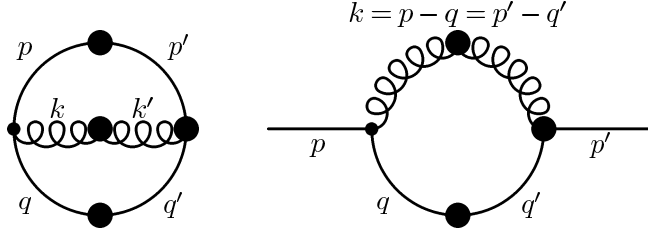


Figure 5.1.: Feynman diagrams for the interaction term of the effective action Γ_2 (left) and the corresponding self-energy (right). Plain lines represent quark propagators, the curly line the gluon propagator. Thick dots represent dressed quantities. The gluon momenta are defined by $k = p - q$ and $k' = p' - q'$ and for a homogeneous gluon holds $k = k'$.

and a vertex dependent on the gluon momentum $\Gamma_\nu^b(q', p') = \Gamma_\nu^b(k')$. In general, especially when considering the full back-coupling of the quark to the gluon or vertex, the latter are also expected to have an inhomogeneous structure, which we neglect for simplicity. Using our previous notation, Γ_2 can also be written more compactly

$$\Gamma_2 = Z_{1F} \frac{g^2}{2} \int_{p,q} \text{Tr} \left(\gamma_\mu \frac{\lambda^a}{2} S_\square(q) \Gamma_\nu^b(k) D_{\mu\nu}^{ab}(k) S_\square(p) \right). \quad (5.32)$$

One of the gap equations is the standard DSE obtained by extremizing Γ with respect to the dressed propagator

$$\frac{\delta \Gamma}{\delta S} = 0 \quad (5.33)$$

and leads to the quark DSE

$$S^{-1}(p, p') = Z_2 S_0^{-1}(p, p') + g^2 \int_{q, q'} \Gamma_{\mu, 0}^a S(q, q') D_{\mu\nu}^{ab}(k, k') \Gamma_\nu^b(q', p'). \quad (5.34)$$

Due to the assumption of a homogeneous gluon and vertex, the inhomogeneous structure is solely carried by the quarks and the loop integral only depends on q , while the q' integration is trivial with the momentum conservation of the gluon propagator $\delta(k - k')$. When using the block structure we can derive a more compact expression for the DSE

$$S_\square^{-1}(p) = Z_2 S_{0, \square}^{-1}(p) + g^2 \int_q \Gamma_{\mu, 0}^a S_\square(q) D_{\mu\nu}^{ab}(k) \Gamma_\nu^b(k). \quad (5.35)$$

The second gap equation is obtained by varying the action with respect to Q

$$\frac{d\Gamma}{dQ} \stackrel{!}{=} 0. \quad (5.36)$$

When calculating this derivative it is useful to take the description of the action in terms of the small blocks (Eq. (5.24), Eq. (5.29), Eq. (5.32)). As the small blocks depend on p and $p + Q$, we need to consider that the argument of S_0^{-1} also depends on Q and needs to be varied when calculating the second gap equation

$$0 \stackrel{!}{=} \frac{d\Gamma}{dQ} = \int_p \text{Tr} \frac{\delta\Gamma}{\delta S_{\square}(p)} \frac{dS_{\square}(p)}{dQ} + \int_p \text{Tr} \frac{\delta\Gamma}{\delta S_{0,\square}^{-1}(p)} \frac{dS_{0,\square}^{-1}(p)}{dQ}. \quad (5.37)$$

The first term is just the first gap equation (quark DSE) and vanishes at the extremum. The derivative in the second term can be carried out and we obtain

$$0 \stackrel{!}{=} \int_p \text{Tr} \left(S_{\square}(p) \frac{dS_{0,\square}^{-1}(p)}{dQ} \right). \quad (5.38)$$

The derivative of the bare propagator can be evaluated

$$\frac{d}{dQ} S_{0,\square}^{-1}(p) = \frac{d}{dQ} \begin{pmatrix} -i(\omega_n + i\mu) - \vec{\sigma}\vec{p} & 0 \\ 0 & -i(\omega_n + i\mu) + \vec{\sigma}(\vec{p} + Q) \end{pmatrix} = \begin{pmatrix} 0 & 0 \\ 0 & \sigma_3 \end{pmatrix}. \quad (5.39)$$

In analogy to the dressing functions of the inverse propagator Eq. (5.9), we label the dressing functions of the dressed propagator that are proportional to $-ip_3\gamma_3$ and $-ip_3\gamma_5\gamma_3$ by $e(p)$ and $e_5(p)$, respectively. We then get from Eq. (5.38)

$$0 \stackrel{!}{=} \int_p (p_3 + Q)e_5(p + Q) - (p_3 + Q)e(p + Q). \quad (5.40)$$

Shifting the integration variable $p \rightarrow p - Q$ and using the symmetry $e(p_3) = e(-p_3)$ the gap equation simplifies to

$$\int_p p_3 e_5(p) \stackrel{!}{=} 0. \quad (5.41)$$

This expression does not vanish in general, as $e_5(p_3) = -e_5(-p_3)$. It gives the necessary condition for the determination of Q .

5.3. Results

For the numerical calculation we use the ansatz Eq. (5.9) for the inverse propagator and the corresponding self-energy. We first fix the wave vector Q and solve the gap equation for the propagator Eq. (5.34) for fixed Q . The inversion of the propagator can

5. Inhomogeneous phases

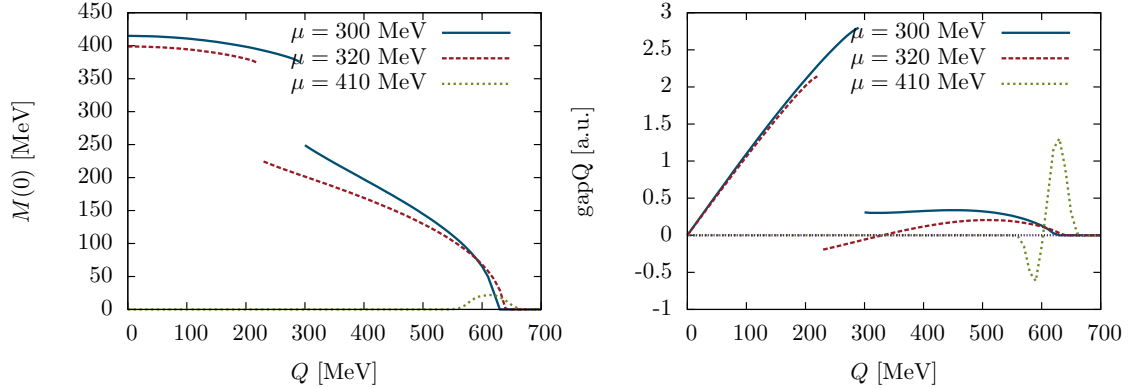


Figure 5.2.: Mass (left) and left-hand side of the gap equation for Q (right) in dependence of a fixed value of Q at $T = 10$ MeV for different chemical potentials.

be performed analytically with computer algebra systems, taking advantage of the block structure in momentum space. Then, we have to solve the coupled system

$$S^{-1}(p, p') = Z_2 (S_0^{-1}(p, p') + \Sigma(p, p')) \quad (5.42)$$

$$\Sigma(p, p') = -4\pi\alpha(\nu)T \sum_{\omega_n} \int \frac{d^3 q}{(2\pi)^3} \frac{\Gamma(k)}{\tilde{Z}_3} \gamma_\mu \frac{\lambda_a}{2} S(q, q + p' - p) \gamma_\nu \frac{\lambda_b}{2} D_{\mu\nu}^{ab}(k) \quad (5.43)$$

with the self-energy truncation of Eq. (3.3).

We perform these steps for several values of Q and evaluate the left-hand side of the gap equation for Q Eq. (5.41) for these results. A necessary condition for a stable solution is this expression to be zero while the slope of the curve at this point has to be positive. This allows us to find possible inhomogeneous solutions of the Dyson-Schwinger system.

We first show a visualization of the root-finding procedure of the Q -gap equation in Fig. 5.2. In the left picture the result for the mass $M(0) = \left| \frac{B(0)}{C(0)} \right|$ as an outcome of the quark DSE, iterated with a fixed value of Q , is shown in dependence of Q . All results are at $T = 10$ MeV. The right plot shows the result of the left-hand side of the Q -gap equation Eq. (5.36) evaluated with the self-consistent solution of the quark DSE. At a chemical potential of 300 MeV the mass decreases smoothly till a sudden jump at $Q \approx 300$ MeV. After this discontinuity the mass again smoothly decreases to zero. The value of the Q -gap equation rises almost linearly and also jumps to a much smaller value at the discontinuity at $Q \approx 300$ MeV. Afterwards it rises weakly again and finally also decreases to 0. At this chemical potential there is only one stable solution at $Q = 0$

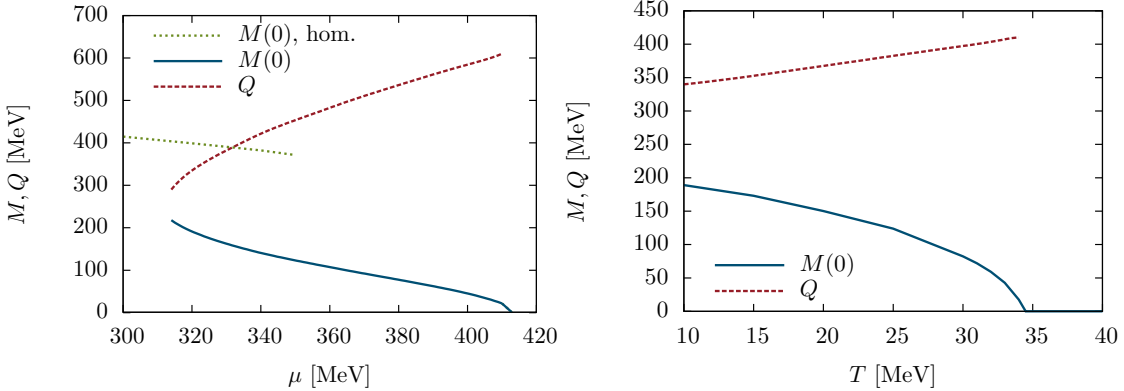


Figure 5.3.: Mass and wave vector Q of the stable solutions in dependence of μ at $T = 10$ MeV (left) and of T at $\mu = 320$ MeV (right).

with a positive slope. The region at $Q > 630$ MeV where the gap equation also vanishes is a plateau in the thermodynamic potential and corresponds to the unstable massless solution. At $\mu = 320$ MeV the mass has a similar shape as for $\mu = 300$ MeV while the Q -gap equation even drops below zero at the discontinuity. This implies a second root of the gap equation with a positive slope at $Q \approx 335$ MeV which corresponds to a stable or metastable inhomogeneous solution. At higher chemical potentials we enter a region where no massive homogeneous solution exists, however, an inhomogeneous solution may be possible. This is the case for $\mu = 410$ MeV where only at finite Q around 600 MeV the mass is non-zero. As the Q -gap equation also shows a zero in this region, which is the only solution with positive slope, the inhomogeneous solution is the ground state in this region.

The masses and wave vectors of the inhomogeneous solutions are shown in Fig. 5.3. The left picture shows the dependence on chemical potential at $T = 10$ MeV. Additionally the massive homogeneous is shown. The decrease of the homogeneous solution with increasing chemical potential is mainly attributed to a violation of the Silver-Blaze property (see Sec. 4.7) due to the HTL-HDL approximation. At chemical potentials larger than 315 MeV we find an inhomogeneous solution which is separated from the homogeneous phase by a first-order phase transition. At this transition the mass jumps to a smaller value while a finite wave vector Q arises. As we do not calculate the pressure, we cannot determine the exact position of the phase transition, instead the onset of the inhomogeneous solution indicates the lower spinodal of the phase transition. In the inhomogeneous region the mass smoothly decreases to zero while Q rises. At $\mu > 410$ MeV

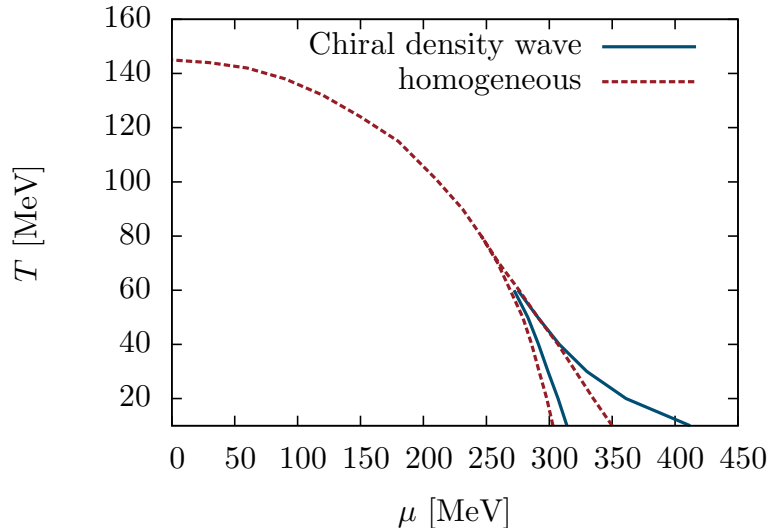


Figure 5.4.: Phase diagram for inhomogeneous phases. The red line shows the homogeneous phase diagram including the spinodals. The blue line shows the boundaries of the inhomogeneous region.

the mass is zero and the system becomes independent of Q . The transition between inhomogeneous and chirally restored phase is of second-order. The right plot shows the same quantities at $\mu = 320$ MeV in dependence on temperature. At this chemical potential the system is inhomogeneous at low temperatures, indicated by a finite Q . With increasing temperature the mass continuously melts to zero, also in a second-order transition, while Q rises with temperature.

We can also collect all results and draw a phase diagram, displayed in Fig. 5.4. It shows the inhomogeneous region and the homogeneous transition with the two spinodals that restrict the region of the first-order phase transition. The upper border of the inhomogeneous phase is a second-order transition and lies outside the homogeneous spinodal region. This line also bends to higher chemical potentials for lower temperatures and it is unclear if the inhomogeneous region ends or if the transition line only approaches 0 asymptotically. The lower border is a first-order spinodal that gives a lower bound to the inhomogeneous phase. Although we do not know the exact positions of the first-order transitions, we can state that the inhomogeneous region covers the homogeneous first-order phase transition similar to results in the NJL model [35, 101]. Especially the phase diagram in [35] which also includes the homogeneous spinodals looks qualitatively

very similar to our result.

The positions of the homogeneous critical point and the critical point, where the inhomogeneous region and the second-order chiral phase transition meet, seem to be very similar. Unfortunately our numerical precision does not allow to decide if these two points coincide or not. In NJL models without vector coupling, these two points fall on top of each other and the resulting phase diagram [35] is in qualitative agreement with our result.

6. Conclusion and Outlook

In this work we investigated QCD at finite density with Dyson-Schwinger equations. These equations are the exact QCD equations of motion but, as they are not a closed system of equations, cannot be solved exactly and need to be truncated. We focused on the quark sector and studied the truncated quark DSE and the quark contribution to the gluon DSE in detail. For the Yang-Mills sector of the gluon DSE we used dressing functions obtained in lattice QCD calculations and for the quark gluon vertex dressing we used a phenomenological model with correct UV running and a model IR strength.

In a first step we calculated the quark loop in the gluon DSE with a hard-thermal-loop / hard-dense-loop approximation which assumes bare massless propagators and provides analytic expressions for the gluon polarization. Open parameters in the vertex were fitted to reproduce the critical temperature of the chiral phase transition at 150 MeV. We performed calculations for 2+1 flavors with 2 chiral quarks and a strange quark with masses in a range compatible with the data of the particle data group [93]. We investigated a 2SC and a CFL like phase and calculated the phase diagram. We see a first-order region with a critical endpoint for the chiral phase transition. At high densities the CFL phase is the ground state as expected. At intermediate densities and in a band between the CFL and the chirally restored phase at finite temperature we also find a 2SC phase. The critical temperature of the color-superconducting phases is quite low and around 20 – 30 MeV.

We improved the truncation in a second step by evaluating the quark loop with dressed color-superconducting quark propagator and therefore used a truncation which is self-consistent on the level of quarks. However, we still neglected the effects of the quark propagator on the Yang-Mills sector. The evaluation of the quark loop required the development of a regularization scheme to cure the quadratic divergencies occurring in a calculation with a numerical cutoff. We used a regularization that effectively subtracted the longitudinal contributions to remove the divergencies. We also had to improve the vertex structure by adding contributions of the color-superconducting condensates to the vertex guided by Slavnov-Taylor identities of QCD. We solved the coupled system of quark and gluon DSE and calculated condensates and the phase diagram. In comparison with the HTL-HDL approximation, the critical temperatures turned out to be higher and are between 40 and 60 MeV. Additionally also the strange quark phase transition is

6. Conclusion and Outlook

clearly visible in the color-superconducting phases, as the strange quark also couples to the light quark via the gluon. It splits the 2SC phase into two phases with high and low strange-quark mass. This truncation also improves vacuum observables like the pion decay constant which was overestimated in the HTL-HDL approximation. With this truncation we also could calculate Debye and Meissner masses of the gluon. Due to the breaking of the color symmetry, gluons with different colors acquire different dressing functions. We checked our truncation by using weak-coupling quark propagators and we could reproduce the weak-coupling results for the Debye and Meissner masses [85, 97]. For the full calculation the gluon masses showed the same relative behavior as in the weak-coupling case. Our truncation does not fulfill the Silver-Blaze property completely as we made simplifying assumptions in the vertex model, but the deviations from the Silver-Blaze property are under control and only small. Especially the quark condensate shows no visible deviation.

In the second part we investigated spatially inhomogeneous phases in the Dyson-Schwinger formalism. These phases have already been investigated in effective models and turned out to cover the first-order chiral phase transition [35]. We developed the formalism to implement inhomogeneous condensates in the Dyson-Schwinger system and to solve the system iteratively as it is commonly done with DSEs. We used the most simple inhomogeneous modulation in form of a one-dimensional plane wave and solved the Dyson-Schwinger system for 2 chiral flavors in HTL-HDL approximation. The gap equations for the quark propagator and the wave vector, characterizing the inhomogeneous modulation, have been obtained by the stationarity condition of the thermodynamic potential. Similar to model calculations, we find an inhomogeneous phase that covers the original first-order transition completely. The critical point seems to stay at the same position within the numerical accuracy. The homogeneous chirally broken phase undergoes a first-order phase transition to an inhomogeneous chirally broken phase. The transition to the normal phase seems to be of second-order within our accuracy.

For the future, it would still be desirable to extend these calculations in further studies. There are still strong assumptions in the truncation especially in the vertex. Therefore, the investigation of the vertex DSE in a suitable truncation and investigating a closed system for quark and gluon propagator and quark-gluon vertex would be a great improvement of the truncation, however, it is numerically demanding. It is also possible to include meson and baryon contributions to the vertex which should be dominant dynamical contributions.

The study of inhomogeneous phases was only a small step into this field. While more complicated inhomogeneous structures like solitons or more-dimensional modulations seem to be numerically tough with DSEs, the investigation of color-superconducting phases with a plane wave structure should be a doable task. These steps, together with

model investigations and experimental research are crucial steps for the understanding of QCD at finite density.

A. Definitions

A.1. Conventions

Throughout this work, we use natural units $\hbar = c = k_B = 1$. We work in 4-dimensional space using the Euclidean metric $g_{\mu\nu} = \delta_{\mu\nu}$ and scalar products of 4-vectors are defined by $xy = x_\mu y_\mu = x_4 y_4 + \vec{x}\vec{y}$.

A.2. Dirac matrices

The Dirac matrices are a matrix representation of the Clifford algebra

$$\{\gamma_\mu, \gamma_\nu\} = 2\delta_{\mu\nu}. \quad (\text{A.1})$$

The most common representation is the Dirac representation, given by

$$\gamma_4 = \begin{pmatrix} 1 & 0 \\ 0 & -1 \end{pmatrix}, \quad \gamma_i = \begin{pmatrix} 0 & -i\sigma_i \\ i\sigma_i & 0 \end{pmatrix} \quad (\text{A.2})$$

with the Pauli matrices

$$\sigma_1 = \begin{pmatrix} 0 & 1 \\ 1 & 0 \end{pmatrix}, \quad \sigma_2 = \begin{pmatrix} 0 & -i \\ i & 0 \end{pmatrix}, \quad \sigma_3 = \begin{pmatrix} 1 & 0 \\ 0 & -1 \end{pmatrix}. \quad (\text{A.3})$$

These matrices are Hermitian $\gamma_\mu^\dagger = \gamma_\mu$. Additionally the 5th Dirac matrix is defined by

$$\gamma_5 = -\gamma_1\gamma_2\gamma_3\gamma_4 = \begin{pmatrix} 0 & 1 \\ 1 & 0 \end{pmatrix} \quad (\text{A.4})$$

and anti-commutes with γ_μ .

For inhomogeneous phases it is convenient to choose the chiral representation of the Dirac matrices

$$\gamma_4^\chi = \begin{pmatrix} 0 & 1 \\ 1 & 0 \end{pmatrix}, \quad \gamma_i^\chi = \gamma_i^D. \quad (\text{A.5})$$

This effectively swaps γ_4 and γ_5

$$\gamma_4^\chi = \gamma_5^D, \quad \gamma_5^\chi = -\gamma_4^D. \quad (\text{A.6})$$

A.3. Fourier transformation

We define the Fourier transform as

$$\begin{aligned} F(p) &= \int d^4x e^{-ipx} F(x) \\ F(p, q) &= \int d^4x d^4y e^{-i(px-qy)} F(x, y) \end{aligned} \quad (\text{A.7})$$

and the inverse transform as

$$\begin{aligned} F(x) &= \int \frac{d^4p}{(2\pi)^4} e^{ipx} F(p) \\ F(x, y) &= \int \frac{d^4p}{(2\pi)^4} \frac{d^4q}{(2\pi)^4} e^{i(px-qy)} F(p, q). \end{aligned} \quad (\text{A.8})$$

A.4. Integral conventions

The integrals in 4-dimensional Fourier space can be simplified exploiting symmetries. For vacuum integrals, we use hyperspherical coordinates

$$\int \frac{d^4q}{(2\pi)^4} = \frac{1}{(2\pi)^4} \int_0^\Lambda dq q^3 \int_0^{2\pi} d\varphi \int_0^\pi d\theta \sin \theta \int_0^\pi d\psi \sin^2 \psi \quad (\text{A.9})$$

with a cut-off Λ . ψ is the angle between q and an external momentum p , $pq = |p||q| \cos \psi$, and the remaining angular integrals are trivial. In medium, the $O(4)$ symmetry is broken to $O(3)$ and $q_4 = |q| \cos \psi$ and $|\vec{q}| = |q| \sin \psi$ are independent coordinates. Finite temperature additionally introduces discrete values of q_4 and replaces the q_4 -integration by a Matsubara sum and we cannot use 4-dimensional hyperspherical coordinates anymore. Using 3-dimensional spherical coordinates for the $O(3)$ -symmetric space instead, we can parametrize the integral by

$$\int \frac{d^4q}{(2\pi)^4} \rightarrow T \sum_{\omega_n} \int \frac{d^3q}{(2\pi)^3} = \frac{T}{(2\pi)^3} \sum_{\omega_n} \int_0^\Lambda d|\vec{q}| |\vec{q}|^2 \int_0^{2\pi} d\varphi \int_0^\pi d\theta \sin \theta \quad (\text{A.10})$$

with the angle θ between \vec{q} and an external momentum \vec{p} , $\vec{p}\vec{q} = |\vec{p}||\vec{q}| \cos \theta$, and a trivial φ integration.

For inhomogeneous phases we introduced a wave vector $\vec{Q} = Q\vec{e}_3$ in p_3 -direction and the spatial $O(3)$ symmetry is broken to an $O(2)$ symmetry in the \vec{p}_\perp -plane. In the parametrization Eq. (A.10), these components are defined by $p_3 = |\vec{p}| \cos \theta$ and

A. Definitions

$|\vec{p}|_\perp = |\vec{p}| \sin \theta$ together with the scalar product $\vec{p}_\perp \cdot \vec{q}_\perp = |\vec{p}|_\perp |\vec{q}|_\perp \cos \varphi$ and all integrations are non-trivial in general.

In some parts, we abbreviate the integrals by \int_q which is short for the integral Eq. (A.9) or Eq. (A.10), dependent on if it is a vacuum or a medium expression, respectively. Dirac delta functions are denoted as $\delta(p - q)$, at finite temperature with $p_4 = (2n + 1)\pi T$ and $q_4 = (2n' + 1)\pi T$ they are given in detail by

$$\delta(p - q) = \delta(p_4 - q_4) \delta(\vec{p} - \vec{q}) \equiv \frac{1}{2\pi T} \delta_{n,n'} \delta(\vec{p} - \vec{q}), \quad (\text{A.11})$$

so that

$$(2\pi)^4 \int_q \delta(p - q) = (2\pi)^4 T \sum_{\omega_n} \int \frac{d^3 q}{(2\pi)^3} \frac{1}{2\pi T} \delta_{n,n'} \delta(\vec{p} - \vec{q}) = 1. \quad (\text{A.12})$$

B. Correlation functions

Abbreviating the QCD fields $(\bar{\psi}, \psi, A_\mu^a, \bar{c}^a, c^a)$ with φ_i and the corresponding sources with J_i , the generating functional is given by

$$Z[J] = \int \mathcal{D}\varphi \exp(-S[\varphi] + J_i \varphi_i) \quad (\text{B.1})$$

where the source terms are

$$J_i \varphi_i = \bar{\eta}\psi + \bar{\psi}\eta + j_\mu^a A_\mu^a + \bar{\sigma}^a c^a + \bar{c}^a \sigma^a. \quad (\text{B.2})$$

The generating functional of connected Green's functions is defined by

$$W[J] = \ln Z[J]. \quad (\text{B.3})$$

The macroscopic fields ϕ_i are defined as expectation values of the fields φ_i and given by

$$\phi_i = \pm \frac{\delta W[J]}{\delta J_i} \quad (\text{B.4})$$

where the upper signs stands for the cases $J_i \in \{j_\mu^a, \bar{\eta}, \bar{\sigma}^a\}$ and the lower signs for the cases $J_i \in \{\eta, \sigma^a\}$ which involve a minus sign due to the anti-commutative character of the Grassmann numbers. The effective action is then the Legendre transform of $W[J]$

$$\Gamma[\phi] = \int_z J_i(z) \phi_i(z) - W[J] \quad (\text{B.5})$$

and therefore the sources are given by

$$J_i = \pm \frac{\delta \Gamma[\phi]}{\delta \phi_i}. \quad (\text{B.6})$$

The propagators are defined as 2-point correlation functions

$$\langle \mathcal{T} \varphi_j(y) \varphi_i(x) \rangle = \left. \frac{\delta^2 W}{\delta J_j(y) \delta J_i(x)} \right|_{J=0} \quad (\text{B.7})$$

B. Correlation functions

and can be expressed as derivatives of $W[J]$ or $\Gamma[\phi]$

$$S_{\alpha\beta}(x, y) = \left. \frac{\delta^2 W}{\delta \eta_\beta(y) \delta \bar{\eta}_\alpha(x)} \right|_{J=0} = \left(\frac{\delta^2 \Gamma}{\delta \psi_\beta(y) \delta \bar{\psi}_\alpha(x)} \right)^{-1} \quad (\text{B.8})$$

$$D_{\mu\nu}^{ab}(x, y) = \left. \frac{\delta^2 W}{\delta j_\nu^b(y) \delta j_\mu^a(x)} \right|_{J=0} = \left(\frac{\delta^2 \Gamma}{\delta A_\nu^b(y) \delta A_\mu^a(x)} \right)^{-1} \quad (\text{B.9})$$

$$G^{ab}(x, y) = \left. \frac{\delta^2 W}{\delta \sigma^b(y) \delta \bar{\sigma}^a(x)} \right|_{J=0} = \left(\frac{\delta^2 \Gamma}{\delta c^b(y) \delta \bar{c}^a(x)} \right)^{-1} \quad (\text{B.10})$$

where α and β indicate the components of the quark spinors (color, flavor, Dirac) and emphasize, that the quark propagator is a matrix in these spaces and not a contracted object as $\frac{\delta^2 W}{\delta \eta(y) \delta \bar{\eta}(x)}$ would suggest. The bare propagators are obtained from the classical action for vanishing field expectation values

$$S_{0,\alpha\beta}^{-1}(x, y) = \frac{\delta^2 S}{\delta \psi_\beta(y) \delta \bar{\psi}_\alpha(x)} = (-\not{d} + m)_{\alpha\beta} \delta(x - y) \quad (\text{B.11})$$

$$D_{\mu\nu,0}^{-1,ab}(x, y) = \frac{\delta^2 S}{\delta A_\nu^b(y) \delta A_\mu^a(x)} = \delta^{ab} \left(-\partial^2 \delta_{\mu\nu} + \left(1 - \frac{1}{\xi} \right) \partial_\mu \partial_\nu \right) \delta(x - y) \quad (\text{B.12})$$

$$G_0^{-1,ab}(x, y) = \frac{\delta^2 S}{\delta c_b(y) \delta \bar{c}_a(x)} = \delta^{ab} \partial^2 \delta(x - y). \quad (\text{B.13})$$

The dressed vertices are the higher derivatives of the effective action, e.g. the quark-gluon vertex is defined by

$$g\Gamma_{\mu,\alpha\beta}^a(x, y, z) = \frac{\delta^3 \Gamma}{\delta A_\mu^a(x) \delta \psi_\beta(y) \delta \bar{\psi}_\alpha(z)} \quad (\text{B.14})$$

and analogously for other vertices. The relation to the connected 3-point function can also be established by taking an additional derivative $\frac{\delta}{\delta j_\nu^b}$ of Eq. (B.8)

$$\left. \frac{\delta^3 W}{\delta j_\nu^b(x) \delta \eta_\beta(y) \delta \bar{\eta}_\alpha(z)} \right|_{J=0} = - \int_{u,v,w} D_{\mu\nu}^{ab}(x, u) S_{\alpha\gamma}(z, v) g\Gamma_{\nu,\gamma\delta}^b(u, v, w) S_{\delta\beta}(w, y). \quad (\text{B.15})$$

For the Fourier transformed vertex $\Gamma_\mu^a(k, p, q)$ with incoming quark (p) and gluon (k) momentum and outgoing quark momentum (q) we can exploit momentum conservation and define

$$g\Gamma_\mu^a(k, p, q) = -ig(2\pi)^4 \delta(k + p - q) \Gamma_\mu^a(p, q). \quad (\text{B.16})$$

C. Derivation of Dyson-Schwinger equations

C.1. Quark DSE

Dyson-Schwinger equations can be obtained directly from the QCD generating functional using the identity

$$0 = \int \mathcal{D}[\varphi] \frac{\delta}{\delta \varphi_i} \exp(-S[\varphi] + J_j \varphi_j) \quad (\text{C.1})$$

where φ_i represent the QCD fields $(\bar{\psi}, \psi, A_\mu^a, \bar{c}^a, c^a)$ and J_i the corresponding sources. Carrying out the variation we obtain

$$0 = \left(\frac{\delta S}{\delta \varphi_i} \left[\pm \frac{\delta}{\delta J_j} \right] \mp J_i \right) Z[J] \quad (\text{C.2})$$

with the sign conventions from Eq. (B.4). We can use the relation

$$\frac{\delta}{\delta J_i} Z[J] = \frac{\delta}{\delta J_i} \exp(W[J]) = \exp(W[J]) \left(\frac{\delta W}{\delta J_i} + \frac{\delta}{\delta J_i} \right) \quad (\text{C.3})$$

in Eq. (C.2) and get with $J_i = \pm \frac{\delta \Gamma}{\delta \phi_i}$

$$\frac{\delta \Gamma}{\delta \phi_i} = \frac{\delta S}{\delta \varphi_i} \left[\pm \left(\frac{\delta W}{\delta J_j} + \frac{\delta}{\delta J_j} \right) \right]. \quad (\text{C.4})$$

With this equation, all DSE's can be derived by choosing an appropriate field $\varphi_i(x)$ and taking additional derivatives. The quark DSE is obtained with $\varphi_i(x) = \bar{\psi}(x)$ and taking the derivative $\frac{\delta}{\delta \bar{\psi}(y)}$. After inserting the action $S = \int d^4x \mathcal{L}$ with Eq. (2.14) we get

$$\begin{aligned} \frac{\delta^2 \Gamma}{\delta \bar{\psi}_\beta(y) \delta \bar{\psi}_\alpha(x)} &= \\ \frac{\delta}{\delta \bar{\psi}_\beta(y)} &\left(-Z_2 \not{\partial} + Z_2 Z_m m - Z_{1F} i g \gamma_\mu \frac{\lambda^a}{2} \left(\frac{\delta W}{\delta j_\nu^b(x)} + \frac{\delta}{\delta j_\nu^b(x)} \right) \right)_{\alpha\delta} \left(\frac{\delta W}{\delta \bar{\eta}_\delta(x)} + \frac{\delta}{\delta \bar{\eta}_\delta(x)} \right). \end{aligned} \quad (\text{C.5})$$

The last derivative can be performed using

$$\frac{\delta}{\delta\psi_\beta(y)} = \int_z \frac{\delta J_k(z)}{\delta\psi_\beta(y)} \frac{\delta}{\delta J_k(z)} = \pm \int_z \frac{\delta^2\Gamma}{\delta\psi_\beta(y)\delta\phi_k(z)} \frac{\delta}{\delta J_k(z)} \quad (\text{C.6})$$

with summation over k . Dropping all terms that do not contribute, we get

$$\begin{aligned} \frac{\delta^2\Gamma}{\delta\psi_\beta(y)\delta\bar{\psi}_\alpha(x)} &= \int_z \left((-Z_2\cancel{\partial} + Z_2Z_m m)_{\alpha_\delta} \frac{\delta^2W}{\delta\eta_\gamma(z)\delta\bar{\eta}_\delta(x)} \right. \\ &\quad \left. - Z_{1F}ig \left(\gamma_\mu \frac{\lambda^a}{2} \right)_{\alpha_\delta} \frac{\delta^3W}{\delta j_\nu^b(x)\delta\eta_\gamma(z)\delta\bar{\eta}_\delta(x)} \right) \frac{\delta^2\Gamma}{\delta\psi_\beta(y)\delta\bar{\psi}_\gamma(z)}. \end{aligned} \quad (\text{C.7})$$

Using the definitions in Appendix B, we arrive at the qDSE in coordinate space

$$S^{-1}(x, y) = Z_2 S_0^{-1}(x - y) + Z_{1F}ig^2 \gamma_\mu \frac{\lambda^a}{2} \int_{u,v} D_{\mu\nu}^{ab}(x, u) S(x, v) \Gamma_\nu^b(u, v, y). \quad (\text{C.8})$$

A Fourier transform leads to the DSE in momentum space

$$S^{-1}(p, p') = Z_2 S_0^{-1}(p, p') + Z_{1F}ig^2 \gamma_\mu \frac{\lambda^a}{2} \int_{q,q',q''} S(q, q') \Gamma_\nu^b(q'', q', p') D_{\mu\nu}^{ab}(p - q, q''). \quad (\text{C.9})$$

Assuming a homogeneous system and Eq. (B.16) simplifies the qDSE to

$$S^{-1}(p) = Z_2 S_0^{-1}(p) + Z_{1F}g^2 \gamma_\mu \frac{\lambda^a}{2} \int_q S(q) \Gamma_\nu^b(q, p) D_{\mu\nu}^{ab}(p - q). \quad (\text{C.10})$$

C.2. Gluon DSE

Choosing $\varphi_i(x) = A_\mu^a(x)$ in Eq. (C.4) and taking a further derivative with respect to $A_\nu^b(y)$ leads to the gluon DSE. The derivation is similar to the quark DSE, except it is more involved to take care of all contributions. We only present a simplified calculation where all Yang-Mills interactions are summarized to

$$\mathcal{L}_{YM,int} = \frac{1}{2} \int_{x,y} A_\mu^a(x) \Pi_{\mu\nu,YM}^{ab}(x, y) A_\nu^b(y). \quad (\text{C.11})$$

This also corresponds to the truncation we used in this work and we get (Eq. (C.4))

$$\begin{aligned} \frac{\delta^2 \Gamma}{\delta A_\nu^b(y) \delta A_\mu^a(x)} = & \frac{\delta}{\delta A_\nu^b(y)} \left(-\frac{\delta W}{\delta \eta(x)} - \frac{\delta}{\delta \eta(x)} \right) \left(-Z_{1F} i g \gamma_\mu \frac{\lambda^a}{2} \right) \left(\frac{\delta W}{\delta \bar{\eta}(x)} + \frac{\delta}{\delta \bar{\eta}(x)} \right) \\ & + Z_3 \left(-\partial^2 \delta_{\mu\nu} + \left(1 - \frac{1}{\xi} \right) \partial_\mu \partial_\nu \right) \left(\frac{\delta W}{\delta j_\mu^a(x)} + \frac{\delta}{\delta j_\mu^a(x)} \right) \\ & + \int_{z'} \Pi_{\mu\sigma, YM}^{ad}(x, z') \left(\frac{\delta W}{\delta j_\sigma^d(z')} + \frac{\delta}{\delta j_\sigma^d(z')} \right). \end{aligned} \quad (\text{C.12})$$

Using Eq. (C.6) with a derivative with respect to A_ν^b instead of ψ we get

$$\begin{aligned} \frac{\delta^2 \Gamma}{\delta A_\nu^b(y) \delta A_\mu^a(x)} = & Z_{1F} i g \int_z \frac{\delta^2 \Gamma}{\delta A_\nu^b(y) \delta A_\rho^c(z)} \left(\gamma_\mu \frac{\lambda^a}{2} \right)_{\alpha\beta} \frac{\delta^3 W}{\delta j_\rho^c(z) \delta \eta_\alpha(x) \delta \bar{\eta}_\beta(x)} \\ & + Z_3 \left(-\partial^2 \delta_{\mu\nu} + \left(1 - \frac{1}{\xi} \right) \partial_\mu \partial_\nu \right) \int_z \frac{\delta^2 \Gamma}{\delta A_\nu^b(y) \delta A_\rho^c(z)} \frac{\delta^2 W}{\delta j_\rho^c(z) \delta j_\mu^a(x)} \\ & + \int_{z, z'} \Pi_{\mu\sigma, YM}^{ad}(x, z') \frac{\delta^2 \Gamma}{\delta A_\nu^b(y) \delta A_\rho^c(z)} \frac{\delta^2 W}{\delta j_\rho^c(z) \delta j_\sigma^d(z')}. \end{aligned} \quad (\text{C.13})$$

With the definitions in Appendix B we get

$$\begin{aligned} D_{\mu\nu}^{ab}(x, y) = & Z_3 D_{\mu\nu,0}^{ab}(x, y) + \Pi_{\mu\nu, YM}^{ab}(x, y) \\ & - Z_{1F} i g^2 \int_{v,w} \text{Tr} \left(\gamma_\mu \frac{\lambda^a}{2} S(x, v) \Gamma_\nu^b(y, v, w) S(w, x) \right). \end{aligned} \quad (\text{C.14})$$

Performing the Fourier transformations gives

$$\begin{aligned} D_{\mu\nu}^{ab}(k, k') = & Z_3 D_{\mu\nu,0}^{ab}(k, k') + \Pi_{\mu\nu, YM}^{ab}(k, k') \\ & - Z_{1F} i g^2 \int_{q, q', q''} \text{Tr} \left(\gamma_\mu \frac{\lambda^a}{2} S(k+q, q') \Gamma_\nu^b(-k', q', q'') S(q'', q) \right). \end{aligned} \quad (\text{C.15})$$

and assuming homogeneous propagators we get the gluon DSE

$$D_{\mu\nu}^{ab}(k) = Z_3 D_{\mu\nu,0}^{ab}(k) + \Pi_{\mu\nu, YM}^{ab}(k) - Z_{1F} g^2 \int_q \text{Tr} \left(\gamma_\mu \frac{\lambda^a}{2} S(k+q) \Gamma_\nu^b(k+q, q) S(q) \right). \quad (\text{C.16})$$

D. Details on the gluon polarization

The gluon polarization for color-superconducting propagators is given by Eq. (3.7)

$$\Pi_{\mu\nu}^{ab}(k) = -2\pi\alpha(\nu) \int_q \text{Tr} \left(\Gamma_{\mu}^{a,0} \mathcal{S}(p) \Gamma_{\nu}^b(p, q) \mathcal{S}(q) \right). \quad (\text{D.1})$$

Using the symmetry relations from Section 2.4.3, the different contributions to the quark-loop integral can be related to simplify the expression. Using the internal NG symmetry Eq. (2.97) and shifting the integration variable $q \rightarrow -p$ the following properties can be derived easily

$$\begin{aligned} \int_q \text{Tr} \left[\gamma_{\mu} \frac{\lambda^a}{2} S^+(p) \gamma_{\nu} \frac{\lambda^b}{2} \Gamma(p, q) S^+(q) \right] &= \int_q \text{Tr} \left[\gamma_{\mu} \frac{\lambda^{a,T}}{2} S^-(p) \gamma_{\nu} \frac{\lambda^{b,T}}{2} \Gamma(p, q) S^-(q) \right] \\ \int_q \text{Tr} \left[\gamma_{\mu} \frac{\lambda^a}{2} T^-(p) \gamma_{\nu} \frac{\lambda^{b,T}}{2} \Gamma(p, q) T^+(q) \right] &= \int_q \text{Tr} \left[\gamma_{\mu} \frac{\lambda^{a,T}}{2} T^+(p) \gamma_{\nu} \frac{\lambda^b}{2} \Gamma(p, q) T^-(q) \right] \end{aligned} \quad (\text{D.2})$$

where the vertex dressing needs to fulfill $\Gamma(p, q) = \Gamma(-q, -p)$. In addition, with the vertex properties Eq. (2.109), we get

$$\begin{aligned} \int_q \text{Tr} \left[\gamma_{\mu} \frac{\lambda^a}{2} S^+(p) \Delta_{\nu}^{b,-}(p, q) T^+(q) \right] &= - \int_q \text{Tr} \left[\gamma_{\mu} \frac{\lambda^{a,T}}{2} T^+(p) \Delta_{\nu}^{b,-}(p, q) S^-(q) \right] \\ \int_q \text{Tr} \left[\gamma_{\mu} \frac{\lambda^a}{2} T^-(p) \Delta_{\nu}^{b,+}(p, q) S^+(q) \right] &= - \int_q \text{Tr} \left[\gamma_{\mu} \frac{\lambda^{a,T}}{2} S^-(p) \Delta_{\nu}^{b,+}(p, q) T^-(q) \right]. \end{aligned} \quad (\text{D.3})$$

The NG trace of the polarization can then be performed and gives

$$\begin{aligned} \Pi_{\mu\nu}^{ab}(k) &= -Z_{1F} 4\pi\alpha(\nu) \int_q \\ &\left\{ \text{Tr} \left[\gamma_{\mu} \frac{\lambda^a}{2} S^+(p) \gamma_{\nu} \frac{\lambda^b}{2} \Gamma(p, q) S^+(q) \right] - \text{Tr} \left[\gamma_{\mu} \frac{\lambda^a}{2} T^-(p) \gamma_{\nu} \frac{\lambda^{b,T}}{2} \Gamma(p, q) T^+(q) \right] \right. \\ &\left. + \text{Tr} \left[\gamma_{\mu} \frac{\lambda^a}{2} S^+(p) \Delta_{\nu}^{b,-}(p, q) T^+(q) \right] + \text{Tr} \left[\gamma_{\mu} \frac{\lambda^a}{2} T^-(p) \Delta_{\nu}^{b,+}(p, q) S^+(q) \right] \right\}. \end{aligned} \quad (\text{D.4})$$

The symmetries Eq. (2.99) and Eq. (2.106) give further relations:

$$\begin{aligned} \int_q \text{Tr} \left[\gamma_\mu \frac{\lambda^a}{2} S^+(p) \gamma_\nu \frac{\lambda^b}{2} \Gamma(p, q) S^+(q) \right] &= \int_q \text{Tr} \left[\gamma_\mu \frac{\lambda^{a,\dagger}}{2} S^+(p) \gamma_\nu \frac{\lambda^{b,\dagger}}{2} \Gamma(p, q) S^+(q) \right]^* \\ \int_q \text{Tr} \left[\gamma_\mu \frac{\lambda^a}{2} T^-(p) \gamma_\nu \frac{\lambda^{b,T}}{2} \Gamma(p, q) T^+(q) \right] &= \int_q \text{Tr} \left[\gamma_\mu \frac{\lambda^{a,\dagger}}{2} T^-(p) \gamma_\nu \frac{\lambda^{b,*}}{2} \Gamma(p, q) T^+(q) \right]^* \end{aligned} \quad (\text{D.5})$$

$$\int_q \text{Tr} \left[\gamma_\mu \frac{\lambda^a}{2} S^+(p) \Delta_\nu^{b,-}(p, q) T^+(q) \right] = - \int_q \text{Tr} \left[\gamma_\mu \frac{\lambda^{a,\dagger}}{2} T^-(p) \left(\Delta_\nu^{b,+}(-q, -p) \right)^\dagger S^+(q) \right]^* \quad (\text{D.6})$$

For the standard choice of the Gell-Mann matrices, they are Hermitian $\lambda^{a,\dagger} = \lambda^a$ and also the dressed anomalous vertex fulfills $\left(\Delta_\mu^{b,+}(-q, -p) \right)^\dagger = -\Delta_\mu^{a,-}(p, q)$, which ensures a real gluon polarization tensor. Eq. (D.4) then simplifies to

$$\begin{aligned} \Pi_{\mu\nu}^{ab}(k) &= -Z_{1F} 4\pi \alpha(\nu) \int_q \text{Re} \left\{ \text{Tr} \left[\gamma_\mu \frac{\lambda^a}{2} S^+(p) \gamma_\nu \frac{\lambda^b}{2} \Gamma(p, q) S^+(q) \right] \right. \\ &\quad \left. - \text{Tr} \left[\gamma_\mu \frac{\lambda^a}{2} T^-(p) \gamma_\nu \frac{\lambda^{b,T}}{2} \Gamma(p, q) T^+(q) \right] + 2 \text{Tr} \left[\gamma_\mu \frac{\lambda^a}{2} S^+(p) \Delta_\nu^{b,-}(p, q) T^+(q) \right] \right\}. \end{aligned} \quad (\text{D.7})$$

In a pure CFL phase the color-flavor traces of the three components of Eq. (D.7) are given by

$$\begin{aligned} \text{Tr}_{cf}(\lambda^a P_i \lambda^b P_j) &= \left(\frac{14}{3} \delta_{i,8} \delta_{j,8} + \frac{2}{3} \delta_{i,1} \delta_{j,8} + \frac{2}{3} \delta_{i,8} \delta_{j,1} \right) \delta^{ab} \\ \text{Tr}_{cf}(\lambda^a M_i \lambda^{b,T} M_j) &= -\frac{4}{3} (\delta_{i,8} \delta_{j,8} + \delta_{i,1} \delta_{j,8} + \delta_{i,8} \delta_{j,1}) \delta^{ab} \\ \text{Tr}_{cf} \left(\lambda^a P_i (\lambda^b M_j + M_j \lambda^{b,T}) M_k \right) &= \left(-\frac{4}{3} \delta_{i,1} \delta_{j,1} \delta_{k,8} + \frac{2}{3} \delta_{i,1} \delta_{j,8} \delta_{k,8} \right. \\ &\quad \left. + \frac{8}{3} \delta_{i,8} \delta_{j,1} \delta_{k,1} - \frac{4}{3} \delta_{i,8} \delta_{j,8} \delta_{k,1} + \frac{10}{3} \delta_{i,8} \delta_{j,8} \delta_{k,8} \right) \delta^{ab}. \end{aligned} \quad (\text{D.8})$$

They are all diagonal in color space and therefore also the gluon is diagonal in a CFL phase. This feature is also expected, as the CFL phase exhibits a large residual symmetry and all colors are on equal footing.

This is different in a 2SC phase or with finite strange-quark masses. For these phases, the polarization does not have to be diagonal in general. However, it can be diagonalized

using a set of rotated Gell-Mann matrices Eq. (4.40). Then, $\lambda^{a,\dagger} \neq \lambda^a$ for $a = 4, 5, 6, 7$ and the corresponding polarization components are not real anymore. Instead, they fulfill $\Pi_{\mu\nu}^{44}(k) = \Pi_{\mu\nu}^{66}(k) = \Pi_{\mu\nu}^{55}(k)^* = \Pi_{\mu\nu}^{77}(k)^*$. So we can get a diagonal gluon polarization by changing the basis of the Gell-Mann matrices with the downside of getting complex components. The other components stay real, as the Gell-Mann matrices $\lambda^{a=1,2,3,8}$ are not modified.

For a 2SC phase we now also evaluate the color-flavor trace, giving various contributions to the different gluon channels:

$$\begin{aligned}
\Pi_{\mu\nu}^{ab}(k) = & -Z_{1F} 4\pi\alpha(\nu) \int_q \Gamma(p, q) \\
& \left(\left\{ \text{Tr} \left[\gamma_\mu S_{ud,rg}^+(p) \gamma_\nu S_{ud,rg}^+(q) \right] + \frac{1}{2} \text{Tr} \left[\gamma_\mu S_{s,rg}^+(p) \gamma_\nu S_{s,rg}^+(q) \right] \right. \right. \\
& \quad \left. \left. + \text{Tr} \left[\gamma_\mu T_{2SC}^-(p) \gamma_\nu T_{2SC}^+(q) \right] \right\} \left(\delta^{a1}\delta^{b1} + \delta^{a2}\delta^{b2} + \delta^{a3}\delta^{b3} \right) \right. \\
& \quad \left. + \left\{ \text{Tr} \left[\gamma_\mu S_{ud,b}^+(p) \gamma_\nu S_{ud,rg}^+(q) \right] + \text{Tr} \left[\gamma_\mu S_{s,b}^+(p) \gamma_\nu S_{s,rg}^+(q) \right] \right\} \left(\delta^{a4}\delta^{b4} + \delta^{a6}\delta^{b6} \right) \right. \\
& \quad \left. + \left\{ \text{Tr} \left[\gamma_\mu S_{ud,rg}^+(p) \gamma_\nu S_{ud,b}^+(q) \right] + \text{Tr} \left[\gamma_\mu S_{s,rg}^+(p) \gamma_\nu S_{s,b}^+(q) \right] \right\} \left(\delta^{a5}\delta^{b5} + \delta^{a7}\delta^{b7} \right) \right. \\
& \quad \left. + \left\{ \frac{1}{3} \text{Tr} \left[\gamma_\mu S_{ud,rg}^+(p) \gamma_\nu S_{ud,rg}^+(q) \right] + \frac{2}{3} \text{Tr} \left[\gamma_\mu S_{ud,b}^+(p) \gamma_\nu S_{ud,b}^+(q) \right] \right. \right. \\
& \quad \left. \left. + \frac{1}{6} \text{Tr} \left[\gamma_\mu S_{s,rg}^+(p) \gamma_\nu S_{s,rg}^+(q) \right] + \frac{1}{3} \text{Tr} \left[\gamma_\mu S_{s,b}^+(p) \gamma_\nu S_{s,b}^+(q) \right] \right. \right. \\
& \quad \left. \left. - \frac{1}{3} \text{Tr} \left[\gamma_\mu T_{2SC}^-(p) \gamma_\nu T_{2SC}^+(q) \right] \right\} \delta^{a8}\delta^{b8} \right. \\
& \quad \left. + \left\{ \text{Tr} \left[\gamma_\mu S_{ud,b}^+(p) \left[-i \frac{k_\nu}{2k^2} (\Phi_{2SC}^-(p) + \Phi_{2SC}^-(q)) \right] T_{2SC}^+(q) \right] \right\} \left(\delta^{a4}\delta^{b4} + \delta^{a6}\delta^{b6} \right) \right. \\
& \quad \left. + \left\{ \text{Tr} \left[\gamma_\mu T_{2SC}^-(p) \left[i \frac{k_\nu}{2k^2} (\Phi_{2SC}^+(p) + \Phi_{2SC}^+(q)) \right] S_{ud,b}^+(q) \right] \right\} \left(\delta^{a5}\delta^{b5} + \delta^{a7}\delta^{b7} \right) \right. \\
& \quad \left. + \left\{ \frac{2}{3} \text{Tr} \left[\gamma_\mu S_{ud,rg}^+(p) \left[-i \frac{k_\nu}{2k^2} (\Phi_{2SC}^-(p) + \Phi_{2SC}^-(q)) \right] T_{2SC}^+(q) \right] \right. \right. \\
& \quad \left. \left. + \left\{ \frac{2}{3} \text{Tr} \left[\gamma_\mu T_{2SC}^-(p) \left[i \frac{k_\nu}{2k^2} (\Phi_{2SC}^+(p) + \Phi_{2SC}^+(q)) \right] S_{ud,rg}^+(q) \right] \right\} \delta^{a8}\delta^{b8} \right. \right) \quad (D.9)
\end{aligned}$$

The calculation of these contributions for massive strange quarks is straight forward, but gives many more contributing terms which we do not want to write down explicitly.

E. Numerical calculation

The quark Dyson-Schwinger equation is schematically given by the system of equations

$$S^{-1}(p) = S_0^{-1}(p) + \Sigma(p) \quad (\text{E.1})$$

$$\Sigma(p) = \int_q S(q) K(p, q) \quad (\text{E.2})$$

with an integration kernel $K(p, q)$ that depends on the gluon propagator and the quark-gluon vertex. We discretize the quark self-energy on a 2-dimensional grid $\Sigma(p_{4,i}, |\vec{p}|_j)$. The energy component is constrained to Matsubara frequencies ω_n but for not too small temperatures ($T \gtrsim 10$ MeV) it is sufficient to include only the first 10 Matsubara frequencies explicitly and to discretize higher energies like a continuous energy. The higher energies and the 3-momenta are discretized on a logarithmic scale while the coarseness is chosen according to the importance of the region. Especially near the Fermi momentum that is typically located around μ we choose a finer discretization at low energies. We choose an IR cutoff of 1 MeV and an UV cutoff of 1000 GeV that are small respectively large enough that their effects are negligible. For the numerical integration we need to choose a grid with finer integration nodes q_i to reach a high enough accuracy and we interpolate $\Sigma(p_i)$ to $\Sigma(q_i)$ bilinearly. We calculate the propagator at each gridpoint by evaluating Eq. (E.1) and inverting the result and obtain the self-energy by numerical evaluation of Eq. (E.2). It is essential to interpolate on the level of the self-energy which is much smoother than the propagator and therefore requires less gridpoints.

For the numerical integration we use a simple Riemann quadrature which is also quite stable in the region of the peaked propagator at the Fermi surface.

The system Eq. (E.1) and Eq. (E.2) is iterated until the desired accuracy is reached. When the quark propagator is coupled back to the gluon self-consistently we want to evaluate the time consuming gluon polarization integral not in every iteration step and we proceed as follows. We calculate the gluon polarization for a quark propagator S . Then we iterate the quark DSE with the calculated gluon until convergence and the resulting quark propagator is used to update the gluon polarization. This procedure is repeated until the full iteration is converged.

The gluon polarization

$$\Pi(k) = \int_q S(q)S(q+k)\tilde{K}(p,q) \quad (\text{E.3})$$

is calculated analogously to the quark self-energy. The discretization of $\Pi(k)$ has the difference that bosonic Matsubara frequencies $k_4 = \omega_m$ need to be used for low energies. To obtain the quark propagator $S(q+k)$, which also depends on the angle between \vec{q} and \vec{k} , the propagator needs to be interpolated also for $q+k$. The gluon polarization therefore needs much more interpolations and propagator evaluations, which makes it numerically more expensive than the quark self-energy. The regularization (Sec. 4.3) is also not easy to implement numerically. The regularized polarization function Π_T for bare vacuum propagators has the asymptotic limit $q \gg k$ which determines the convergence (cf. Eq. (4.19))

$$\int \frac{d^4q}{(2\pi)^4} \frac{-\frac{2}{3}q^2 + \frac{8}{3}q^2 \cos^2 \psi}{(q^2)^2} \quad (\text{E.4})$$

where we used hyperspherical coordinates Eq. (A.9). Performing the ψ -integration, the result vanishes which regularizes the full polarization integral. The numerical evaluation of this integral requires a high accuracy, as there is no symmetry of the integrand, that can be used for canceling the divergent terms. Additionally, in medium, we have to use the parametrization Eq. (A.10)

$$T \sum_{\omega_n} \int \frac{d^3q}{(2\pi)^3} \frac{-\frac{2}{3}(\omega_n^2 + |\vec{q}|^2) + \frac{8}{3} \frac{(\omega_n \omega_m + |\vec{q}| |\vec{k}| \cos \theta)^2}{k^2}}{(\omega_n^2 + |\vec{q}|^2)^2} \quad (\text{E.5})$$

and the integral only vanishes when ω_n and $|\vec{q}|$ are constrained by an $O(4)$ cutoff via $\omega_n^2 + |\vec{q}|^2 < \Lambda^2$, otherwise the quadratic divergence remains. In principle, this would provide a cutoff-independent result, but numerically, this regularization is very unstable. We therefore choose a different numerical regularization and calculate

$$\Pi_T(k) - \Pi_L(k) - (\Pi_T(0) - \Pi_L(0))_{T=0,\mu=0}. \quad (\text{E.6})$$

If all terms have the same integration nodes for large q , this expression shows no quadratic divergencies, independent of the coarseness of the nodes, as there is always a pair of terms $\Pi(k) - \Pi(0)$ which cancel the divergencies of each other. If calculated with vacuum dressing functions, the subtracted term $\Pi_{sub} = (\Pi_T(0) - \Pi_L(0))_{T=0,\mu=0}$ is zero analytically and serves solely for numerical stabilization. In medium, we only can

preserve this advantage by taking medium dressing functions $A(q)$, $B(q)$ and $C(q)$ in the regulator. We evaluate Π_{sub} with the real part of these dressing functions and set all other dressings as well as the explicit occurrences of T and μ to zero. If $A(q) = C(q)$ this contribution still vanishes due to the arguments discussed above. As $A(q)$ and $C(q)$ differ in medium, this term is not exactly zero and leads to a small truncation error, that also violates the Silver-Blaze property. Although this regulator seems a bit arbitrary, the result only slightly changes by testing variations of the regularization like setting also $B(q) = 0$ or using $\frac{1}{2}(A(q) + C(q))$ instead of $A(q)$ and $C(q)$. The regularization therefore is quite robust and we neglect the error for the benefit of a numerically stable expression for the polarization function. Without this subtraction, other approximations like the introduction of a cutoff are needed for the numerical calculation which usually lead to even larger errors.

F. A remark on the iterative procedure

Throughout this work we used a fixed point iteration to obtain the solutions of the DSE. In general, not every solution can be found iteratively and for an iterative condition

$$x_{i+1} = \varphi(x_i) \quad (\text{F.1})$$

with a fixed point $x^* = \varphi(x^*)$, the iteration converges if the iteration is contracting, i.e.

$$\frac{|x_{i+1} - x^*|}{|x_i - x^*|} = \frac{|\varphi(x_i) - \varphi(x^*)|}{|x_i - x^*|} \stackrel{!}{\leq} L \quad (\text{F.2})$$

with a constant $L < 1$. This expression is just the discretized derivative $|\varphi'(x^*)|$.

For a mean-field NJL model, this property can be investigated analytically. The NJL Lagrangian is given by [107]

$$\mathcal{L}_{NJL} = \bar{\psi}(i\cancel{\partial} - m)\psi + G [(\bar{\psi}\psi)^2 + (\bar{\psi}i\gamma_5\vec{\tau}\psi)^2] \quad (\text{F.3})$$

with an NJL coupling constant G and the bare quark mass m . In mean-field approximation, the thermodynamic potential in vacuum is given by (e.g. [80])

$$\Omega_{NJL} = \frac{(M - m)^2}{4G} - 2N_c N_f \int \frac{d^3 q}{(2\pi)^3} \sqrt{\vec{q}^2 + M^2} \quad (\text{F.4})$$

with the dressed quark mass M . Additionally a regularization needs to be specified, as the integral is divergent. The gap equation (DSE) can be derived by

$$\frac{\delta \Omega}{\delta M} = \frac{M - \varphi(M)}{2G} \stackrel{!}{=} 0 \quad (\text{F.5})$$

with

$$\varphi(M) = m + 4G N_c N_f \int \frac{d^3 q}{(2\pi)^3} \frac{M}{\sqrt{\vec{q}^2 + M^2}} \quad (\text{F.6})$$

which has the solutions M^* . By investigating the second derivative, we can see the physical stability of the solution:

$$\frac{\delta^2 \Omega}{\delta M^2} \Big|_{M=M^*} = \frac{1}{2G} \left(1 - \frac{d\varphi(M)}{dM} \Big|_{M=M^*} \right) \quad (\text{F.7})$$

Therefore, the solution corresponds to a minimum if $\varphi'(M^*) < 1$ and to a maximum if $\varphi'(M^*) > 1$. The derivative of $\varphi(M)$ is given by

$$\varphi'(M) = 4GN_cN_f \int \frac{d^3q}{(2\pi)^3} \frac{\vec{q}^2}{(\vec{q}^2 + M^2)^{3/2}} \quad (\text{F.8})$$

which is positive for all values of M . Therefore, we have

$$|\varphi'(M^*)| \begin{cases} < 1 & \text{for a minimum of } \Omega \\ > 1 & \text{for a maximum of } \Omega. \end{cases} \quad (\text{F.9})$$

With Eq. (F.2) we see immediately that maxima of the potential correspond to numerical unstable iterative solutions, while minima are numerically stable. This allows in principle to find all minima of the potential by iterating the gap equation. It can also be checked easily, that the introduction of finite temperature and chemical potential does not change these arguments. For QCD DSEs, the situation is much more complicated as we have functional derivatives and an in principle infinite-dimensional system. Therefore, we cannot provide an analogous analytic argument for the relation between physical and numerical stability, however, we expect this relation still to be valid.

Bibliography

- [1] G. Aad, T. Abajyan, B. Abbott, J. Abdallah, S. Abdel Khalek, A. A. Abdelalim, O. Abdinov, R. Aben, B. Abi, M. Abolins and et al., *Observation of a new particle in the search for the Standard Model Higgs boson with the ATLAS detector at the LHC*, Physics Letters B **716**, 1–29 (2012).
- [2] S. Chatrchyan, V. Khachatryan, A. M. Sirunyan, A. Tumasyan, W. Adam, E. Aguilo, T. Bergauer, M. Dragicevic, J. Erö, C. Fabjan and et al., *Observation of a new boson at a mass of 125 GeV with the CMS experiment at the LHC*, Physics Letters B **716**, 30–61 (2012).
- [3] D. J. Gross and F. Wilczek, *Ultraviolet Behavior of Non-Abelian Gauge Theories*, Physical Review Letters **30**, 1343–1346 (1973).
- [4] H. D. Politzer, *Reliable Perturbative Results for Strong Interactions?*, Physical Review Letters **30**, 1346–1349 (1973).
- [5] A. M. Jaffe and E. Witten, *Quantum Yang-Mills theory*, (2000), www.claymath.org/millennium/Yang-Mills_Theory/yangmills.pdf.
- [6] GSI Helmholtzzentrum für Schwerionenforschung, *The phase diagram of strongly interacting matter*.
- [7] P. Braun-Munzinger and J. Stachel, *The quest for the quark-gluon plasma*, Nature **448**, 302–309 (2007).
- [8] P. Braun-Munzinger and J. Wambach, *Colloquium: Phase diagram of strongly interacting matter*, Reviews of Modern Physics **81**, 1031–1050 (2009).
- [9] K. Fukushima and T. Hatsuda, *The phase diagram of dense QCD*, Reports on Progress in Physics **74**, 014001 (2011).
- [10] K. Adcox, S. S. Adler, N. N. Ajitanand, Y. Akiba, J. Alexander, L. Aphecetche, Y. Arai, S. H. Aronson, R. Averbeck, T. C. Awes and et al., *Suppression of Hadrons with Large Transverse Momentum in Central Au+Au Collisions at (s_{NN}) = 130 GeV*, Physical Review Letters **88**, 022301 (2002).

Bibliography

- [11] C. Adler, Z. Ahammed, C. Allgower, J. Amonett, B. D. Anderson, M. Anderson, G. S. Averichev, J. Balewski, O. Barannikova, L. S. Barnby and et al., *Disappearance of Back-To-Back High- p_T Hadron Correlations in Central Au+Au Collisions at $(s_{NN})=200$ GeV*, Physical Review Letters **90**, 082302 (2003).
- [12] G. Aad, B. Abbott, J. Abdallah, A. A. Abdelalim, A. Abdesselam, O. Abdinov, B. Abi, M. Abolins, H. Abramowicz, H. Abreu and et al., *Observation of a Centrality-Dependent Dijet Asymmetry in Lead-Lead Collisions at $s_{NN}=2.76$ TeV with the ATLAS Detector at the LHC*, Physical Review Letters **105**, 252303 (2010).
- [13] P. Braun-Munzinger, K. Redlich and J. Stachel, Particle Production in Heavy Ion Collisions, In R. C. Hwa and X.-N. Wang, editors, *Quark-Gluon Plasma*, page 491 (2004).
- [14] A. Andronic, P. Braun-Munzinger and J. Stachel, *Thermal hadron production in relativistic nuclear collisions*, Acta Phys. Polon. **B40**, 1005–1012 (2009).
- [15] A. Andronic, P. Braun-Munzinger, K. Redlich and J. Stachel, *The statistical model in Pb-Pb collisions at the LHC*, arXiv:1210.7724 [nucl-th] (2012).
- [16] S. Borsányi, Z. Fodor, C. Hoelbling, S. D. Katz, S. Krieg, C. Ratti and K. K. Szabó, *Is there still any T_c mystery in lattice QCD? Results with physical masses in the continuum limit III*, Journal of High Energy Physics **9**, 73 (2010).
- [17] A. Bazavov, T. Bhattacharya, M. Cheng, C. Detar, H.-T. Ding, S. Gottlieb, R. Gupta, P. Hegde, U. M. Heller, F. Karsch, E. Laermann, L. Levkova, S. Mukherjee, P. Petreczky, C. Schmidt, R. A. Soltz, W. Söldner, R. Sugar, D. Toussaint, W. Unger and P. Vranas, *Chiral and deconfinement aspects of the QCD transition*, Phys. Rev. **D85**, 054503 (2012).
- [18] P. de Forcrand and O. Philipsen, *Constraining the QCD Phase Diagram by Tricritical Lines at Imaginary Chemical Potential*, Physical Review Letters **105**, 152001 (2010).
- [19] G. Endrődi, Z. Fodor, S. D. Katz, Szabó and K. K., *The QCD phase diagram at nonzero quark density*, Journal of High Energy Physics **4**, 1 (2011).
- [20] O. Kaczmarek, F. Karsch, E. Laermann, C. Miao, S. Mukherjee, P. Petreczky, C. Schmidt, W. Söldner and W. Unger, *Phase boundary for the chiral transition in (2+1)-flavor QCD at small values of the chemical potential*, Phys. Rev. **D83**, 014504 (2011).

- [21] F. Karsch, B.-J. Schaefer, M. Wagner and J. Wambach, *Towards finite density QCD with Taylor expansions*, Physics Letters B **698**, 256–264 (2011).
- [22] S. Borsányi, G. Endrődi, Z. Fodor, S. D. Katz, S. Krieg, C. Ratti and K. K. Szabó, *QCD equation of state at nonzero chemical potential: continuum results with physical quark masses at order μ^2* , Journal of High Energy Physics **8**, 53 (2012).
- [23] M. Alford, K. Rajagopal and F. Wilczek, *Color-flavor locking and chiral symmetry breaking in high density QCD*, Nuclear Physics B **537**, 443–458 (1999).
- [24] T. Schäfer, *Patterns of symmetry breaking in QCD at high baryon density*, Nuclear Physics B **575**, 269–284 (2000).
- [25] I. A. Shovkovy and L. C. R. Wijewardhana, *On gap equations and color-flavor locking in cold dense QCD with three massless flavors*, Physics Letters B **470**, 189–199 (1999).
- [26] H. Abuki and T. Kunihiro, *Extensive study of phase diagram for charge-neutral homogeneous quark matter affected by dynamical chiral condensation: unified picture for thermal unpairing transitions from weak to strong coupling*, Nuclear Physics A **768**, 118–159 (2006).
- [27] S. B. Rüster, V. Werth, M. Buballa, I. A. Shovkovy and D. H. Rischke, *Phase Diagram of Neutral Quark Matter at Moderate Densities*, In A. Sedrakian, J. W. Clark and M. Alford, editors, *Pairing in Fermionic Systems: Basic Concepts and Modern Applications*, page 63, World Scientific Publishing Co (2006).
- [28] D. Blaschke, S. Fredriksson, H. Grigorian, A. M. Öztaş and F. Sandin, *Phase diagram of three-flavor quark matter under compact star constraints*, Phys. Rev. D**72**, 065020 (2005).
- [29] W. Broniowski, *Chiral waves in quark matter*, Acta Phys.Polon.Supp. **5**, 631 (2012).
- [30] A. W. Overhauser, *Structure of Nuclear Matter*, Physical Review Letters **4**, 415–418 April 1960.
- [31] D. V. Deryagin, D. Y. Grigoriev and V. A. Rubakov, *Standing Wave Ground State in High Density, Zero Temperature QCD at Large N_C* , International Journal of Modern Physics A **7**, 659–681 (1992).

- [32] E. Shuster and D. T. Son, *On finite-density QCD at large N_c* , Nuclear Physics B **573**, 434–446 (2000).
- [33] M. Sadzikowski and W. Broniowski, *Non-uniform chiral phase in effective chiral quark models*, Physics Letters B **488**, 63–67 (2000).
- [34] E. Nakano and T. Tatsumi, *Chiral symmetry and density waves in quark matter*, Phys. Rev. D**71**, 114006 (2005).
- [35] D. Nickel, *Inhomogeneous phases in the Nambu-Jona-Lasinio and quark-meson model*, Phys. Rev. D**80**, 074025 (2009).
- [36] C. D. Roberts and A. G. Williams, *Dyson-Schwinger equations and their application to hadronic physics*, Progress in Particle and Nuclear Physics **33**, 477–575 (1994).
- [37] C. D. Roberts and S. M. Schmidt, *Dyson-Schwinger Equations: Density, Temperature and Continuum Strong QCD*, Progress in Particle and Nuclear Physics **45**, 1 (2000).
- [38] R. Alkofer and L. von Smekal, *The infrared behaviour of QCD Green's functions: Confinement, dynamical symmetry breaking, and hadrons as relativistic bound states*, Phys. Rep.**353**, 281–465 (2001).
- [39] P. Maris and C. D. Roberts, *Dyson-Schwinger Equations*, International Journal of Modern Physics E **12**, 297–365 (2003).
- [40] C. S. Fischer, *Infrared properties of QCD from Dyson-Schwinger equations*, Journal of Physics G Nuclear Physics **32**, 253 (2006).
- [41] C. S. Fischer, A. Maas and J. M. Pawłowski, *On the infrared behavior of Landau gauge Yang-Mills theory*, Annals of Physics **324**, 2408–2437 (2009).
- [42] C. S. Fischer and J. A. Müller, *Chiral and deconfinement transition from Dyson-Schwinger equations*, Phys. Rev. D**80**, 074029 (2009).
- [43] C. S. Fischer, A. Maas and J. A. Müller, *Chiral and deconfinement transition from correlation functions: $SU(2)$ vs. $SU(3)$* , European Physical Journal C **68**, 165–181 (2010).
- [44] C. S. Fischer, J. Lücker and J. A. Müller, *Chiral and deconfinement phase transitions of two-flavour QCD at finite temperature and chemical potential*, Physics Letters B **702**, 438–441 (2011).

- [45] C. S. Fischer and J. Lücker, *Propagators and phase structure of $N_f=2$ and $N_f=2+1$ QCD*, Physics Letters B **718**, 1036–1043 (2013).
- [46] D. Nickel, J. Wambach and R. Alkofer, *Color superconductivity in the strong-coupling regime of Landau gauge QCD*, Phys. Rev. D**73**, 114028 (2006).
- [47] D. Nickel, R. Alkofer and J. Wambach, *Unlocking of color and flavor in color-superconducting quark matter*, Phys. Rev. D**74**, 114015 (2006).
- [48] D. Nickel, R. Alkofer and J. Wambach, *Neutrality of the color-flavor-locked phase in a Dyson-Schwinger approach*, Phys. Rev. D**77**, 114010 (2008).
- [49] J. Pawłowski, *Aspects of the functional renormalisation group*, Annals of Physics **322**, 2831–2915 (2007).
- [50] J. M. Pawłowski, *The QCD phase diagram: Results and challenges*, AIP Conf. Proc. **1343**, 75–80 (2011).
- [51] T. K. Herbst, J. M. Pawłowski and B.-J. Schaefer, *The phase structure of the Polyakov-quark-meson model beyond mean field*, Physics Letters B **696**, 58–67 (2011).
- [52] V. Skokov, B. Friman and K. Redlich, *Quark number fluctuations in the Polyakov loop-extended quark-meson model at finite baryon density*, Phys. Rev. C**83**, 054904 (2011).
- [53] D. Müller, M. Buballa and J. Wambach, *Dyson-Schwinger approach to color superconductivity at finite temperature and density*, arXiv:1303.2693 [hep-ph] (2013).
- [54] V. N. Gribov, *Quantization of non-Abelian gauge theories*, Nuclear Physics B **139**, 1–19 (1978).
- [55] M. E. Peskin and D. V. Schroeder, *An Introduction to Quantum Field Theory*, Westview Press (1995).
- [56] J. C. Taylor, *Ward identities and charge renormalization of the Yang-Mills field*, Nuclear Physics B **33**, 436–444 (1971).
- [57] M. Le Bellac, *Thermal Field Theory*, Cambridge University Press (2000).
- [58] S. Elitzur, *Impossibility of spontaneously breaking local symmetries*, Phys. Rev. D**12**, 3978–3982 (1975).

- [59] P. W. Anderson, *Plasmons, Gauge Invariance, and Mass*, Physical Review **130**, 439–442 (1963).
- [60] P. W. Higgs, *Broken Symmetries and the Masses of Gauge Bosons*, Physical Review Letters **13**, 508–509 (1964).
- [61] S. L. Adler, *Axial-Vector Vertex in Spinor Electrodynamics*, Physical Review **177**, 2426–2438 (1969).
- [62] J. S. Bell and R. Jackiw, *A PCAC puzzle: $\pi^0 \rightarrow \gamma\gamma$ in the σ -model*, Nuovo Cimento A Serie **60**, 47–61 (1969).
- [63] A. Maas, J. Wambach, B. Grüter and R. Alkofer, *High-temperature limit of Landau-gauge Yang-Mills theory*, European Physical Journal C **37**, 335–357 (2004).
- [64] A. Maas, J. Wambach and R. Alkofer, *The high-temperature phase of Landau-gauge Yang-Mills theory*, European Physical Journal C **42**, 93–107 (2005).
- [65] A. Cucchieri, A. Maas and T. Mendes, *Infrared properties of propagators in Landau-gauge pure Yang-Mills theory at finite temperature*, Phys. Rev. D**75**, 076003 (2007).
- [66] R. Alkofer, C. S. Fischer, F. J. Llanes-Estrada and K. Schwenzer, *The quark-gluon vertex in Landau gauge QCD: Its role in dynamical chiral symmetry breaking and quark confinement*, Annals of Physics **324**, 106–172 (2009).
- [67] J. M. Cornwall, R. Jackiw and E. Tomboulis, *Effective action for composite operators*, Phys. Rev. D**10**, 2428–2445 (1974).
- [68] P. Maris, C. D. Roberts and P. C. Tandy, *Pion mass and decay constant*, Physics Letters B **420**, 267–273 (1998).
- [69] P. Petreczky, *Lattice QCD at non-zero temperature*, Journal of Physics G Nuclear Physics **39**, 093002 (2012).
- [70] R. Williams, C. S. Fischer and M. R. Pennington, *Extracting the $\bar{q}q$ condensate for light quarks beyond the chiral limit in models of QCD*, arXiv:0704.2296 [hep-ph] (2007).
- [71] B. R. Holstein, *How large is f_π ?*, Physics Letters B **244**, 83–87 (1990).

- [72] H. Pagels and S. Stokar, *Pion decay constant, electromagnetic form factor, and quark electromagnetic self-energy in quantum chromodynamics*, Phys. Rev. D**20**, 2947–2952 (1979).
- [73] M. Gell-Mann, R. J. Oakes and B. Renner, *Behavior of Current Divergences under $SU_3 \times SU_3$* , Physical Review **175**, 2195–2199 (1968).
- [74] J. Bardeen, L. N. Cooper and J. R. Schrieffer, *Microscopic Theory of Superconductivity*, Physical Review **106**, 162–164 (1957).
- [75] J. Bardeen, L. N. Cooper and J. R. Schrieffer, *Theory of Superconductivity*, Physical Review **108**, 1175–1204 (1957).
- [76] K. Rajagopal and F. Wilczek, *The Condensed Matter Physics of QCD*, arXiv:hep-ph/0011333 (2000).
- [77] M. Alford, *Color-Superconducting Quark Matter*, Annual Review of Nuclear and Particle Science **51**, 131–160 (2001).
- [78] T. Schäfer, *Quark Matter*, Proc. of the BARC workshop on Quarks and Mesons, Mumbai (2003).
- [79] D. H. Rischke, *The quark-gluon plasma in equilibrium*, Progress in Particle and Nuclear Physics **52**, 197–296 (2004).
- [80] M. Buballa, *NJL-model analysis of dense quark matter*, Phys. Rep. **407**, 205–376 (2005).
- [81] I. A. Shovkovy, *Two Lectures on Color Superconductivity*, Foundations of Physics **35**, 1309–1358 (2005).
- [82] M. G. Alford, A. Schmitt, K. Rajagopal and T. Schäfer, *Color superconductivity in dense quark matter*, Reviews of Modern Physics **80**, 1455–1515 (2008).
- [83] R. D. Pisarski and D. H. Rischke, *Superfluidity in a model of massless fermions coupled to scalar bosons*, Phys. Rev. D**60**, 094013 (1999).
- [84] K. Zarembo, *Dispersion laws for Goldstone bosons in a color superconductor*, Phys. Rev. D**62**, 054003 (2000).
- [85] D. H. Rischke, *Debye screening and the Meissner effect in a three-flavor color superconductor*, Phys. Rev. D**62**, 054017 (2000).

- [86] M. Alford, J. Berges and K. Rajagopal, *Unlocking color and flavor in superconducting strange quark matter*, Nuclear Physics B **558**, 219–242 (1999).
- [87] J. Skullerud, A. Ki Izilersü and A. G. Williams, *Quark-gluon vertex in a momentum subtraction scheme*, Nuclear Physics B Proceedings Supplements **106**, 841–843 (2001).
- [88] C. S. Fischer and R. Williams, *Probing the Gluon Self-Interaction in Light Mesons*, Physical Review Letters **103**, 122001 (2009).
- [89] A. Windisch, M. Hopfer and R. Alkofer, *Towards a self-consistent solution of the Landau gauge quark-gluon vertex Dyson-Schwinger equation*, Acta Phys.Polon.Supp. **6**, 347–352 (2013).
- [90] M. Hopfer, A. Windisch and R. Alkofer, *The Quark-Gluon Vertex in Landau gauge QCD*, PoS Confinement X page 073 (2013).
- [91] J. S. Ball and T.-W. Chiu, *Analytic properties of the vertex function in gauge theories. I*, Phys. Rev. D**22**, 2542–2549 (1980).
- [92] R. Aouane, V. G. Bornyakov, E.-M. Ilgenfritz, V. K. Mitrjushkin, M. Müller-Preussker and A. Sternbeck, *Landau gauge gluon and ghost propagators at finite temperature from quenched lattice QCD*, Phys. Rev. D**85**, 034501 (2012).
- [93] J. Beringer and et al., *Review of Particle Physics*, Phys. Rev. D**86**, 010001 (2012).
- [94] T. van Ritbergen, J. A. M. Vermaseren and S. A. Larin, *The four-loop β -function in quantum chromodynamics. I*, Physics Letters B **400**, 379–384 (1997).
- [95] M. Buballa and M. Oertel, *Color-flavor unlocking and phase diagram with self-consistently determined strange-quark masses*, Nuclear Physics A **703**, 770–784 (2002).
- [96] N. Brown and M. R. Pennington, *Studies of confinement: How quarks and gluons propagate*, Phys. Rev. D**38**, 2266–2276 (1988).
- [97] D. H. Rischke, *Debye screening and the Meissner effect in a two-flavor color superconductor*, Phys. Rev. D**62**, 034007 (2000).
- [98] W. Marciano and H. Pagels, *Quantum chromodynamics*, Phys. Rep. **36**, 137–276 (1978).

- [99] T. D. Cohen, *Functional Integrals for QCD at Nonzero Chemical Potential and Zero Density*, Physical Review Letters **91**, 222001 (2003).
- [100] T. D. Cohen, *QCD Functional Integrals for Systems with Nonzero Chemical Potential*, arXiv:hep-ph/0405043 (2004).
- [101] S. Carignano, D. Nickel and M. Buballa, *Influence of vector interaction and Polyakov loop dynamics on inhomogeneous chiral symmetry breaking phases*, Phys. Rev. D**82**, 054009 (2010).
- [102] S. Carignano and M. Buballa, *Two-dimensional chiral crystals in the Nambu-Jona-Lasinio model*, Phys. Rev. D**86**, 074018 (2012).
- [103] J. A. Bowers and K. Rajagopal, *Crystallography of color superconductivity*, Phys. Rev. D**66**, 065002 (2002).
- [104] R. Casalbuoni and G. Nardulli, *Inhomogeneous superconductivity in condensed matter and QCD*, Reviews of Modern Physics **76**, 263–320 (2004).
- [105] D. Nickel and M. Buballa, *Solitonic ground states in (color) superconductivity*, Phys. Rev. D**79**, 054009 (2009).
- [106] V. Schön and M. Thies, *Emergence of the Skyrme crystal in Gross-Neveu and 't Hooft models at finite density*, Phys. Rev. D**62**, 096002 (2000).
- [107] Y. Nambu and G. Jona-Lasinio, *Dynamical Model of Elementary Particles Based on an Analogy with Superconductivity. II*, Physical Review **124**, 246–254 (1961).

Danksagung

An dieser Stelle möchte ich nun einer Reihe von Menschen danken, die zum Gelingen dieser Arbeit beigetragen haben.

Mein erster Dank geht an Prof. Jochen Wambach für die Möglichkeit, diese Arbeit in seiner Gruppe schreiben zu können, und die stetige Unterstützung bei allen fachlichen und auch verwaltungstechnischen Angelegenheiten.

Ein besonderer Dank geht an Dr. Michael Buballa für die großartige Betreuung dieser Arbeit und für alle langen und kurzen Diskussionen zu all meinen Fragen und Problemen.

Bei Prof. Christian Fischer möchte ich mich für viele hilfreiche Tipps zu Dyson-Schwinger Gleichungen und auch die Hilfe bei der Einarbeitung bedanken.

Für die Hilfe in der Anfangsphase möchte ich mich auch bei Jens Müller und Dominik Nickel (hauptsächlich indirekt durch seine Thesis) bedanken.

David Scheffler möchte ich danken, dass er bei den meisten Computerproblemen eine Antwort wusste und mich auch bei meinen Admintätigkeiten unterstützt hat (und dafür jetzt diesen Job erbt). Für zahlreiche physikalische, aber oftmals auch nichtphysikalische Diskussionen möchte ich mich auch bei allen meinen Bürokollegen bedanken, insbesondere bei Pascal Büscher (auch für das Korrekturlesen (und auch für das Dartboard)) und bei Stefano Carignano, der trotz (vermutlich vorgetäuschter) Unlust am zuverlässigsten bei allen sich ergebenden Wanderungen dabei war.

Für Diskussionen und Sonstiges möchte ich auch noch Hannes Basler, Sam Edwards, Klaus Heckmann, Sabine Reinhardt, Thorsten Zöller, den restlichen Kickern des schon seit einer Weile leider ausgestorbenen Fußballtrupps sowie allen Beteiligten des „Spiele-Seminars“ danken. Außerdem sollte ich die mittlerweile Gießener Fraktion Jacqueline Bonnet und Jan Lücker nicht vergessen.

Für Reisekostenunterstützung und interessante Seminarwochen bedanke ich mich bei der Helmholtz Graduate School for Hadron and Ion Research.

Zu guter Letzt möchte ich mich auch bei meinen Eltern bedanken, auf deren Unterstützung ich immer zählen konnte.

Lebenslauf

Name: Daniel Roland Müller
Geburtsdatum: 05. April 1985
Geburtsort: Miltenberg
Nationalität: Deutsch
Familienstand: Ledig

Bildungsweg

9/1991 - 8/1995	Grundschule Dorfprozelten
9/1995 - 6/2004	Johannes-Butzbach-Gymnasium Miltenberg Abschluss: Abitur (sehr gut)
7/2004 - 3/2005	Wehrdienst in Külsheim und Veitshöchheim
4/2005 - 11/2007	Bachelor Studium in Physik an der TU Darmstadt Abschluss: Bachelor of Science (sehr gut)
11/2007 - 8/2009	Master Studium in Physik an der TU Darmstadt Abschluss: Master of Science (sehr gut)
seit 10/2009	Promotionsstudium an der TU Darmstadt
seit 10/2009	Wissenschaftlicher Mitarbeiter am Institut für Kernphysik der TU Darmstadt

Erklärung

Hiermit erkläre ich, dass ich die vorliegende Dissertation selbständig verfasst, keine anderen als die angegebenen Hilfsmittel verwendet und noch keinen Promotionsversuch unternommen habe.

Ort, Datum

Unterschrift